HIGHLY-RESOLVED TEMPOROSPATIAL SHRINKAGE KINETICS OF RESIN-BASED COMPOSITES USING LASER INTERFEROMETRY

by

Ivan Kostylev

Submitted in partial fulfilment of the requirements
for the degree of Master of Science

at

Dalhousie University
Halifax, Nova Scotia
July 2014

TABLE OF CONTENTS

LIST OF TABLES

LIST OF FIGURES

ABSTRACT

Photocurable resin-based composites (RBCs) are commonly used as dental restoratives due to their superior aesthetic quality. An enduring problem is that photocuring RBCs results in polymerization shrinkage that may lead to clinical failure of the restoration. A novel Michelson interferometer based approach is developed for accurately measuring shrinkage dynamics and topography of fast heterogeneously curing RBCs in the bonded disc geometry. The main components of the apparatus consist of a Helium-Neon (HeNe) laser and a CCD camera with 122 frames per second acquisition rate capable of measuring shrinkage rates up to 19.3 μm/s with a spatial resolution on the sample of 20.6 μm. The accuracy and reliability of the system were confirmed by comparison with a photodiode, profilometer, and spherical mirrors. Study on sample geometry demonstrated that coverslip rigidity affects the RBC shrinkage kinetics especially for low power inhomogeneous light-curing unit (LCU) irradiance beam profile. The inhomogeneous beam profile of a LED-based polywavelength (1 violet and 2 blue LEDs) LCU was evident in the shrinkage map at short time but obfuscated at long exposure time. Reproducibility of results and uncertainty of deflection rates are attributed to LCU power fluctuation and data acquisition rates, respectively. Autocatalytic equation fits well to experimental results and suggests a greater possible maximum shrinkage for lower LCU irradiance. A linear relationship between the degree of conversion of RBC, measured by a Fourier Transform Infrared Spectrometer, and the shrinkage was observed across the full range of measured values. Nevertheless, a difference in the reaction order parameters derived from the autocatalytic equation fits to the data for DC and shrinkage is observed.

LIST OF ABBREVIATIONS AND SYMBOLS USED

ϕ	Phase Difference
1D	One Dimensional
2D	Two Dimensional
A	Amplitude of Cosine Function
a	Deflection Rate Constant
$A_{aliphatic}$	Aea of the Aliphatic Absorption Peak
$A_{aliphatic,uncured}$	Area of the Aliphatic Absorption Peak of the Uncured RBC
$A_{aromatic}$	Area of the Aromatic Absorption Peak
$A_{aromatic,uncured}$	Area of the Aromatic Absorption Peak of the Uncured RBC
ATR-FTIR	Attenuated Total Reflection Fourier Transform Infrared Spectroscopy
B	Initial Phase of Cosine Function
b	Maximum Deflection
Bis-GMA	Bisphenol A-Glycidyl Methacrylate
C	Intensity offset of Cosine Function
CCD	Charged-Coupled Device
C-factor	Configuration factor
CQ	Camphorquinone
D	Deflection
D_o	Deflection at Peak Deflection Rate
DC	Degree of Conversion
f	Focal Length of Spherical Mirror
FPS	Frames per Second
FWHM	Full-Width Half-Max
HeNe	Helium Neon
I	Interference Intensity
k	Shrinkage Strain Rate Constant
k'	Reaction Rate Constant
L	Optical Path Length Difference
LCU	Light Curing Unit
LED	Light Emitting Diode
LVDT	Linear Variable Differential Transformer
m	Reaction Order
n	Reaction Order
OD	Optical Density
r	Radial Distance
R	Radius of Curvature
RBC	Resin-Based Composite
α	Degree of Conversion
α_m	Maximum Degree of Conversion
δ	Normalized Deflection
δ_o	Normalized Deflection at Peak Normalized Deflection Rate
ε	Shrinkage Strain

ε_m	Maximum Shrinkage Strain
λ	Emission Wavelength of HeNe Laser
π	Ratio of a Circle's Circumference to its Diameter (≈3.14159)

ACKNOWLEDGEMENTS

I wish to express my gratitude to the following people:

My supervisor Dr. Daniel Labrie for guidance and discussions, not only about the research work, but about my career plans and other matters as well.

My co-supervisor Dr. Richard Price for further guidance and a perspective on the work from the Dentistry side.

Tolson Winters for editing chapters 3 to 5 of my thesis.

The support staff from the machine shop Kevin Borgel and John Noddin whose expertise was critical to the construction of the many essential components of the measurement system.

The technologist Mark LeBlanc from the Electrical & Computer Engineering Department for the modification of the Bluephase Style LCU to include a remote activation switch.

Dr. Sergey Ponomarenko, Dr. David C. Watts, and others involved for the stimulating discussions we had on various separate occasions. In addition, Dr. Watts provided the 100 µm thick glass coverslips that were used in this study.

Dr. Harm Rotermund, departmental chair, who provided departmental support. Without his support, this work would not have been possible.

Furthermore, I am grateful to those who were not as directly involved with my research work but whose impact was nevertheless momentous:

My brother Andrey and my friends who further enrich my life and whose company is vital for the (hopefully mutual) relief of stress.

My relatives who support me from Ukraine and especially my late grandfather Eduard who, a scientist himself, always provided encouragement and advice on my life and career choices.

Most of all - my parents Vladimir and Rita (also scientists) for their continued guidance, patience, moral (and financial) support, and love.

Chapter 1
INTRODUCTION

1.1 BACKGROUND

The use of photocured resin-based composites (RBCs) to the field of dentistry has led to tremendous research activities in polymer and materials engineering [1–8]. It is estimated that there are 236 million direct RBC related restorations placed annually in the world [9]. A study done in Sweden showed that the average life of a RBC-based filling is only six years [10]. A similar study performed by the US navy found that the replacement rate for RBC restorations is significantly higher than that for amalgam; the latter has an average life of 15 years [11]. A major challenge with direct RBC restoration is related to the polymerization shrinkage strain of the methacrylate-based resins during curing. For instance, shrinkage strain may lead to significant stress development at the tooth walls. This may result in microcracking, failure of the RBC-tooth interface leading to microleakage, secondary caries, and clinical failure of the restoration [12–14]. RBC shrinkage is significant from the point of view of the size of the bacteria that causes caries, *Streptococcus mutans*, which is about 0.3 μm in size [15]. This indicates that any gap formed from microleakage that is greater than 0.3 μm in size poses risk for further development of caries. The addition of nanoparticle filler in the RBC reduces the degree of shrinkage in the cured RBC, but the shrinkage is still appreciable [16]. Although efforts are made to develop new polymer composites with better physical properties [7,17,18], methacrylate-based composites are, to date, still the materials of choice for this application.

The research related to the photopolymerization of methacrylate-based composites is very rich and involves the study of a complex interplay between the photo-induced reaction kinetics such as polymer chain growth and crosslinking, volumetric shrinkage, and time dependent viscoelastic properties of the RBC [1–4,19–27]. These RBCs have been the subject of extensive studies since their introduction more than fifty years ago [28]. With photoinitiation and resulting kinetics, the monomers which are initially loosely bound by weak van der Waals forces are gradually integrated, although heterogeneously, into networks by strong covalent bonds. The average intermolecular distance is reduced resulting in volume shrinkage of the RBC [25]. In contemporary RBCs photoinitiation occurs by exposure to blue light emitted by a light curing unit (LCU).

1.2 Overview of Shrinkage Measurement Instrumentation

1.2.1 Volumetric Shrinkage Measurement Instrumentation

Several approaches have been used to measure the shrinkage strain in RBCs. One of the first and still widely used methods is the mercury dilatometer [29–31]. When the RBC shrinks upon photocuring the total volume of the RBC and mercury within the reservoir decreases. The small decrease in volume is measured by the drop in mercury level inside the capillary tube. Several disadvantages of this method are that mercury is toxic, the procedure is time consuming, it is sensitive to temperature fluctuations, it can only measure the final shrinkage, and finally mercury is not transparent to light. A water-based dilatometer [32] may also be used to alleviate the safety and handling concern, but the

RBC may absorb water thus affecting the result. A technique based on Archimedes' Principle, the Buoyancy Method, is also commonly used to measure the volumetric shrinkage [30,33–36]. The method involves measuring the weight of the RBC inside and outside of the water using a scale and then knowing the density of water and air to calculate the density of the RBC. The disadvantage of this method is that it is sensitive to temperature, voids, and air bubbles inside or on the RBC. Watts *et al.* [33] used silicone as their Archimedean fluid. Lee *et al.* [34] used an electromagnetic balance with a precision of 10 μg in order to make real time measurements of shrinkage. Dewaele *et al.* [35] used a density column, which is a calibrated graduated cylinder filled with liquids of varying density kept at static equilibrium. A solid sample would floats within the column at a level corresponding to its density. This approach was stated by the authors as being more accurate than the Archimedes' principle for measuring the volume of the cured RBC.

The gas pycnometer is an instrument that uses Boyle's Law (gas pressure increases with decreasing volume) to determine changes in volume of a specimen from the changes in pressure in the device. The system is incapable of making measurements during the curing process of the RBC because it takes 45 min to achieve an accurate results. The measurement accuracy has been reported to be ± 0.002 cm^3 which corresponds to ± 0.2 % for a 1 cm^3 sample [37].

1.2.2 Linear Shrinkage Measurement Instrumentation

In 1991 Watts *et al.* [38] popularized a method first introduced by Wilson [39] called the "Bonded Disc method" or referred to as the "Deflecting Disc Method". The technique has since become widely used to measure the axial linear shrinkage [16,25,31,40–43]. This method typically employs a linear variable differential transformer (LVDT) displacement transducer to measure the sample deflection along the axis normal to the sample disc surface. The LVDT displacement transducer has been reported to have a sensitivity better than 0.1 μm and can output 4 data points per second [38].

In the bonded disc method the RBC is shaped in the form of a disc sandwiched between a thick glass disc and a thin coverslip; the latter is supported by a brass ring. The large sample diameter to thickness ratio (>5) used in this method causes the sample to have close to half of its total surface area bonded to a rigid structure. The bonded surfaces inhibit shrinkage in the radial component resulting in shrinkage only in the axial direction [40]. For an unbound RBC sample, isotropic contraction occurs and the linear shrinkage is approximately $1/3^{rd}$ of the volumetric shrinkage strain for relatively small changes in volume. However, when all except for the axial component is bound and for a large sample diameter to thickness ratio, anisotropic contraction occurs where the axial shrinkage is, in principle, equal to that of the volumetric shrinkage strain [41].

The strain gauge is another early technique that was used to measure linear shrinkage [44]. Using this technique, a sample is adhered to a metallic foil pattern on an insulating

flexible backing. When the sample is deformed so does the foil thus changing its measured electrical resistance. The device is calibrated so that changes in resistance are related to strain. Its major drawback is that strain measurements can be monitored only after gelation since a minimum amount of stress from the sample is required to affect the gauge. The thermal expansion of the gauge caused by the sample exotherm and LCU irradiation both contribute to the measured strain values and consequentially have to be subtracted out from the data. Sakaguchi *et al.* [31] improved on the strain gauge from their previous work [44] by using a biaxial strain gauge where the two orthogonal strain measurements were averaged. Data was collected at a sampling rate of two data points per second with a standard deviation quoted to be 0.004% (at 60 s) and 0.006% (at 300 s) for the shrinkage strain.

In 1993 a new measurement device dubbed the "linometer" was made to measure the isotropic linear shrinkage of an unbound RBC [45]. This technique employs a RBC sample sandwiched between the top fixed glass substrate and bottom movable aluminum disc. As the RBC shrinks it pulls the aluminum disc up towards the glass substrate and a contactless displacement transducer such as an infrared micrometer tracks the disc movement. The results generally agree with those measured using a mercury dilatometer [45,46]. Rosin *et al.* [30] found shrinkage values that were lower than those obtained using the bonded disc method [38]. The linometer technique has also been used to correlate unbound linear shrinkage with degree of conversion, flexural modulus, and shrinkage stress [47]. The relative uncertainty in estimating the final shrinkage strain ranged from 0.2% to 1.1% [47]. Advantages of this method are its ease of use and its

insensitivity to changes in temperature and humidity. A shortcoming of this method is the measurement of the true linear shrinkage requires a thin lubricating layer on the RBC sample so that radial shrinkage is not restricted by the adhesion to the glass and aluminum surfaces. The combined effects of gravity, type of lubricant used, and the RBC viscous properties may affect the results [45].

Another notable method for measuring linear shrinkage is the laser scanning micrometer. The basic principle of operation is that an opaque sample is placed in between the path of a laser beam to a photodiode, the laser beam scans across the sample at a uniform speed, and when the sample obscures the laser beam there is no signal in the detector. Conversely, when the beam is unobstructed there is a signal in the detector. Knowing the laser beam's transverse speed and the time interval between the beam being obstructed (no signal) and unobstructed (signal) by the sample is then used to calculate its thickness. This method is similar to a caliper with an accuracy of 1 μm [48].

1.2.3 Imaging Techniques

Aside from the common mechanical measurement methods, there are imaging techniques to monitor the RBC shrinkage strain. The first method [49,50] was to make a spherical ball of the RBC and then determine the volumetric shrinkage from the decrease of the projected area. Spherical sample geometry is required to ensure accuracy of the conversion from projected area to volume. Another method [42] includes placing two markers, one at each end of a long cylindrically shaped RBC, and measure their positions before and after irradiation to calculate the linear shrinkage. Lee *et al.* [51] placed a

marker further away from the RBC sample connected by a cover glass in order to avoid the camera being saturated by the LCU light during light exposure. Another technique is the Digital Image Correlation which became a widely used approach in determining axial and transverse shrinkage in RBC samples. It requires the use of tracer particles and a video camera to track the particles with time. One of the common issues with this technique is that in most cases the CCD sensor was saturated when the LCU was on [52–56] resulting in no shrinkage data during light exposure. Another limitation of this technique is that motion of particles out of plane distorts the measured in-plane strain values. In the Li *et al.* study [52], the false in-plane shrinkage strain was 0.015% for a 0.5% axial shrinkage strain which corresponded to a relative error of 3%. Miletic *et al.* [54], Milosevic *et al.* [56] and Martinsen *et al.* [57] used 2 cameras to get out-of-plane movement vectors to improve the measurement accuracy. Martinsen *et al.* quote an average absolute error in the strain measurement of their system to be 0.01% [57]. To improve the technique Kweon *et al.* [58] employed the use of fluorescent particles and an optical filter to allow video acquisition at 2 frames per second while the LCU is on. Their system had a spatial resolution of 4.54 μm per pixel, but with sub-pixel accuracy due to the "area center method" used to determine the particle coordinates (the more pixels comprising the area of the particle the higher the accuracy).

A laser-speckle correlation method has been used [32] to study shrinkage rates. The system measures the changes in the speckle pattern as the RBC undergoes polymerization shrinkage. A video camera is used to capture the speckle patterns at 10 frames per second and each successive pair of images in the video are used to calculate the Pearson's

product-moment correlation coefficient. Low or high correlation coefficient value indicates the highest or lowest rate of polymerization, respectively. A drawback of this approach is that one does not measure the true shrinkage, but rather a correlation value. Also the analysis method used does not consider spatial variation of the shrinkage although the spatial resolution of the images is 5 μm. Wells-Gray *et al.* [59] used the theory of dynamic light scattering to probe the reaction kinetics of the sample by including the molecular motion within the bulk of the RBC. In this method, the correlation rate is proportional to the degree of motion within the bulk of the sample rather than just on the surface. Their system was capable of a sampling rate of 32 frames per second. This allowed them to measure the correlation rate peak in higher detail than previous works using laser-speckle correlation methodology.

X-ray micro-computed tomography has been used to image strain vectors inside the RBC [60–62]. Radio-opaque tracer particles are mixed into the RBC and then imaged before and after light exposure to determine the strain field. Due to the nature of the device, the measurements take hours to do and hence can be done only before and after curing of the RBC. The spatial resolution in the latest study was 14.2 μm [62].

1.2.4 Laser Interferometry

Optical Coherence Tomography was used to calculate the linear shrinkage of material by measuring the change in sample thickness [36]. The instrument consists of a low coherence Michelson interferometer using a broadband source (e.g. Ti:sapphire laser). As light penetrates into the sample, only the light that travels the same optical path length

along the two arms of the interferometer interferes constructively and results in a large intensity signal at the detector. By varying the optical path length along the reference arm one "scans" through the sample thickness. The maximum image depth achieved in their work is 1.6 mm and an axial resolution of 6.2 μm is obtained. This method has the advantage of being able to calculate the average refractive index of the material by dividing the optical path length by the sample thickness [36].

A series of interferometric techniques using a quasi-monochromatic source were used for measuring polymerization shrinkage. The first application of such a technique used thin film samples where the sample-substrate interface functions as the reference surface for the interferometer [22,63]. The laser beam is partially reflected at the sample-air surface and substrate-sample interface and then the two reflected beams interfere on the photodetector. The interference patterns give information on the sample thickness and how it varies over time. The drawback with this method is that it only works for thin non-opaque thin film (≤30 μm) RBCs, it requires knowing the refractive index of the RBC as it cures, and it provides information only at the center of the sample since a single photodetector was used. Note that the laser beam diameter is not optically altered in Ref. [22,63] and hence likely to be close to 0.8 mm of a contemporary 5 mW HeNe laser. Fogleman *et al.* [64] used a setup with a fixed reference mirror and a "movable" mirror affixed to the RBC sample so that the sample shrinkage could be measured from the mirror displacement. Again, this method does not give information about the varying degrees of shrinkage across the sample surface. The principle of the fiber optic Fizeau interferometer [65] is similar to that of a Michelson interferometer where the moving mirror is replaced by an aluminum foil placed on top of the sample and the fixed mirror

corresponds to the glass/air interface at the fiber optics tip. These aforementioned "1D" methods all have good time resolution only limited by the data acquisition hardware. By using an imaging camera instead of a photodiode, spatially varying shrinkage information can be extracted from the interference patterns. Only one group so far utilized this approach [66–68]. Their experimental setup was such that a reflecting mirror was placed on top of the sample and it pivoted as the sample shrunk. The laser beam that was reflected from the mirror was recombined with the beam from the reference mirror to produce an interference pattern on the camera. The highest achieved camera acquisition rate was 50 frames per second (500x582 pixel resolution) [68]. As they cured their samples the interference pattern shifted from its original position and then the pattern was shifted back by a micrometer thus mechanically determining the total shrinkage. For real time measurement they employed interference fringe counting. Due to their experimental design, there was no information provided on the variations of shrinkage across the sample surface. An alternative method used was off-axis holography [69]. In this approach the axial shrinkage is not measured, but the radial deflection of a tooth is determined instead. Similar to Michelson interferometry the shrinkage values are determined by interference fringe counting. The holographic method required that their tooth had to be coated with silver paint to prevent multiple light backscattering.

1.3 RBC PROPERTIES

1.3.1 Shrinkage Kinetics Modeling by Autocatalytic Equation

Recently, it was shown [16,22,23] that the shrinkage strain of dimethacrylate RBCs follows the autocatalytic model of Kamal [70] reflecting the diffusion-controlled kinetics of the polymerization of dimethacrylate monomers. It is interesting to note that in Ref. [16], the data presented in Fig. 2 of the time dependent shrinkage strain rate collected at three temperatures appear qualitatively well described by the autocatalytic model. It has been observed that in certain cases the RBC initially expands when the LCU is turned on. The light induced expansion is attributed to thermal expansion [68,71,72]. Due to the functional form of the autocatalytic model, it does not model negative strain (expansion) or strain rate, which means such data has to be excluded when fitting using this equation. The experimental technique used was the bonded-disc technique, which measures the axial shrinkage at the center of a disc shaped sample. Their sample dimensions were 1.5 mm thick by 8 mm diameter, which was sandwiched between a 3 mm thick glass plate and a 100 μm thin flexible glass cover slip [73].

1.3.2 LCU Beam Profile Effects on RBC Cure

The LCU beam profile normal to its optical axis is a 2D map of the light irradiance distribution across the beam and it varies with distance away from the LCU tip end. Studies have shown that the surfaces of cured RBC samples exhibit non-uniform hardness depending on the LCU positioning and their beam profiles [74,75]. It is known that the degree of conversion (DC), micro hardness, and shrinkage strain all correlate

together for the methacrylate-based composites and that they are affected by the avereged light irradiance [47,76–78]. As a result, non-uniform shrinkage strain across the sample surface is expected. An initial study performed by Watts *et al.* [73] showed that the cured RBC samples (bonded disc geometry; 1.5 mm thick and 8 mm diameter samples) took on a flat surface profile. This was determined using a profilometer that scanned across the diameter of the sample.

1.4 THESIS OBJECTIVES

In this work, a novel approach is introduced to measure the full axial shrinkage field across the sample surface in real time before, during, and after light exposure with a spatial and temporal resolution of 20 μm and 8 ms, respectively. In this approach, a Michelson interferometer, Helium-Neon (HeNe) laser, and charged-coupled device (CCD) camera with 122 frames per second acquisition rate are used to image the axial shrinkage field. The sample geometry utilised in this work is a modification of that used in the bonded disc method. By using laser interferometry this approach has an internal absolute displacement calibration. The CCD camera high frame rate allows monitoring of fast axial shrinkage dynamics with shrinkage rates up to 19.3 μm/s. All previous methods had either a high spatial or temporal resolution, but did not possess both types of resolution. For example X-ray micro-computed tomography has excellent spatial resolution, but takes hours to acquire the data and the Fizeau interferometer has high data acquisition rate, but provides no spatial information. In light of the aforementioned, this work's approach opens up a new avenue toward studying the shrinkage dynamics of fast heterogeneously curing RBCs.

1.5 THESIS OUTLINE

The next chapter describes the experimental procedure used to measure the axial shrinkage field and the approach utilized to reconstruct the axial shrinkage field map as a function of time from the imaged interference patterns. Chapter 3 presents results on the role of the sample geometry and beam profile on the axial shrinkage map during and after photopolymerization and elucidates the role of the cover slip and the brass ring. Chapter 4 presents the results on the dependence of the irradiance level and beam profile on the axial shrinkage. Chapter 5 presents the RBC shrinkage kinetics and degree of conversion fitted by the autocatalyic model. Chapter 6 summarizes the findings in this study and future work.

Chapter 2
EXPERIMENTAL TECHNIQUES AND METHODOLOGY

In this chapter, the principle of a Michelson interferometer and its application to the measurement of the axial 2D shrinkage of dental RBCs in real time is first presented. Section 2 details the experimental apparatus and procedure. In section 3, the results of the spatial and temporal calibration of the apparatus are given. The final section summarizes the findings of this chapter.

2.1 APPROACH USED TO MEASURE THE AXIAL SHRINKAGE FIELD ACROSS THE SAMPLE SURFACE

A Michelson interferometer is a non-contact method of measuring minute differences between the optical path lengths using a photodetector of the interferometer arms. Figure 1 demonstrates the basic principle of a Michelson interferometer. A collimated laser beam from a Helium-Neon (HeNe) laser passes through a beam splitter and is split into two beams that then travel along the two arms of the interferometer. At the end of each arm of the interferometer is a reflecting surface, such as a plane mirror, which reflects the light beams back. The two beams recombine at the beam splitter and then cause interference patterns at the detector. The light intensity at the detector varies between a maximum and minimum value caused by the constructive and destructive interference between the two light beams. Constructive and destructive interference occur when the difference in optical path length between the two light beams is equal to $n\lambda$ and $(n+1/2)\lambda$, respectively, where n is an integer and λ is the laser wavelength.

Figure 2 illustrates the effect of two optical geometries on a Michelson interferometer. If a plane mirror is placed on the sample arm of the interferometer, titled at an angle with respect to the optical axis, a vertical band-like interference pattern forms on the imaging screen. If the tilted plane mirror is replaced by a spherical mirror - a circular band-like interference pattern forms on the screen. The symmetry of the mirror surface, relative to the optical axis, manifests itself in the interference pattern. A non-uniform mirror surface normal to the optical axis imparts a non-uniform phase shift across the laser beam and thus is observed as a non-uniform interference pattern on the screen. In the interference pattern, the distance from one bright (or dark fringe) to its adjacent one, corresponds to an axial displacement of $\lambda/2$ on the mirror surface. As a result, for a laser emission wavelength of 632.8 nm, the interference pattern undergoes a full oscillation for a 316.4 nm deflection of the mirror surface.

2.2 Experimental Apparatus and Procedure

2.2.1 Optical Configuration of the Apparatus

The schematic diagram of the experimental apparatus used to measure the real-time shrinkage of light-cured RBCs is shown in Figure 3. A 632.8 nm emission wavelength 1 mW output power HeNe laser is used. The laser beam is collimated by lenses 1 (6 mm focal length) and 2 (750 mm focal length) and directed into a Michelson interferometer. The modulated output beam from the interferometer is focused by lens 3 (125 mm focal length) and partially reflected by a beam splitter into lens 4 (10 mm focal length) and

filter 1 onto the Si photodiode. The modulated output beam transmitted through the beam splitter is directed through filter 2, camera objective (30 mm focal length; f/1.4), and filter 3 onto the CCD camera. Aperture 1 is used to cut stray laser light while aperture 2 is used to restrict the laser beam to a 10 mm diameter. Aperture 3 is used to block any stray light and light from the LCU. The Si photodiode monitors the modulated laser intensity. The camera images the full field interference pattern over an area that is 10 mm in diameter across the sample. Filters 1 and 3 are 1.0 nm wide band-pass filters centered at 632.8 nm to filter out any stray light. Filter 2 is a red longpass (600 nm cut-off) glass optical filter.

A schematic diagram of the Michelson interferometer part of the experimental apparatus is shown in Figure 4. The incident laser beam is partially reflected at the beam splitter and directed through the neutral density filter (OD = 0.6) onto the reference mirror ($\lambda/10$ surface accuracy). The partially transmitted laser beam through the beam splitter is reflected on the top surface of the sample. The two reflected beams are recombined at the beam splitter and are directed towards lens 3. The neutral density filter is used so that the intensity of reflected light from the sample surface and reference mirror of the interferometer are approximately equal when the two beams recombine at the beam splitter.

Figure 5 shows a photograph of the experimental apparatus on an optical bench. The equipment is encased in an enclosure that prevents dust and ambient light from entering the apparatus (in the photograph the enclosure top is removed). Figure 6 shows a close-up

photograph of the Michelson interferometer. The LCU was positioned so that it illuminated the RBC sample through its quartz disc substrate and its light guide tip was less than 0.5 mm away from the bottom surface of the quartz disc. A Plasma Arc LCU (Sapphire®) set on bleach mode is used for most of the experiments. Either a standard (6 mm entrance and 10 mm diameter exit port) or turbo (6 mm entrance and 3 mm diameter exit port) light guide was used with the LCU. For some experiments, a 250 μm inner diameter aperture was placed on the standard light guide tip to produce a 1 mm diameter beam profile at the sample surface.

Total light power output as a function of time of the Sapphire® LCU using a standard light guide is shown in Figure 7. There is an initial surge in power over the first 10 ms reaching peak value of 893 mW then dropping down to 704 mW, for the next 2.5 seconds the power rises up to 1026 mW, then taking another 2.5 s to drop down to 858 mW, and thereafter gradually increases to 893 mW. The mean output powers (± standard deviation) over 0 to 5 s and 5 to 30 s intervals for five measurement repeats are 824 mW ± 7 mW and 876 mW ± 5 mW, respectively. The radiant exposure up to 5 s and 30 s is 4.12 J and 26.1 J, respectively.

Lens 3 and the camera objective form an afocal system where a collimated light beam entering the system emerges collimated. The afocal system acts as a beam expander in reverse; the modulated 10 mm diameter laser beam entering the system exits with a 3.8 mm diameter beam that is imaged onto the camera's sensor. Using the magnification

factor of 1/3.68 for the afocal system, each camera pixel images a 20.6 μm x 20.6 μm area on the sample surface.

The optical alignment of the afocal system and the camera was achieved in two steps. The first step was to align lens 3 and camera objective such that their separation is the sum of their focal lengths. In this arrangement a collimated light ray incident on the first lens will still be collimated when it exits from the second lens. The second step was to align the camera with respect to its objective by adjusting their separation such that the collimated beam from the reference arm and divergent laser beam from the sample arm overlapped exactly on the camera's sensor. This was done by observing the sample beam changing size in the camera image until it matched the size of the reference arm beam. The divergent laser beam was produced by a concave spherical mirror located in the sample arm. A camera objective was used instead of a short focal length plano-convex lens to minimize any optical distortion produced by the afocal system.

2.2.2 Sample Geometry

A modified bonded disc method was used to measure the surface topography of a RBC. Figure 8 shows the schematic diagram of the bonded disc sample geometry. A disc shaped RBC sample of 1.22 mm thickness and 10 mm diameter is placed on a 1.5 mm or 3 mm thick quartz plate of 25.4 mm diameter. The quartz substrate was sanded using 1200 grit sand paper and then salinized to increase its bonding with the RBC sample. A brass ring of 20 mm inner and 24 mm outer diameter was used to define the sample thickness. The brass ring's thickness was 1.22 mm thick except in some experiments

where it was 1.00 mm thick in which case it is explicitly mentioned in the results of those experiments. In some experiments, the brass ring was removed after making the sample and in others it was used to support a glass coverslip. A thin Borosilicate glass coverslip of 22 mm diameter rested on top of the RBC sample and acted as a reflecting surface for the laser beam. The glass coverslip thickness was either 100 μm or 150 μm so that it could bend and follow the shape of the RBC sample surface as it deformed. In other experiments, a 25 μm thick circular Mylar disc was used instead of the glass coverslip to provide an even higher degree of coverslip flexibility. A brass ring was not used with the Mylar coveslip because the coverslip is sufficiently flexible that the brass ring had no impact on the determination of the surface shape of the RBC sample. Neither glass nor Mylar coverslips were salinized.

A mercury based thermometer was used to monitor the temperature inside the equipment enclosure. During the course of the experiments over a one year period, the sample temperature varied from 20.7 °C to 23.9°C with a corresponding mean temperature of 22.3 °C. The latter temperature will be quoted for all the results. It is assumed that the temperature within the enclosure and the RBC are the same before LCU light exposure.

2.2.3 Data Acquisition of the Interference Patterns

The CCD camera used to capture the interference patterns is a Basler scA640-120gm. Its acquisition rate is 122 frames per second (FPS), 12-bit ADC bit-depth (but 8-bit was used for video acquisition), (659 x 494) pixel² and (4.46 x 3.80) mm² sensor size, and a pixel area of (5.6 x 5.6) μm². The camera was connected to the computer via a National

Instruments GigE Vision Adapter interface card (NI PCIe-8231). The maximum axial shrinkage rate that the system can measure without aliasing is calculated as follows – given the highest 122 FPS sampling rate of the camera and that there is a $\lambda/2$ (316.4 nm) displacement of the sample when the signal, at any given pixel, oscillates a full period then the maximum shrinkage rate that the camera can capture is 19.3 μm/s. Video acquisition was done using a custom made program in LabVIEW. A Si photodiode connected to an amplifier and NI myDAQ with an acquisition rate of 1000 samples/s was used in conjunction with the CCD camera to verify that no aliasing effects due to under-sampling by the camera occurred. The Si photodiode active area diameter was 1 mm in size and was positioned such that the central area diameter of (0.30 ± 0.03) mm part of the sample was observed. This was determined using a flat mirror in the sample holder. With the 8" focal length spherical mirror in the sample holder, the central area diameter of the sample that was observed increased to (0.38 ± 0.04) mm due to an increased beam diameter at the detector.

2.3 Validation of the Spatial and Temporal Dependence of the Interferometric Patterns

2.3.1 Measurements of the Focal Length of Spherical Mirrors Using Interferometry

Three experiments were performed to test the system's spatial accuracy. In one such experiment three concave spherical mirrors with focal lengths of 8", 12", and 18" were used as standards and the interferometer would attempt to independently confirm their focal lengths. The uncertainty in focal length from the manufacturer's specifications is

±2%. The spherical mirrors were purchased from Edmund optics and their specifications are given in Table 1. The 8" focal length has a radius of curvature that would be similar to that of a RBC sample with a high degree of axial shrinkage. Figure 9 shows the recorded interference patterns of the spherical mirrors using the Michelson interferometer. These patterns are then post-processed to maximize the fringe contrast. This is done by acquiring an image of the interference pattern with the spherical mirror placed in the sample holder, and of the sample and reference beam separately by blocking the other beam in its respective arm and taking an image. This allows variations in the laser beam profile to be numerically removed using the equation for interference between two light waves (Equation 9.4 in ref. 79) and extracting the interference term. Figures 10-12 shows the results using a 2D least-squares fit (Levenberg–Marquardt algorithm) of the expected interference pattern from a spherical mirror of known focal length to the post-processed interference patterns for each spherical mirror. The equation used to fit the data is:

$$I(r) = A\cos\left(\frac{\pi r^2}{\lambda f} + B\right) + C \qquad (1)$$

where A is amplitude, B is the initial phase, C is the intensity offset, f is the focal length of the spherical mirror, λ is the wavelength of the laser, and r is the radial distance away from the axis of symmetry of the spherical mirror. A derivation of equation (1) is given in appendix A. The focal length is obtained from the equation (1) and the goodness of fit is confirmed by comparing the overlap between the fit and interferometric data displayed in Figures 10-12. As shown in Table 1 an excellent agreement is obtained between manufacturer's and fitted focal lengths.

2.3.2 Temporal Calibration of the CCD Camera Detection System Using a Parallel Si Photodiode Detection System

To ensure the time resolution of the camera detection system is adequate to digitize the interference patterns without aliasing, a comparison was carried out between the data obtained by the camera and photodiode detection systems. Figure 13 shows the data collected as a function of time of a representative RBC sample during polymerization using both the photodiode and by tracking the output of the central single pixel of the camera's CCD. The sample was prepared using the RBC product Filtek™ Supreme Ultra CT produced by 3M ESPE. The sample was photo-cured for 30 seconds using a Plasma Arc LCU (Sapphire®) on bleach mode (1.38 W/cm²) with a standard light guide. Note that the signal oscillations in the photodiode data overlap with those obtained using the camera data. The observed variation in fringe contrast with time is tentatively attributed to the intensity variation of an unwanted laser light reflection originating from the glass-RBC interface due to the index of refraction of the RBC changing as it cures. The results indicate that the camera frame rate is sufficient to monitor the time dependence of the interference patterns. Figure 14 depicts the axial deflection and deflection rate as a function of time derived from interferometric photodiode and camera (at the center pixel) data.

A peak finding algorithm written in MATLAB located all oscillation extrema in the acquired interference pattern and determined the sample deflection as a function of time. An excellent agreement is obtained between the camera and photodiode data. The appreciable uncertainty in the deflection rate for the camera pixel data versus that of the

photodiode data is evident. Sources of error in the peak finding algorithm from the interference pattern are shown in Figure 15. The uncertainty in the estimation of peak position is greater for the camera than the photodiode data due to fewer data points constituting a period of oscillation. The actual peak position may be in-between two data points thus making peak position uncertainty of about ±4 ms for a sampling rate of 122 FPS. Photodiode data is acquired at about 10 times the rate of the camera, thus only making the peak position uncertainty of ±0.5 ms. The presence of noise may also shift the peak position near the extrema. Deflection rate uncertainty is solely determined by peak position uncertainty as the deflection is necessarily $\lambda/4$ for a $\pi/2$ phase shift in the interference pattern. In addition, due to noise, low light intensity, or variation in fringe contrast in the acquired interference pattern the peak finding algorithm may falsely detect peaks (false positives) or may miss actual peaks (false negatives) resulting in a systematic error.

2.3.3 Comparison between the Sample Surface Topography of Light-Cured RBC Derived from Interferometry and Profilometry

Figure 16 shows a comparison of interference patterns obtained from the real-time CCD camera video and the shrinkage map calculated for three specific times. The photo-cured RBC sample is made out of Filtek Supreme Ultra CT. The sample was illuminated by a Plasma Arc LCU (Sapphire®) on bleach mode at 876 mW output power (1.37 W/cm²) with a turbo light guide for an exposure time of 30 s. The sample thickness and temperature were 1.22 mm and 22 °C, respectively. The times chosen for the comparison are at 0 s when the LCU was turned on, at 1.764 s when the RBC sample underwent the highest rate of shrinkage, and 1858 s at the end of the video acquisition. The shrinkage

map, that is the deflection as a function position on the sample surface, is not a reconstruction from the spatial distribution of fringes seen in the interference pattern at the time shown, but rather from the time varying intensity at a given camera pixel as the sample cured. It is interesting to note that there is a correlation between the symmetry observed in the shrinkage map and in the interference pattern. The interference pattern shows the topography, but the shrinkage map is the total deflection at the time of observation. If the initial topography is very flat (as shown in Figure 16 (a) with a surface roughness less than 1 μm) the topography at any given time is approximately equal to the shrinkage map which is why symmetry is clearly observed. To confirm the derived topography, the sample surface topography was then measured using a stylus profilometer (Bruker Dektak® surface profiler) and the results were compared.

Figure 17 shows the results obtained using the two measurement systems. The total deflection and variations in topography measured using the profilometer follows very closely those acquired using the interferometer. There is less than 1 μm discrepancy out of a total deflection of 27.5 μm (3.6% difference) in deflection in the line profiles of the 2D maps. The profilometer measures the final sample topography relative to its sample holder stage, while the analysis of the interferometric data presented in this thesis provides the change in sample topography from its initial topography. The profilometer data required tilt correction because the sample surface was not coplanar with the profilometer stage. Tilt correction was done by fitting a plane surface in the acquired data containing the top inner edge of the brass ring and then subtracting out the former from the latter. As a result, a mean deflection value of zero is produced along the top inner

edge of the brass ring (20 mm). Since the glass coverslip rests on the top inner edge of the brass ring, no deflection occurs along that edge.

The sources of discrepancy between the two methods are - the sample may have undergone additional post-curing from the time the sample was measured using the interferometer and then measured using the profilometer (about 1 hour after the measurement using the interferometer and then a total of 4 hour measurement time in the profilometer), the sample orientation is not exactly the same (± 5°), the sample center position is offset (upper limit of 0.265 mm), and the tilt correction is not accurate due to offset in sample and brass ring center position. The brass ring center offset can be as large as 0.125 mm with respect to the quartz disc. This results in an upper limit of 0.390 mm potential offset from the center in the profilometer. In Figure 17 (c), the offset of the brass ring is enough to potentially have the plane surface fit the data encompassing near the local minimum (at about 3.5 mm) and the sharp rise near the edge (at about 4.5 mm). This would correspond to a discrepancy of about 1 μm from edge to the center.

2.4 Degree of Conversion

The DC of dimethacrylate based RBCs can be measured by using Attenuated Total Reflectance Fourier Transform Infrared Spectroscopy (ATR-FTIR) [80]. ATR-FTIR measures the infrared absorption spectrum of a sample. Information about DC is gained by measuring before and during (or after) photopolymerization at the spectral range that includes the absorption peaks of the aromatic (at 1608 cm^{-1}) and aliphatic (1637 cm^{-1}) carbon double bonds in the RBC monomer. The aliphatic absorption peak decreases in

intensity with increasing polymerization whereas the aromatic absorption peak remains constant and is used to normalize the spectrum [81]. After measuring the area of the aliphatic and aromatic absorption peaks the DC is calculated by:

$$DC = 100\% \times \left(1 - \frac{A_{aliphatic}/A_{aromatic}}{A_{aliphatic,uncured}/A_{aromatic,uncured}}\right) \qquad (2)$$

where $A_{aliphatic}$ is the area of the aliphatic absorption peak, $A_{aromatic}$ is the area of the aromatic absorption peak, $A_{aliphatic,uncured}$ is the area of the aliphatic absorption peak of the uncured RBC, and $A_{aromatic,uncured}$ is the area of the aromatic absorption peak of the uncured RBC.

2.5 SUMMARY

In this chapter, the principle of a Michelson interferometer and its application to the measurement of the axial shrinkage topography in real time of RBC sample was presented. The main components of the apparatus consist of a Michelson interferometer and camera detection system capable of collecting up to 122 frames per second. The apparatus temporal resolution of 8 ms was verified using a parallel Si photodiode-amplifier detection system. The sample surface topography measured using laser interferometry was compared against a direct measurement of the sample surface topography of a typical light cured RBC sample using profilometry. Excellent agreement in axial shrinkage was found between the two techniques validating the new approach to measure the axial shrinkage field of photocured RBC samples presented in this thesis.

2.6 Figures and Tables

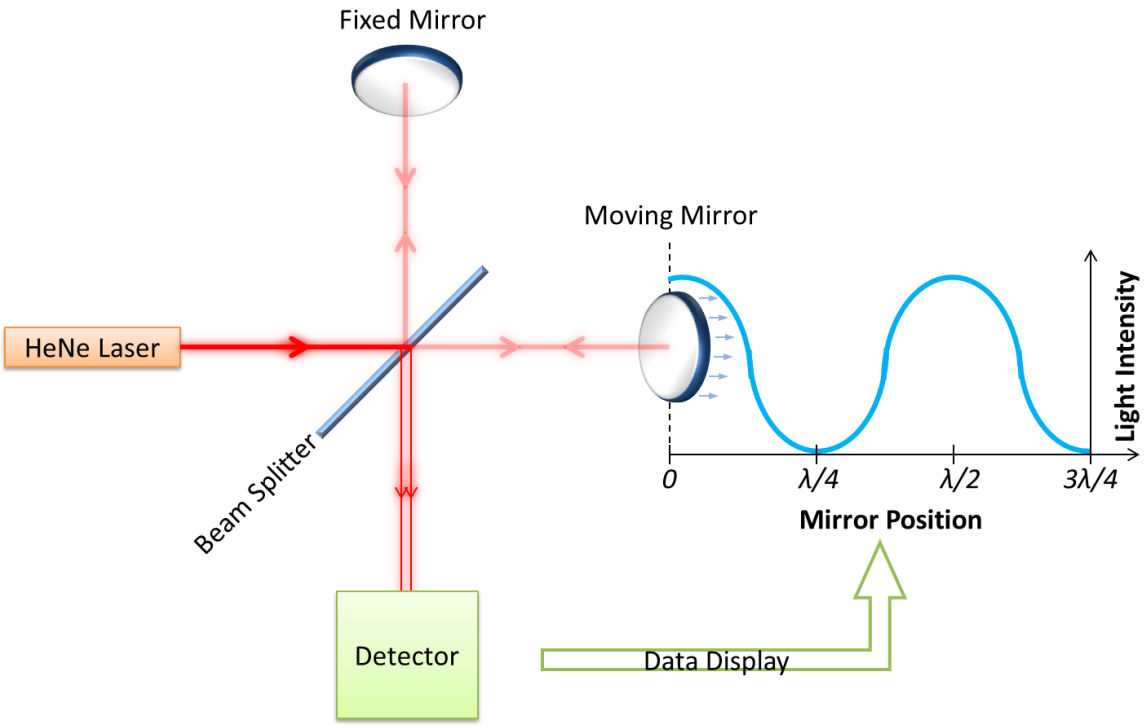

Figure 1 Schematic diagram of a Michelson interferometer with plane mirrors. A collimated laser beam from a HeNe laser is separated at the beam splitter into two beams travelling along the two interferometer arms. The two beams recombine at the beam splitter and then interfere at the detector. The light intensity at the detector varies between a maximum and minimum value caused by the constructive and destructive interference between the two light beams. Constructive and destructive interference occur when the difference in optical path length between the two light beams at the detector is equal to $n\lambda$ and $(n+1/2)\lambda$ where n is an integer, respectively. Note that when the moving mirror travels a distance d, the optical path length of the laser beam is 2d because the light beam has to travel back and forth that distance.

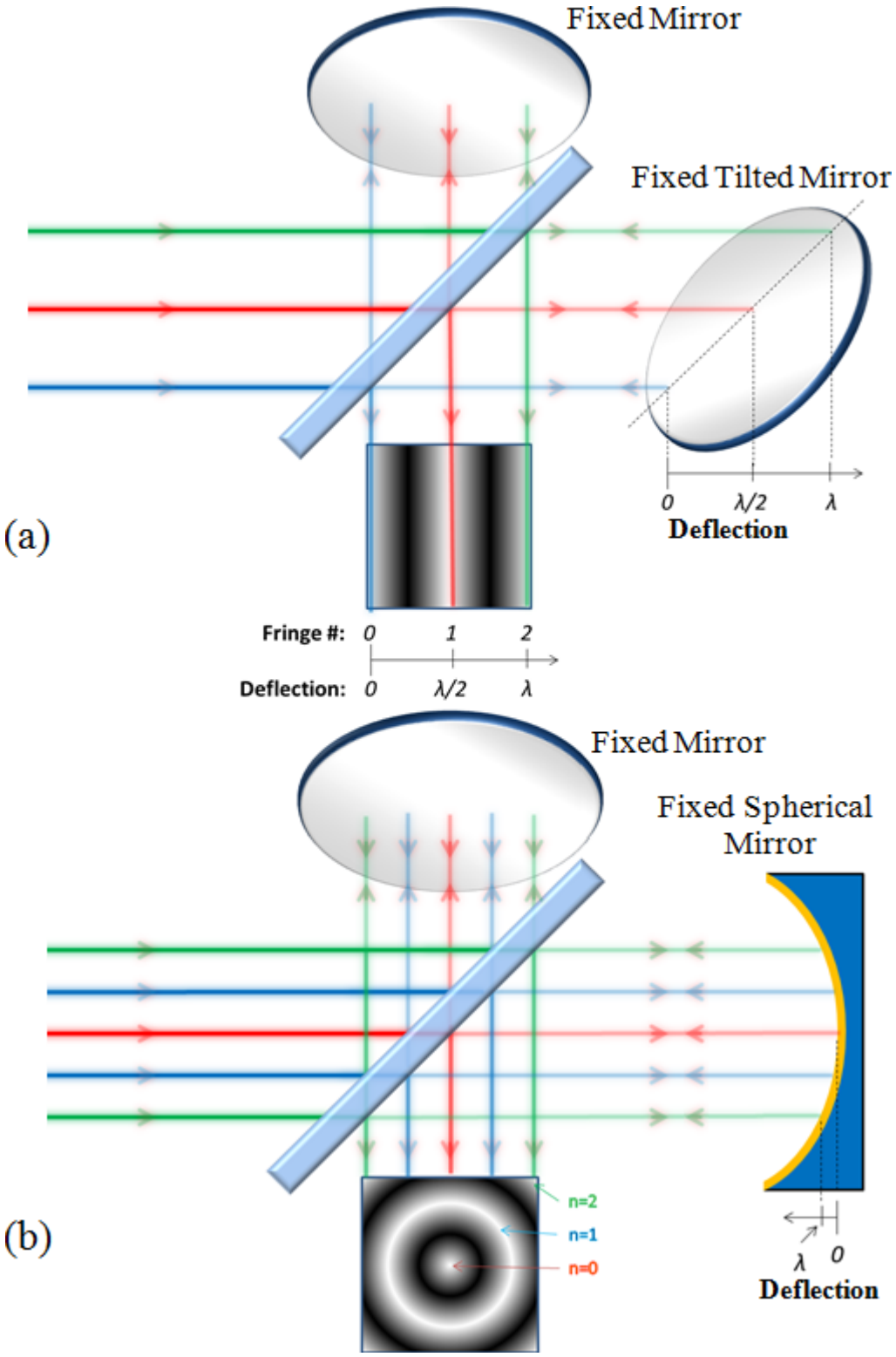

Figure 2 Schematic diagram of a Michelson interferometer for two optical geometries. The colored rays are representative rays of a laser beam with a finite spatial extent. (a)

The fixed tilted mirror is set at an angle with respect to the parallel rays so that the red and green ray travels exactly an additional distance to reach the mirror of $\lambda/2$ and λ relative to the blue ray, respectively. In this case when the laser beam recombines at the imaging screen it forms an interference pattern consisting of vertical bright and dark fringes. By counting the fringe number, one can calculate the deflection of the tilted mirror at each of the red and green light ray relative to the blue ray. (b) The tilted mirror has been replaced by a spherical mirror where its optical axis is along that of the interferometer. Due to the mirror symmetry, a series of circular bright and dark fringes are observed at the imaging screen. As in (a) the change in distance between the outer green ray and the central red ray is λ; hence two bright fringes are observed relative to the central fringe.

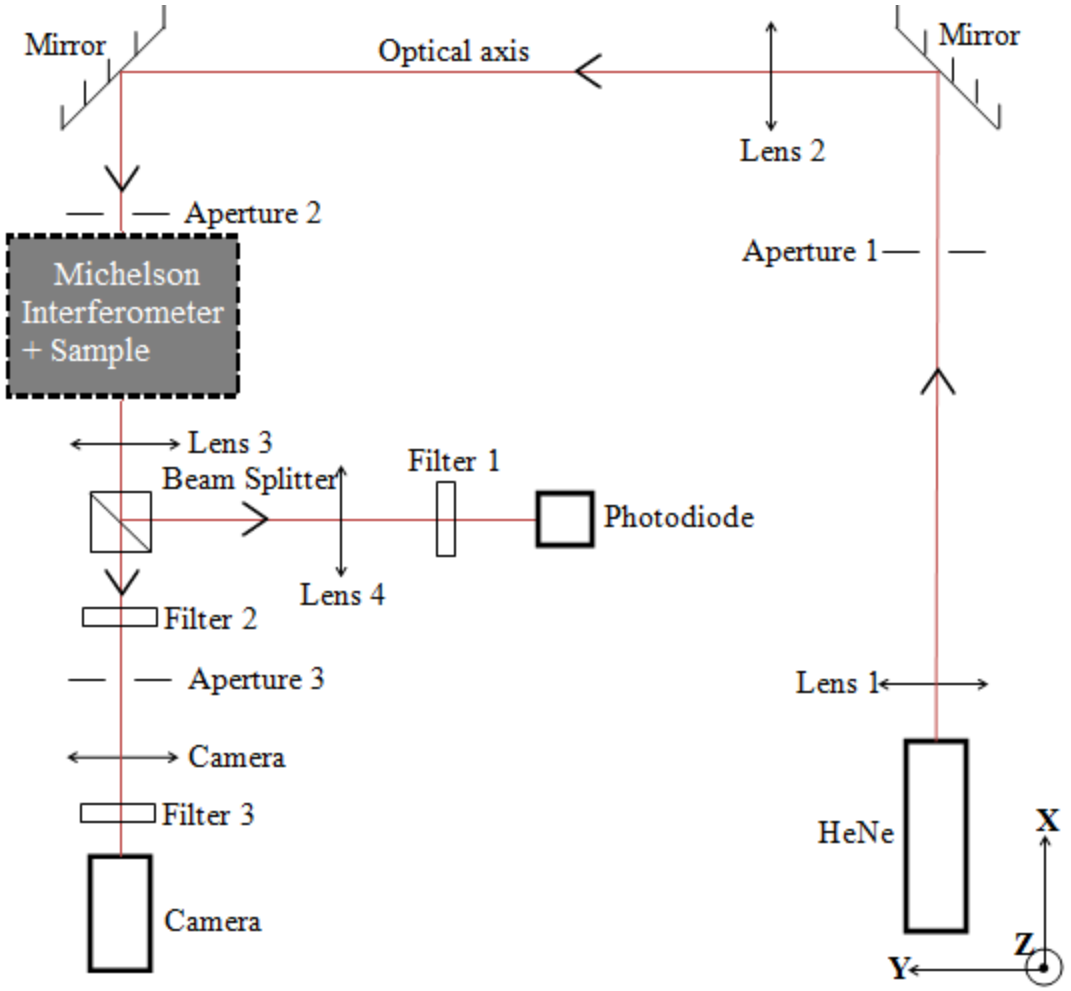

Figure 3 Schematic diagram of the experimental apparatus used to measure the real-time axial shrinkage map of light-cured RBC. The laser beam is collimated by lenses 1 (6 mm focal length) and 2 (750 mm focal length) and directed into a Michelson interferometer where the sample is located. The modulated output beam is focused by lens 3 (125 mm focal length) and partially reflected by a beam splitter into lens 4 (10 mm focal length) and filter 1 onto the Si photodiode. The transmitted modulated beam is directed through filter 2, camera objective (30 mm focal length; f/1.4), and filter 3 onto the CCD camera. Aperture 1 is used to cut stray laser light while aperture 2 is used to define the laser beam to 10 mm diameter. Filter 2 greatly attenuates any blue light emitted by the LCU. Aperture 3 is used to block any stray light and light from the LCU. The Si photodiode monitors the modulated laser intensity at the center of the sample. The camera images the full field interference pattern from across the 10 mm diameter sample. Filters 1 and 3 are 1.0 nm wide band-pass filters centered at 632.8 nm to filter out any stray light. Filter 2 is a red longpass (600 nm cut-off) glass optical filter.

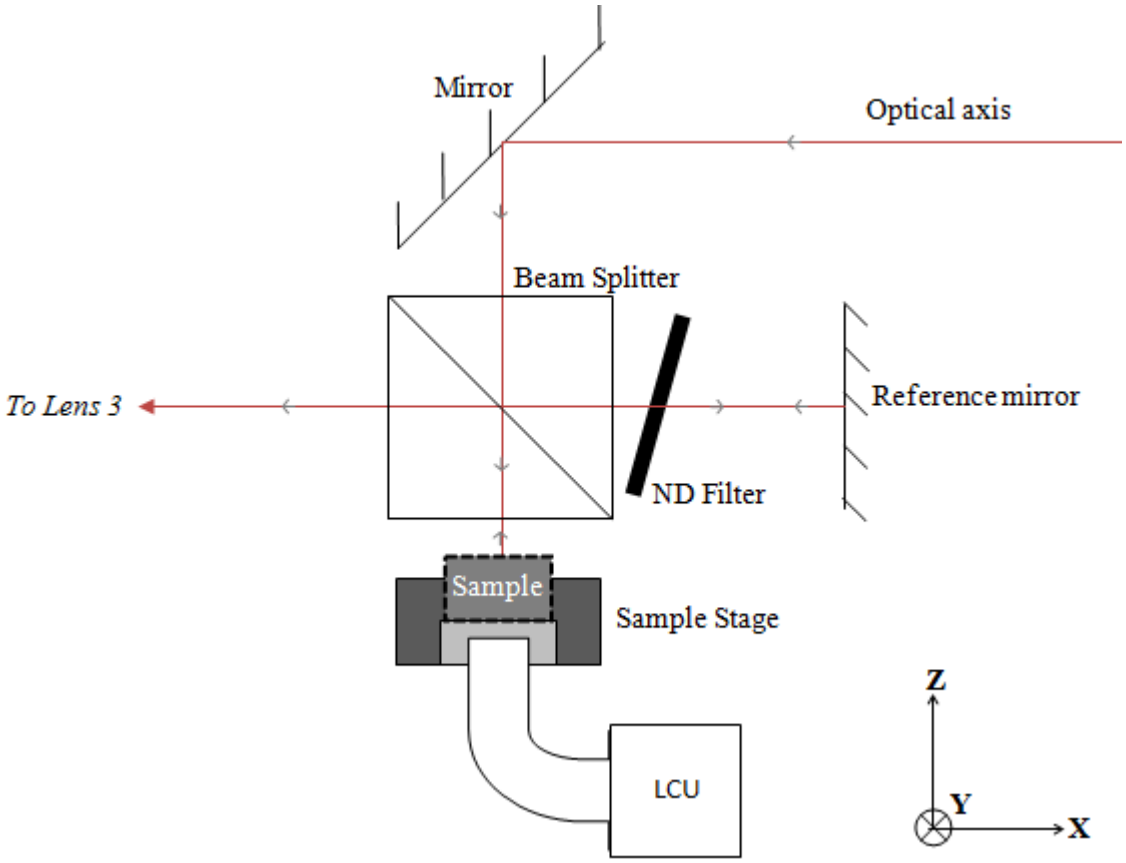

Figure 4 Close up of the Michelson interferometer displayed in Figure 3. The incident laser beam is partially reflected at the beam splitter and directed through the neutral density filter (OD = 0.6) onto the reference mirror (λ/10 surface accuracy). The transmitted laser beam is reflected on the top surface of the sample. The two reflected beams are recombined at the beam splitter and are directed towards lens 3. The LCU was positioned such that when it is turned on the emitted light would illuminate the sample through its quartz disc substrate

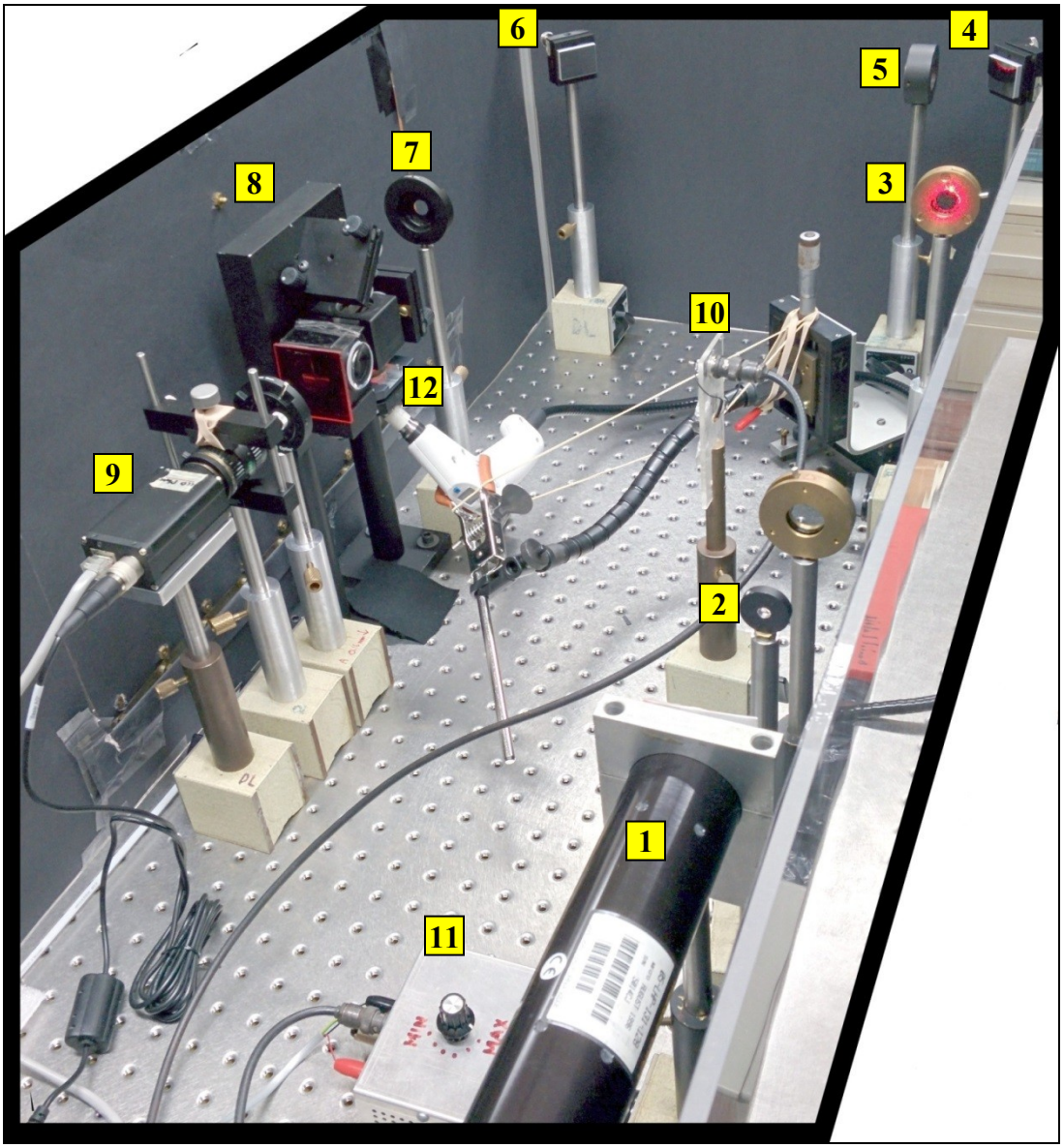

Figure 5 Photograph of the experimental apparatus used to measure the real time axial shrinkage map of light-cured RBC. [1] HeNe laser (632.8 nm). [2] 6 mm focal length plano-convex lens to expand the laser beam. [3] Aperture to block any stray laser light. [4] Plane mirror. [5] 750 mm focal length lens to collimate the laser beam. [6] Plane mirror. [7] Aperture to define the collimated laser beam to a size of 10 mm in diameter. [8] Michelson interferometer. [9] CCD Camera. [10] Si photodiode. [11] Photodiode amplifier. [12] Sample holder and LCU.

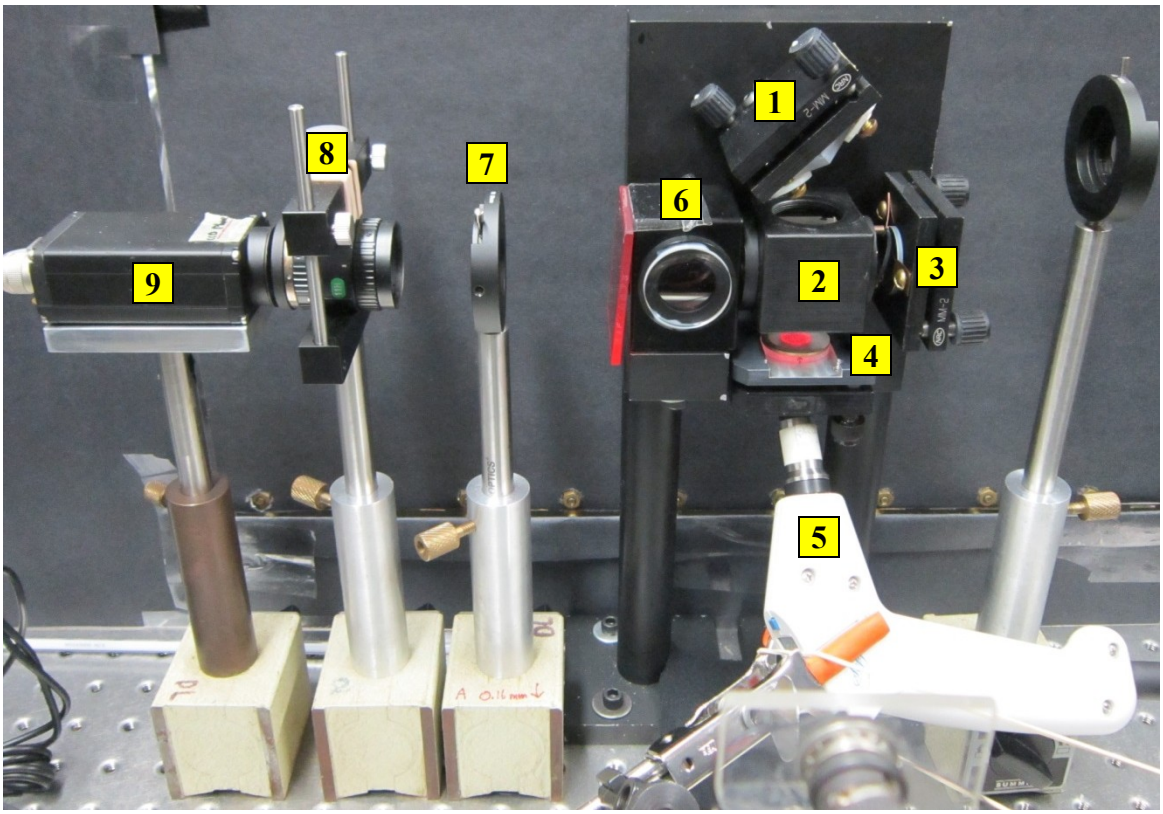

Figure 6 Photograph of the Michelson interferometer. The position of the light curing tip with respect to the sample is clearly visible. [1] Plane mirror. [2] Beam splitter with a 125 mm focal length plano-convex lens and a neutral density filter (OD = 0.6) mounted on its left and right side, respectively. [3] Plane reference mirror (λ/10 surface accuracy). [4] Sample stage with a sample placed inside. [5] Light curing unit with its light guide tip placed right up against the bottom surface of the quartz disc of the sample. [6] Beam splitter with a lens (10 mm focal length) and a red longpass (600 nm cut-off) filter mounted on its front and left side, respectively. [7] Aperture used to prevent stray light from reaching the camera caused by multiple laser reflections and blue light from the curing unit. [8] Camera objective (30 mm focal length; f/1.4) used to reduce the size of the laser beam to fit onto the CCD active area of the camera. [9] CCD camera.

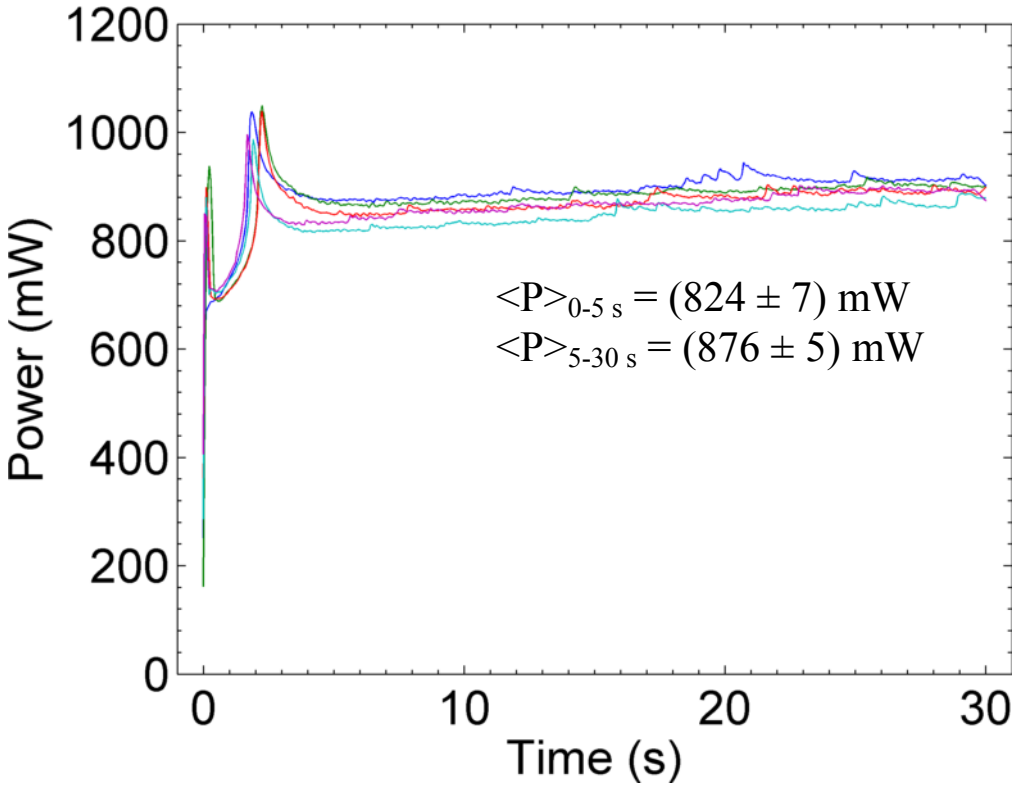

Figure 7 Total light power output as a function of time of the Sapphire® LCU using a standard light guide. A total of 5 measurements are shown. The data was collected using an integrating sphere and an Ocean Optics USB3000 spectrometer. The spectrometer calculated the total power by integrated over the 350 nm to 550 nm spectral range. There is an initial spike in power over the first 10 ms reaching peak value of 893 mW, then dropping down to 704 mW, for the next 2.5 seconds the power rises up to 1026 mW, then taking another 2.5 s to drop down to 858 mW, and thereafter gradually increases to 893 mW. The mean output powers (± standard deviation) over 0 to 5 s and 5 to 30 s intervals for five measurement repeats are 824 mW and 876 mW, respectively. The radiant exposure up to 5 s and 30 s is 4.12 J and 26.1 J, respectively. The radiant exposure was calculated by summing up the power values within the specified time interval and multiplying by the time interval.

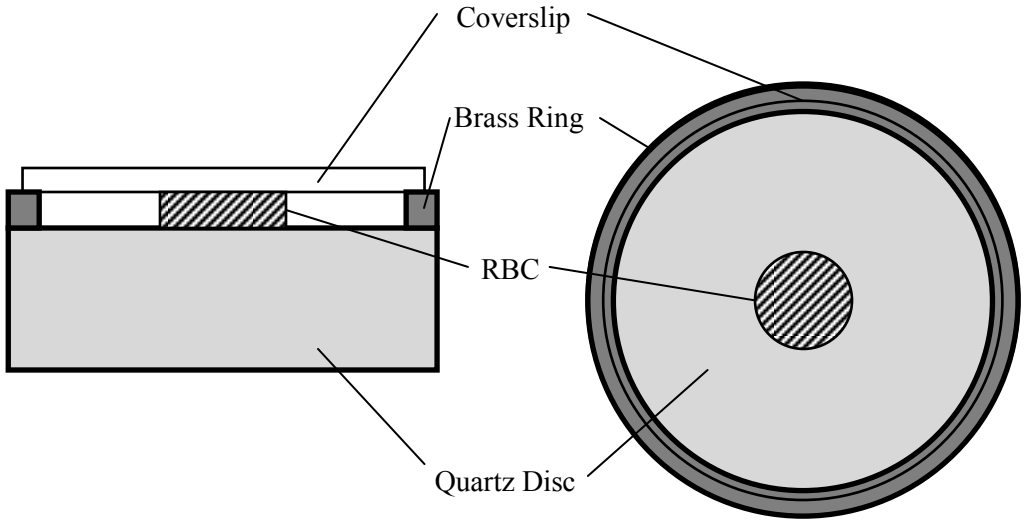

Figure 8 Schematic diagram of the sample geometry used for the axial shrinkage strain measurements. The sample substrate consists of a 3 (or 1.5) mm thick by 25.4 mm diameter quartz disc. A RBC sample with a thickness of 1.22 mm or 1.00 mm and 10 mm diameter is placed at the center of the quartz disc. The brass ring's thickness was 1.22 mm thick except in some experiments where it was 1.00 mm thick in which case it is explicitly mentioned in the results of those experiments. The brass ring thickness defines the sample thickness. The brass ring has an outer and inner diameter of 25.2 mm and 20 mm, respectively. In some experiments the brass ring was not used. The coverslip which provides good sample reflectivity to the laser light is 22 mm in diameter and is either a 100 μm (or 150 μm) thick glass disc or a 25 μm thick Mylar disc.

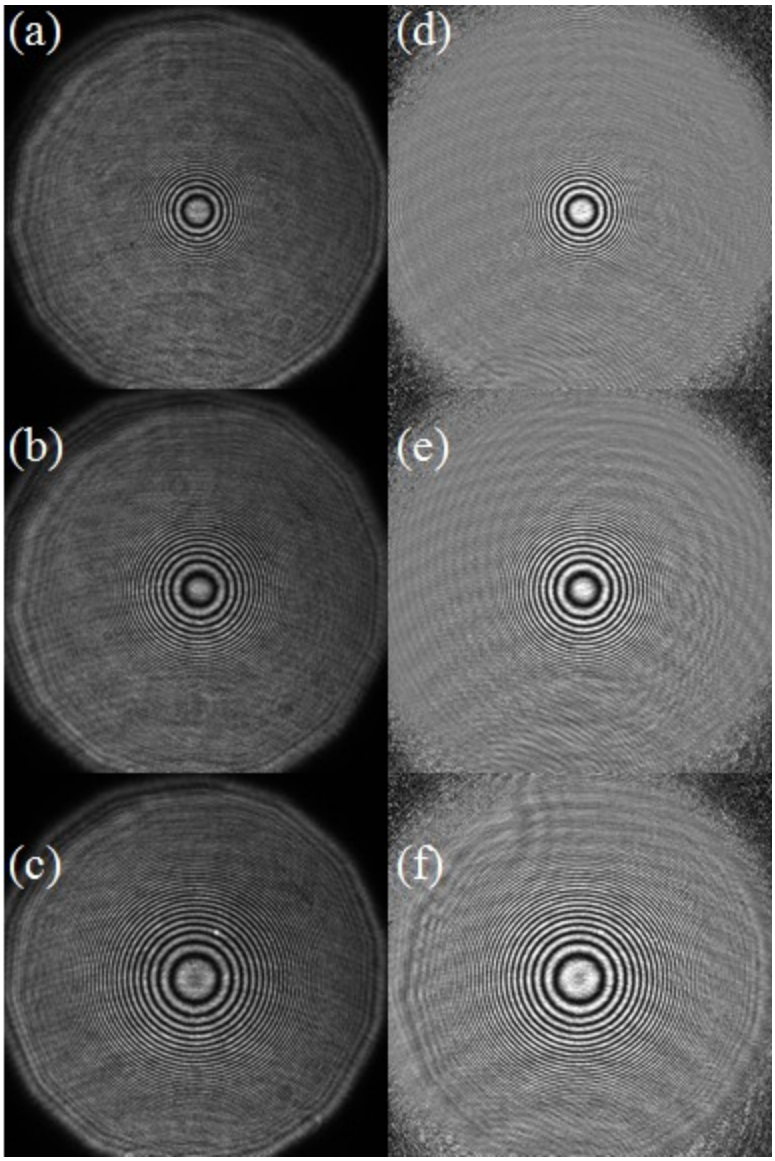

Figure 9 Interference patterns (a-c) produced by three concave spherical mirrors of 8", 12", and 18" focal lengths and measured by the CCD camera. Post-processed patterns (d-f) where the fringe contrast was enhanced. The signal processing carried out on the measured interference pattern canceled out the variations in laser beam irradiance across the image. This was done by collecting the sample and reference beam intensity separately and using them in the two-wave interference equation. Note the circular fringe patterns associated with the axial symmetry of the mirrors. The fringe spacing increases with increasing focal length.

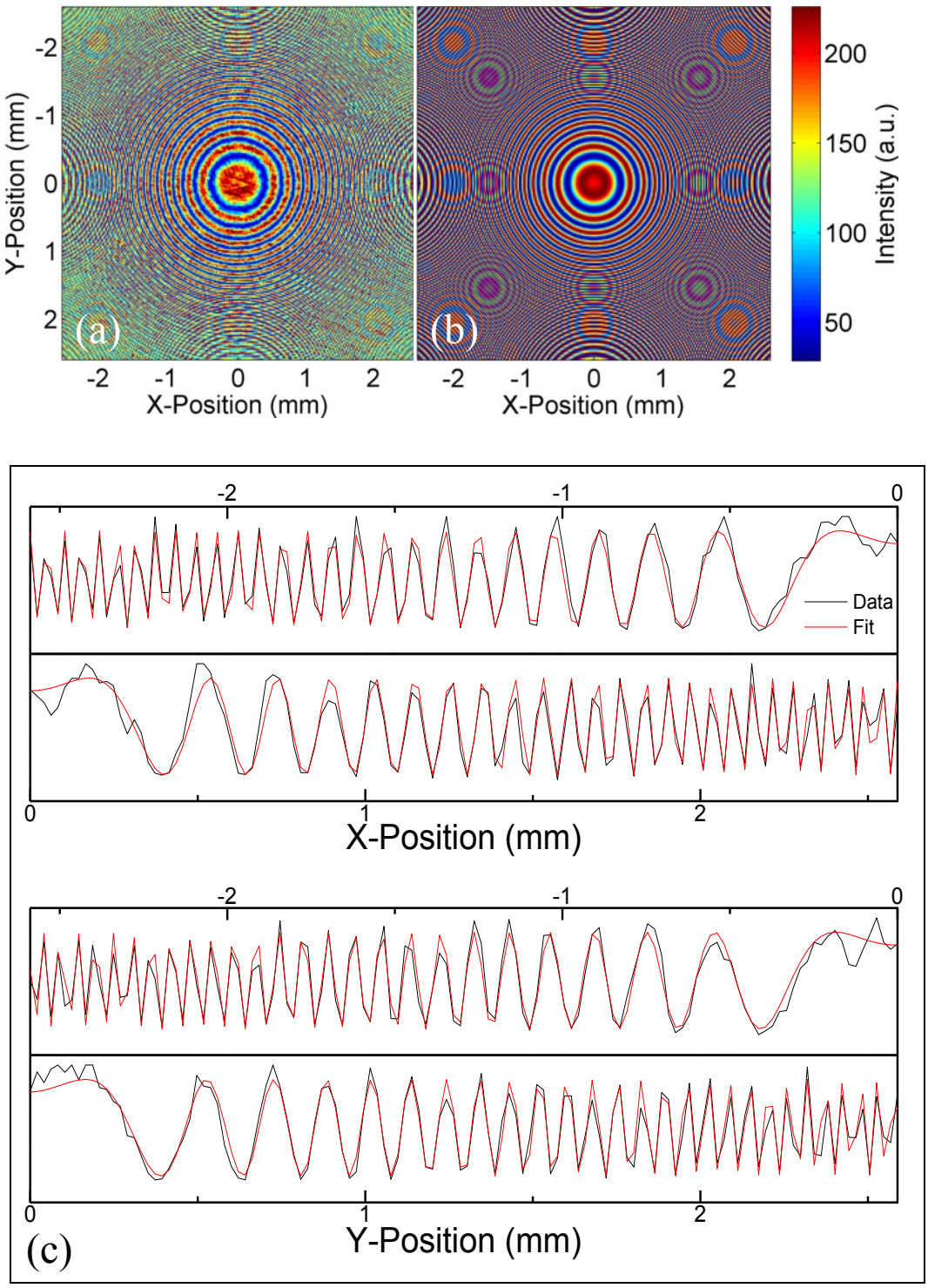

Figure 10 Results from the 2D least-squares fit to the 8" focal length spherical mirror. The original contrast-enhanced interference pattern (a) and the fitted interference pattern (b). Note the circular fringes near the edges are due to image down-sampling induced aliasing effects. (c) Both vertical and horizontal line scans through the center of (a) and (b) overlaid on top of each other. Excellent agreement is found between the data and fit

along both axes between -2.6 and 2.6 mm. Outside this range spatial aliasing of the interferometric pattern occurs. The calculated focal length is 7.98030” ± 0.00002” (0.25% difference from manufacturer’s specified value of 8”). The uncertainty in the fitted focal length is given by the standard deviation determined from the covariance matrix calculated by the fitting program.

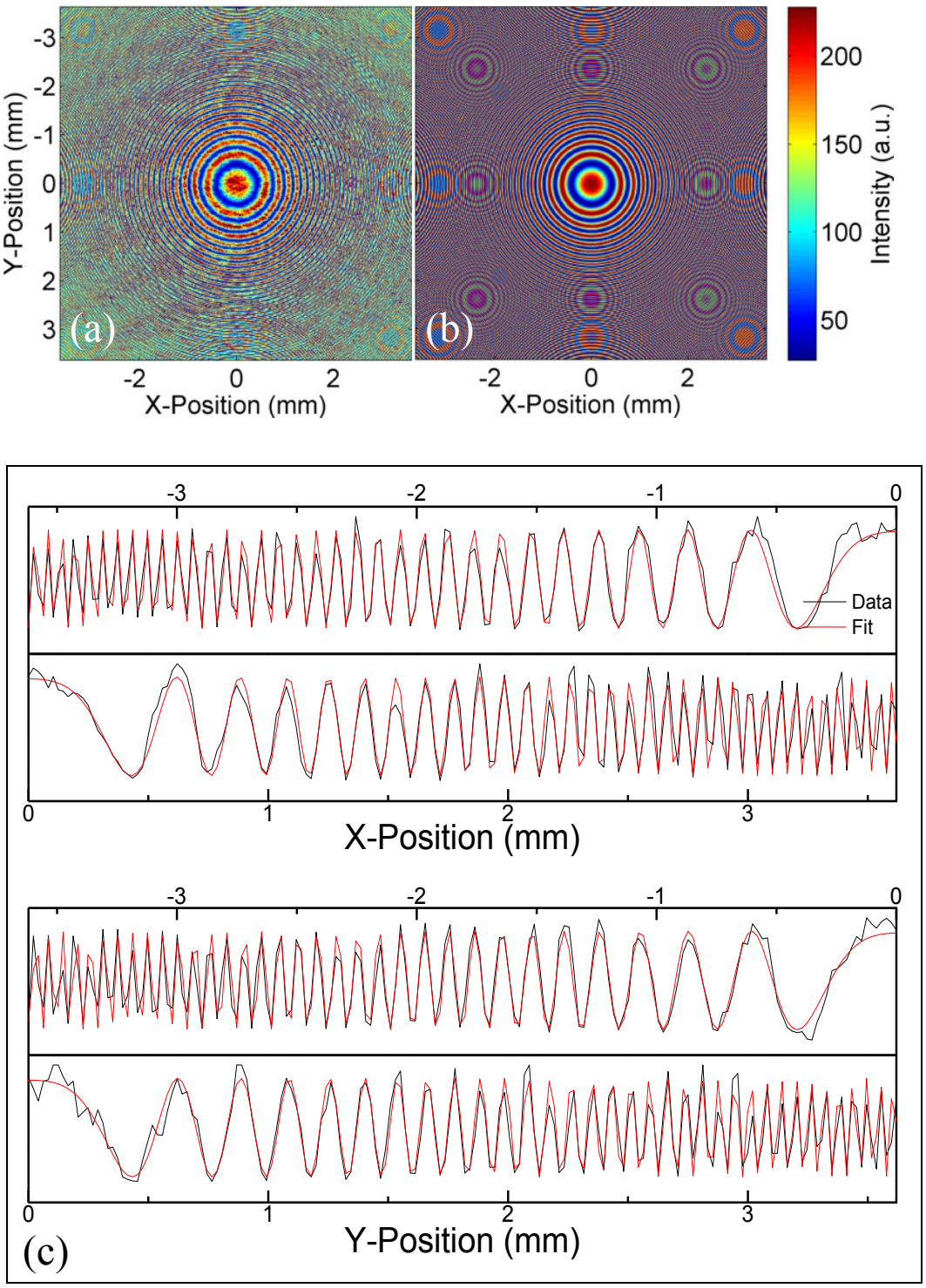

Figure 11 Results from the 2D least-squares fit to the 12" focal length spherical mirror. The original contrast-enhanced interference pattern (a) and the fitted interference pattern (b). Note the circular fringes near the edges are due to image down-sampling induced aliasing effects. (c) Both vertical and horizontal line scans through the center of (a) and (b) overlaid on top of each other. Excellent agreement is found between the data and fit

along both axes between -3.6 and 3.6 mm. Outside this range spatial aliasing of the interferometric pattern occurs. The calculated focal length is 12.20836" ± 0.00003" (1.7% difference from manufacturer's specified value of 12"). The uncertainty in the fitted focal length is given by the standard deviation determined from the covariance matrix calculated by the fitting program.

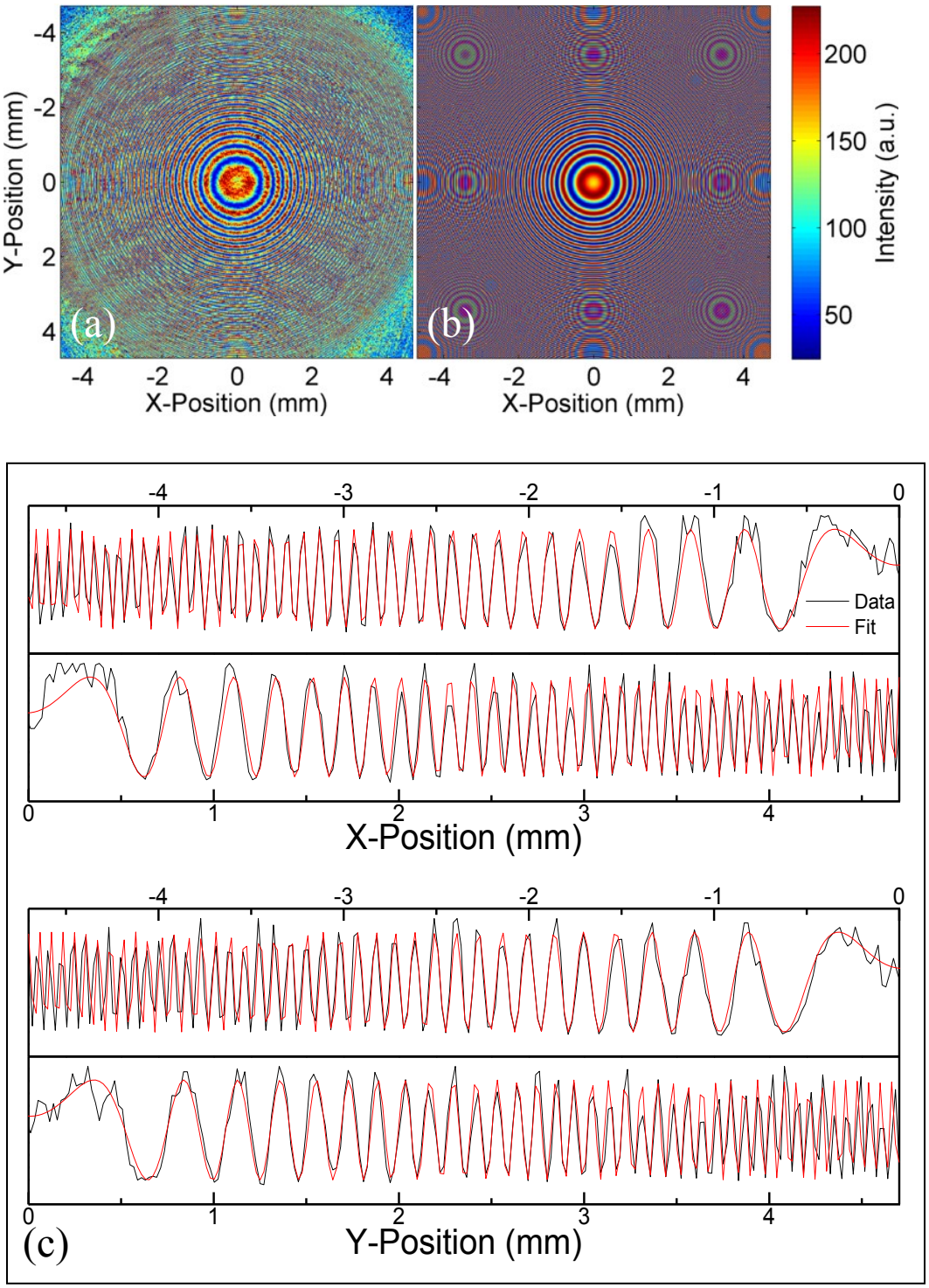

Figure 12 Results from the 2D least-squares fit to the 18" focal length spherical mirror. The original contrast-enhanced interference pattern (a) and the fitted interference pattern (b). Note the circular fringes near the edges are due to image down-sampling induced aliasing effects. (c) Both vertical and horizontal line scans through the center of (a) and

(b) overlaid on top of each other. Excellent agreement is found between the data and fit along both axes between -4.6 and 4.6 mm. Outside this range spatial aliasing of the interferometric pattern occurs. The calculated focal length is 17.60894" ± 0.00005" (2.2% difference from manufacturer's specified value of 18"). The uncertainty in the fitted focal length is given by the standard deviation determined from the covariance matrix calculated by the fitting program.

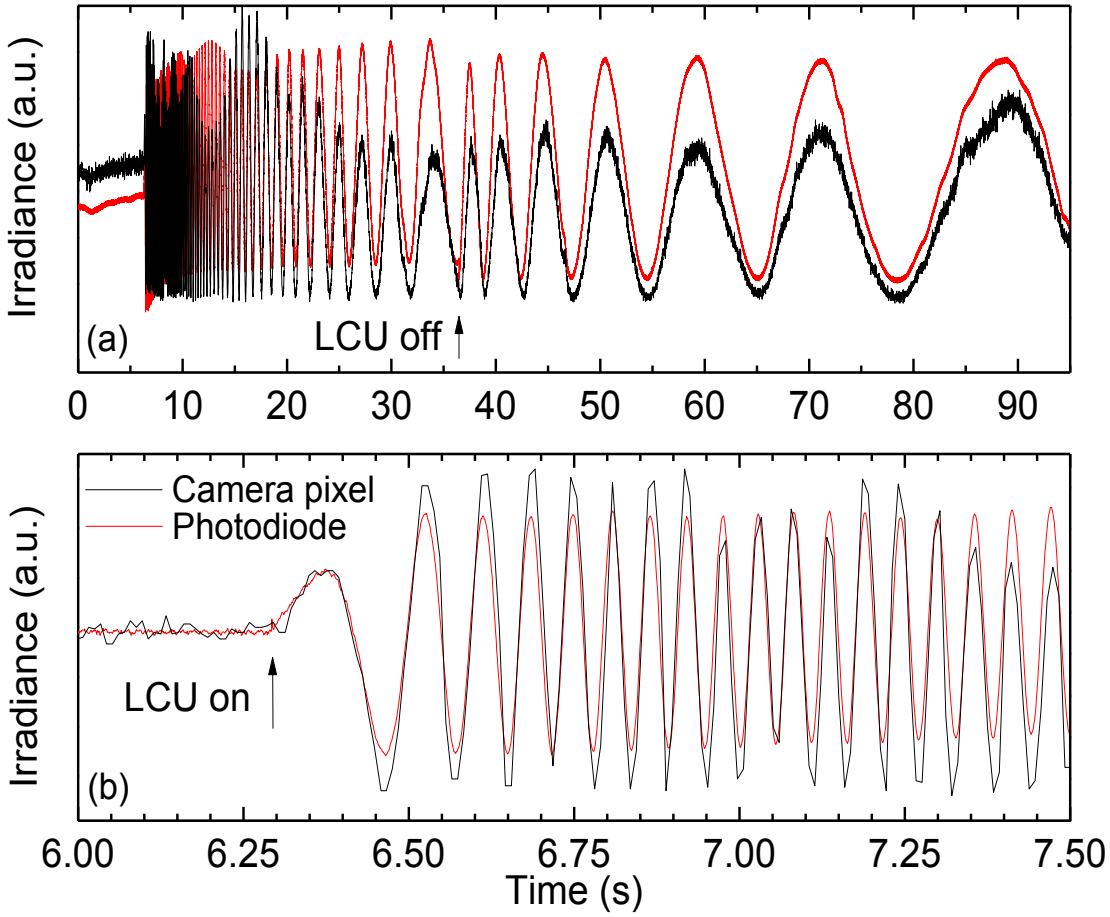

Figure 13 Comparison between a representative interferometric data collected using a photodiode and that measured from a single pixel at the center of the camera during the photopolymerization shrinkage of a typical RBC sample. The sample consisted of a 3mm thick quartz plate, a 1.22 mm thick by 10 mm diameter RBC (Filtek Supreme Ultra CT), a brass ring, and a 100 μm thick glass coverslip. The sample was photo-cured for 30 seconds using a Plasma Arc LCU (Sapphire®) on bleach mode (1.38 W/cm²) with a standard light guide at a temperature of 22 °C. (a) For these measurements, the optical geometry used minimized LCU light from reaching the photodiode. The data displayed were acquired over a 95 s interval. (b) Close up of the data between 6 s and 7.5 s to see the region where the oscillation frequency is at its highest. In Figure 13 (b), the photodiode data was scaled to facilitate a direct comparison with the camera data. Note that the oscillations in laser irradiance recorded by the two methods are in excellent agreement. Axial shrinkage reconstruction is done by locating the minima and maxima in the interferometric data. The separation between two successive minima or maxima corresponds to a sample surface displacement of λ/2. The camera and photodiode acquisition rates were 122 FPS and 1000 samples per second, respectively.

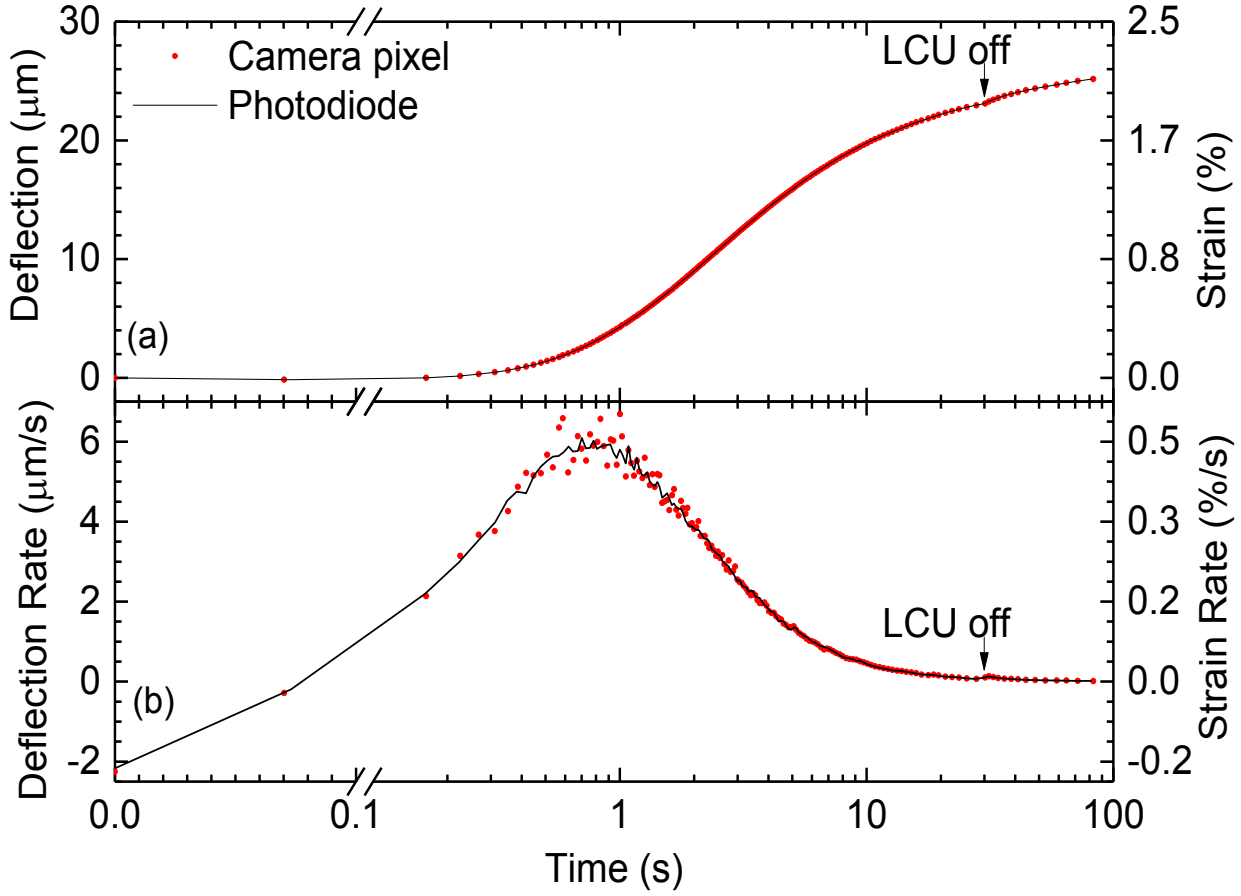

Figure 14 Axial deflection (a) and axial deflection rate (b) as a function of time obtained using the interferometric data from the Si photodiode and CCD camera pixel on the shrinkage of a RBC sample made out of Filtek Supreme Ultra CT. The sample was illuminated by a Plasma Arc LCU (Sapphire®) on bleach mode (1.38 W/cm²) with a standard light guide for an exposure time of 30 s. The sample thickness and temperature were 1.22 mm and 22 °C, respectively. The initial light-induced expansion is observed for times less than 0.1 s where the axial deflection rate is negative. As displayed in (a) and (b) note the excellent agreement between the two sets of data. The appreciable noise observed in Figure 13 (b) for the data obtained from the camera pixel is due to the relatively large uncertainties in the determination of time intervals between successive maxima and minima in the interference pattern. In turn these uncertainties are related to the lower frame rate of 122 FPS for the camera compared to the photodiode amplifier output sampling rate of 1000 data per second. Note the time axis is linear from 0 to 0.1 s and logarithmic thereafter.

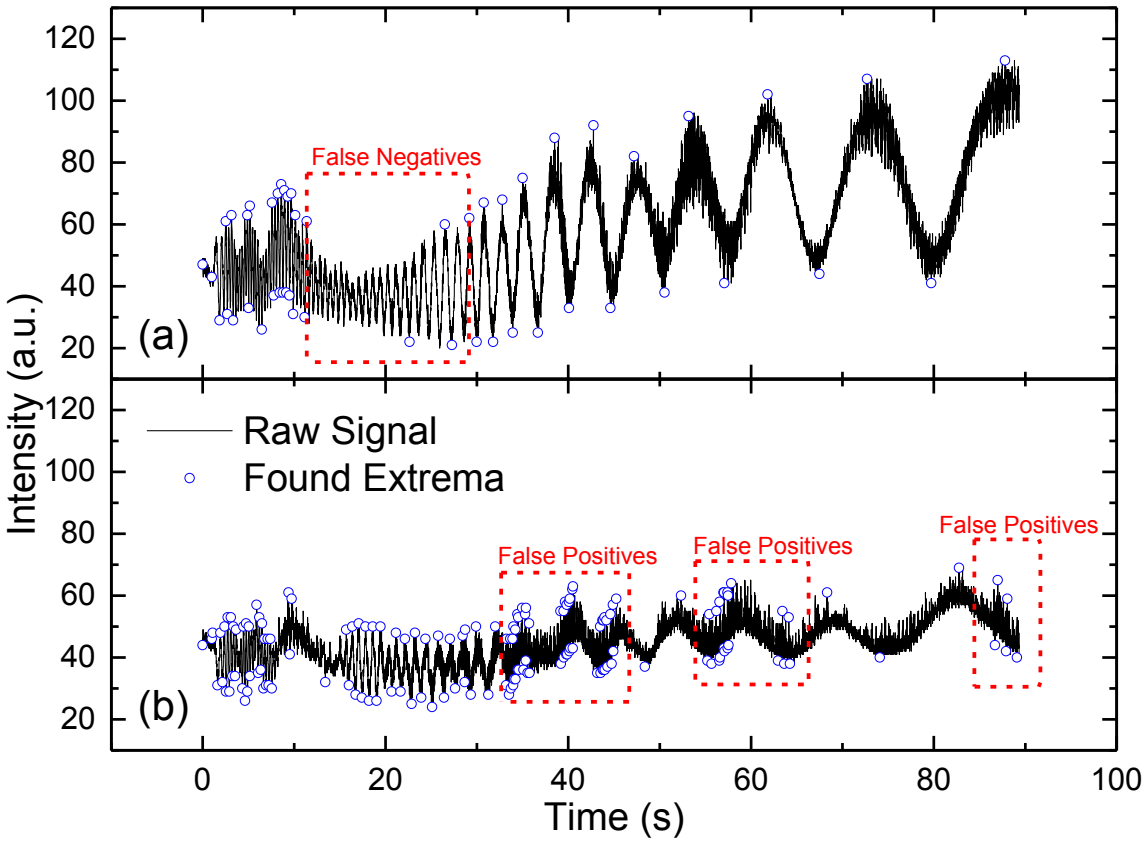

Figure 15 Sources of error in the peak finding algorithm from the interference pattern. Due to noise in the acquired signal the peak finding algorithm may (a) miss actual peaks (false negatives) or (b) falsely detect peaks (false positives). In addition, the time at which the minima or maxima occurs may be off from the actual peak position due to a low data acquisition frequency, especially near regions of high interference pattern oscillation, or noise in the data. The data shown was collected at a time interval of 8.14 ms per data point. Note that in this context "peak" refers to "trough" as well.

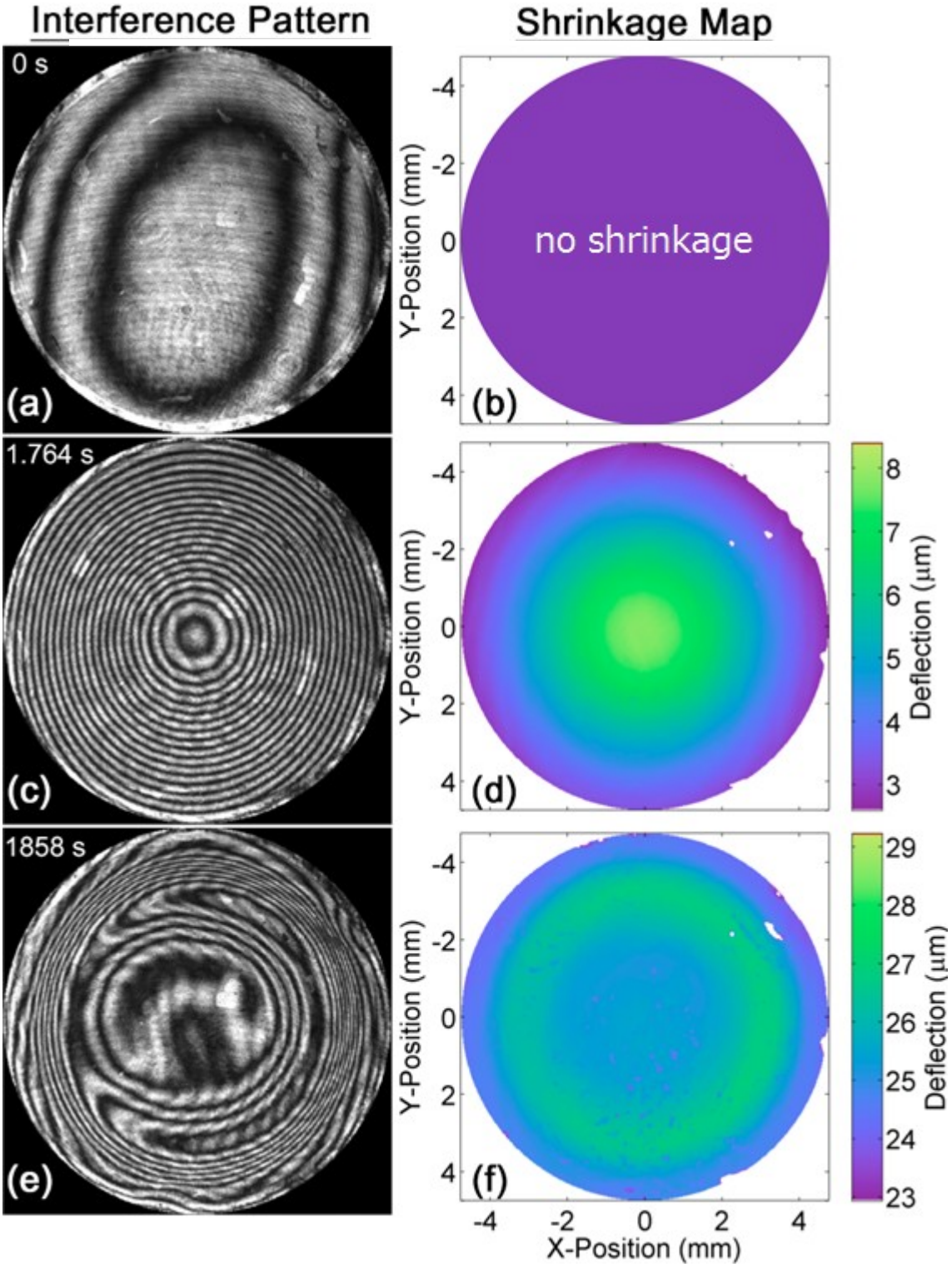

Figure 16 Comparison of interference patterns obtained from the real-time CCD camera video (a, c, e) and corresponding shrinkage map calculated from time = 0 s up until the time displayed (b, d, f). The times chosen for the comparison are at 0 s when the LCU was turned on (a, b), when the RBC sample underwent the highest rate of shrinkage at

1.764 s (c, d), and at the end of the video acquisition 1858 s in (e, f). The photo-cured RBC sample is made out of Filtek Supreme Ultra CT. The sample was illuminated by a Plasma Arc LCU (Sapphire®) on bleach mode (1.38 W/cm²) with a turbo light guide for an exposure time of 30 s. The sample thickness and temperature were 1.22 mm and 22 °C, respectively. A 100 μm thick glass coverslip was used with a brass ring. Note that the shrinkage map is not a reconstruction from the spatial distribution of interference fringes seen in the pattern at the time shown, but rather from the time varying intensity at a given camera pixel as the sample cured.

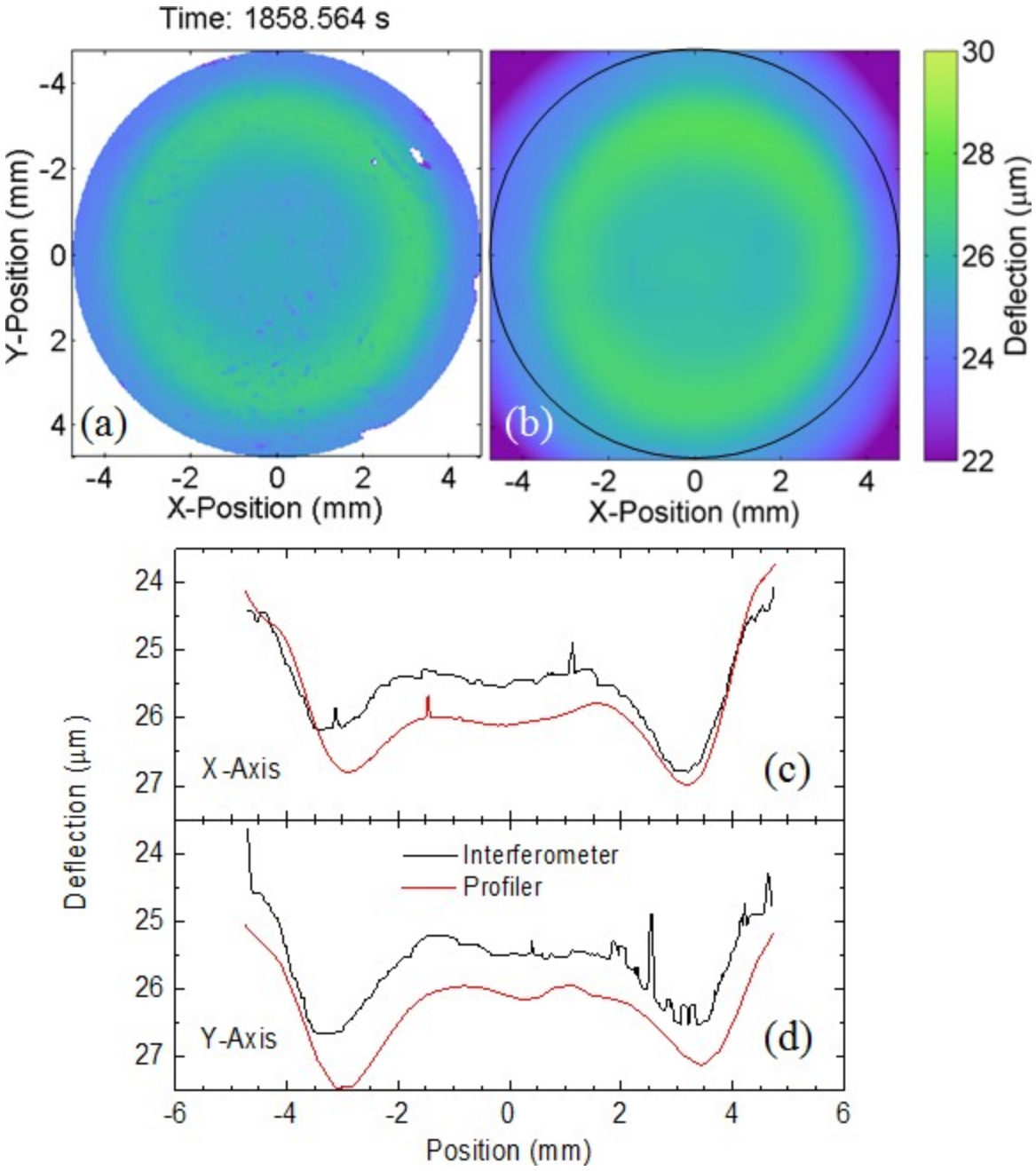

Figure 17 Comparison between the topography reconstructed using the interferometry data (a) and that measured using a profilometer (b). The photo-cured RBC sample is made out of Filtek Supreme Ultra CT. The sample was illuminated by a Plasma Arc LCU (Sapphire®) on bleach mode (1.38 W/cm²) with a turbo light guide for an exposure time of 30 s. The sample thickness and temperature were 1.22 mm and 22 °C, respectively. A 100 µm thick glass coverslip was used with a brass ring. The white areas in Fig 14 (a) indicate the absence of data or data below the minimum value in the color scale. The time indicates the elapsed time since the LCU was turned on. The profiler data collected over a period of 4 hours began 1 hour after those shown in (a). The profiler data shown in (b) were corrected for sample tilt and location of the origin where the shrinkage is zero,

along the inner diameter of the brass ring. The black circle is a guide to the eye for a comparison with the data in (a). Both horizontal (c) and vertical (d) line scans through the center of (a) and (b) are overlaid on top of each other. Note the discrepancy at the center of about 0.5 μm equates to a 2% relative difference from the profilometer data. Considering that the initial sample curvature (about 1 μm) was not subtracted from the profilometer data in (b), the uncertainty related to the orientation of the X and Y axis, and the additional sample shrinkage that occurred between the two sets of measurements, an excellent agreement is found between the interferometry and profiler data.

Table 1 Summary of the 2D least-squares fit to the 8", 12", and 18" focal length spherical mirrors. The manufacturer's (Edmund Optics) part numbers for the mirrors and corresponding focal lengths together with the fitted focal lengths are given. The uncertainty in focal length from the manufacturer's specifications is ±2%. The uncertainty of the fitted focal length is given by the standard deviation determined from the covariance matrix from the fitting program.

Part # of spherical mirror	**Manufacturer's Specification of the focal length (inches)**	**Fitted focal Length (inches)**	**% Difference**
49601	8.00 ± 0.16	7.98030 ± 0.00002	0.25
32818	12.00 ± 0.24	12.20836 ± 0.00003	1.7
32830	18.00 ± 0.36	17.60894 ± 0.00005	2.2

Chapter 3

ROLE OF THE SAMPLE GEOMETRY AND BEAM PROFILE ON THE SHRINKAGE KINETICS DURING AND AFTER LIGHT EXPOSURE

In the conventional bonded disk technique the sample geometry consists of a 3 mm thick glass substrate, a disk shaped RBC sample located at the center of the substrate, a 100 μm thick glass coverslip adhered to the sample and supported at its edge by a 1 mm thick brass ring. With the silanization of the glass surfaces, excellent adhesion between the sample top and bottom surfaces and coverslip and substrate is obtained. The coverslip is necessary to provide a hard surface for contact with the tip of the position sensor. The position sensor monitors the coverslip surface deflection at the sample center and hence the RBC axial shrinkage with time during polymerization.

In the non-contact optical interferometry approach investigated in this thesis, a coverslip is used to flatten the RBC sample and to provide a specular reflecting surface for the laser. The role of the coverslip flexibility and brass ring are studied in this chapter using three different LCU beam profiles. The first beam profile has a good irradiance uniformity of 1.01 W/cm² near the center and with a full width at half maximum (FWHM) of 9 mm while the second and third beam profile have a Gaussian-like shape with a peak irradiance of 15 W/cm² and 85 mW/cm² and FWHM of 2 mm and 0.5 mm, respectively. The third beam profile with a FWHM 20 times less than the sample diameter was selected to study the role of fast and slow curing RBC regions within the sample and their impact on shaping the sample.

Sample exposure to a LCU beam profile induces polymerization and shrinkage of the RBC with time. In turn, the sample pulls on the coverslip where its shape is dictated by its elastic property, RBC viscoelastic properties and its state of polymerization (liquid, gel, or glassy state). Furthermore, the coverslip shape (and RBC sample) is also determined by the brass ring which imposes that no deflection occurs at the coverslip-brass ring contact. The coverslip may also apply a mechanical constraint on the RBC in the liquid or gel state resulting in RBC flow within the sample. As a result, the sample shrinkage strain topography from beginning to end of polymerization is dictated by the LCU beam profile and sample-coverslip interaction. This interaction depends strongly on the coverslip flexibility and whether the coverslip is supported by a brass ring or not.

The following three sections present results on the shrinkage of disk shaped RBC samples using three different sample geometries and irradiance beam profiles. For each of the three beam profiles described above, three sample geometries were used where each sample was covered by a 100 μm thick glass coverslip with and without a supporting brass ring (Geometry #1 and # 2, respectively), and a 25 μm thick Mylar coverslip without a brass ring (Geometry #3). The last section summarizes the findings in this chapter.

3.1 Uniform Beam Profile upon the Shrinkage Kinetics

3.1.1 Results

The irradiance beam profile of the Sapphire® LCU with a standard tip light guide is presented in Figure 18. Total power output of the LCU on bleach mode with this light guide as measured through a 3 mm thick quartz disc was 876 mW. The mean irradiance at the center of the beam profile is 1.04 W/cm² with a peak to peak fluctuation of 0.18 W/cm².

The surface topography of representative RBC samples made with Filtek™ Supreme Ultra CT exposed to the LCU light can be seen in Figure 19. The samples were exposed to the LCU radiation for 30 second. The sample temperature was 22 °C. For Geometry #1 and #2 the shrinkage maps were qualitatively very similar with comparable total deflection values. Near the position values of ±2 mm there is about 1 μm increase in deflection as compared to the center of the sample. For Geometry #3 the shrinkage map was more rounded, did not flatten out near the edges, and did not exhibit the two pronounced local maxima away from the sample center as compared to the maps associated with Geometry #1 and #2. The beam profile matches best with the shrinkage line scan in Geometry #3.

The maximum deflection rates and deflections and their mean values for each of the sample geometries and LCU exposure time can be observed in Figure 20. The values

were measured 90 seconds after the LCU was turned on. Note that for the two data points below the mean value for both Mylar (5s) and Mylar (30s), the sample conditions differed. Rather than the standard 1.22 mm thick brass ring used, a new 1.00 mm thick brass ring was employed instead. All mean values were calculated from the three repeats, except for where it is noted in the figure caption. The maximum deflection rate for the 5 s and 30 s trials should be comparable because they are attained within 1 s from the start of LCU light exposure. Increasing the light exposure from 5 s to 30 s resulted in an increase in the maximum deflection for each sample geometry. Going from glass coverslip with a brass to without one there is an increase in the maximum deflection and deflection rate at 5 s exposure time and a decrease at 30 s exposure time. Since two of the three data points collected using Geometry #3 and at each exposure time were obtained with a 1.00 mm ± 0.01 mm thick brass ring, the values were scaled by multiplying by 1.22 to estimate what the mean deflection and mean deflection rate would be using the 1.22 mm ± 0.01 mm thick brass ring. Upon scaling, the mean deflection and mean deflection rate for 5 s and 30 s exposure time are 24.5 µm ± 0.5 µm and 6.04 µm/s ± 0.1 µm/s and 25.9 µm ± 0.2 µm and 5.860 µm/s ± 0.003 µm/s respectively. The scaled mean deflection for both 5 s and 30 s exposure time is higher than the value obtained with the 1.22 mm ± 0.01 mm thick sample. The scaled mean deflection rate is about the same and lower than the value for the 1.22 mm ± 0.01 mm thick sample for 5 s and 30 s exposure time, respectively.

3.1.2 Discussion

The most striking difference in this experiment is between the Mylar and glass coverslip shrinkage maps and line scans. The results indicate that there is more shrinkage just

outside the center of the sample if using a glass coverslip, but such a trend is not observed for Geometry #3. This phenomenon is briefly discussed here and is later shown to be related to the rigidity of the coverslip. The concept is that faster curing regions caused by a relatively higher irradiance pull the coverslip with them. Due to the rigidity of the coverslip it compresses the slower curing RBC regions still in the pre-vitrified state related to the low irradiance there. In addition to intrinsic polymerization shrinkage there is coverslip induced sample deformation. Note that the flexural rigidity of the 25 μm thick Mylar coverslip is about 1000 times less than that of the 100 μm thick Borosilicate glass coverslip. Due to the high flexibility of the Mylar coverslip, coverslip induced axial deflection was not observed. Consequently, the results shown in Figure 19(i) depict the effect of the finite beam width on the shrinkage maps.

Differences in the shrinkage maps between Geometry #1 and #3 imply that the shrinkage kinetics have been altered. It is important to see if the shrinkage kinetics has changed at the center of the sample in addition to the regions further away from the center of the sample. It was observed that there was a slight change at the center of the sample when using a glass coverslip with or without a brass ring. The change being that the maximum deflection and deflection rate for Geometry #3 was less than for Geometry #1 and #2 by 2.6 μm ± 0.8 μm and 0.09 μm/s ± 0.04 μm/s, respectively. This may be due to a smaller configuration factor (C-factor) in Geometry #3. The C-factor is the ratio of the sample surface bonded to a rigid surface to the area of exposed surface. The larger the C-factor the more the linear shrinkage strain approximates the volumetric shrinkage strain [40,41]. Due to the Mylar's flexibility, it is possible that it does not restrict in-plane shrinkage

near the sample surface to the extent that it does for the glass coverslip thus reducing the C-factor and the linear shrinkage.

Two of the three data points for Geometry #3 were collected with a 1.00 mm instead of 1.22 mm thick sample. For comparison with the 1.22 mm thick sample data the 1.00 mm thick sample data was multiplied by 1.22. The 1.22 mm thick sample case requires another two measurements in order to get better statistics to draw a stronger conclusion. For example, to see of there's an effect on the shrinkage kinetics from the difference in the C-factor.

3.2 High Irradiance Small Diameter Beam Profile upon the Shrinkage Kinetics

3.2.1 Results

The irradiance beam profile of the Sapphire® LCU with a turbo tip light guide is presented in Figure 21. Total power output of the LCU on bleach mode with this light guide as measured through a 3 mm thick quartz disc was 510 mW and maximum irradiance was 15 W/cm². Note that the beam profile FWHM of 2.0 mm was five times smaller than the RBC sample diameter.

Surface topography of representative RBC samples made with Filtek™ Supreme Ultra CT exposed to the LCU light are depicted in Figure 22. The sample temperature was 22 °C. For the two geometries using a glass coverslip with and without a brass ring the shrinkage maps are similar with comparable total deflection values. The shrinkage maps

at the maximum shrinkage rate time of 0.5 – 0.6 s are qualitatively correlated with the irradiance beam profile of the turbo light guide, especially for Geometry #3. At the final acquisition time for Geometry #1 and #2 there is 2 μm more deflection at ±3 mm than at 0 mm. The shrinkage map in Geometry #3 at the final acquisition time shows the two pronounced local maxima at ±3 mm from the center of the sample as it does for Geometry #1 and #2, but the global maximum is maintained at the center. Near the edge of the sample (radius >4 mm) the deflection decreases more rapidly than it does for Geometry #1 and #2.

The maximum deflection rate and maximum deflection for each of the sample geometries and experimental conditions are shown in Figure 23. The maximum deflection was measured 90 s after the LCU was turned on. Except for where noted in the figure caption all mean values were calculated from three repeats. Due to the small number of repeats rather than providing error bars calculated from standard deviation, the mean deflection value, mean deflection rate value, and sample values are shown in Figure 23 to display the range in the measured results. The mean maximum deflection rate for the three sample geometries are the same within the sample distribution. The mean maximum deflection of Geometry #3 is about 1 μm ± 1 μm lower than the other two geometries.

3.2.2 Discussion

In addition to the standard light guide, using the turbo light guide further elucidates the role of the coverslip rigidity. The local maxima in the shrinkage profile at ±3 mm are even more pronounced compared to when using the standard light guide. A schematic

diagram depicting the effects of the coverslip rigidity induced deformation on the RBC sample in the bonded disc geometry is shown in Figure 24. For a uniform illumination of the RBC by the LCU depicted in Figure 24 (a-c), the sample is expected to shrink uniformly across the entire surface with time since the rate of polymerization is the same everywhere across the surface. For a non-uniform illumination displayed in Figure 24 (d-f), such as by using a turbo light guide, the central region of the RBC sample initially cures and shrinks faster than the surrounding RBC. The coverslip deflects at the center then, due to its high flexural rigidity, presses on, deforms, and displaces the peripheral RBC still in the pre-vitrified state. The lower the RBC degree of curing, the less viscous it is so it conforms more readily to the applied pressure from the bending coverslip. After the RBC's central part is mostly cured, the surrounding parts continues polymerization induced shrinkage at a decreasing rate until reaching a maximum deflection greater than that of the central part. In contrast, Mylar coverslip rigidity is very low. Thus RBC away from the central fast curing region is unaffected. This resulted in the most shrinkage at the center of the RBC and then decreased towards the edge - as would be intuitively expected given the beam profile. The results obtained in Section 3.1 and 3.2 that use a glass coverslip likely exhibit some coverslip rigidity induced deformation on the RBC sample since even for the standard light guide the irradiance drops off near the sample edge. Especially, for the turbo light guide it can be seen that off-center there is more shrinkage than at the center of the sample.

Comparing the results for the maximum deflection and maximum deflection rate at the center of the sample shows that there is not an appreciable difference between the three

geometries. This may be a result of the fastest curing region of the sample affecting the slower curing regions. The use or not of a brass ring in the glass coverslip conditions does not make any striking difference. This is attributed to the high shrinkage stress applied by the sample onto the coverslip compared to the rigidity of the coverslip. For instance, a 25 mm diameter by 3 mm thick quartz substrate was observed to bend by 0.8 μm from center to edge after photopolymerization of a 1.22 mm thick by 10 mm diameter RBC sample. Following the plate bending calculation approach used by Watts *et al.* [38], for a 27 μm deflection of a 20 mm diameter by 100 μm thick glass coverslip about 0.3 kPa is required; for a 0.8 μm deflection of 25 mm diameter by 3 mm thick quartz substrate about 90 kPa is required. For both calculations a Young's modulus of 70 GPa and Poisson's ratio of 0.3 was used. Based on the estimates, the very high shrinkage stress generated by the RBC during curing can easily bend the glass coverslip to conform to the sample topography. For comparison, the Young's modulus of dentine and enamel is 15 GPa and between 40 to 80 GPa, respectively [82].

3.3 Low Irradiance Small Diameter Beam Profile upon the Shrinkage Kinetics

3.3.1 Results

Irradiance beam profile of the Sapphire® LCU obtained with a standard light guide and a 250 μm diameter aperture attachment placed on the light guide tip is depicted in Figure 25. Total power output of the LCU on bleach mode with this light guide as measured through a 3 mm thick quartz disc was 201 μW. The beam full width at half maximum was 0.5 mm.

Presented in Figure 26 is the surface topography of representative RBC samples made with Filtek™ Supreme Ultra CT exposed to the LCU light for 720 s at a sample temperature of 22 °C. The two sample conditions tested were 100 μm and 150 μm thick glass coverslips with a brass ring. Near the beginning of photopolymerization the shrinkage maps qualitatively correlated with the beam profile where the highest shrinkage was found near the center. At the end of data acquisition for both sample conditions the sample shrinkage line scans have the characteristic "w" shape where low shrinkage occurs at the center and the highest shrinkage is observed near ±2.5 mm from the center of the sample. The valley to peak deflection of 5 μm is the same for both coverslip thicknesses. There was minimal shrinkage towards the edges of the sample.

Displayed in Figure 27 is the surface topography of representative RBC samples made with Filtek™ Supreme Ultra CT exposed to the LCU light for 720 s. The two sample conditions of 100 μm and 150 μm thick glass coverslips without a brass ring were used. The sample temperature was 22 °C. Near the beginning of photopolymerization the shrinkage maps qualitatively correlated with the beam profile where there is the highest shrinkage near the center and less towards the edge of the sample. At the end of data acquisition for both sample conditions the sample shrinkage qualitatively appears similar with lowest shrinkage at the center and greater shrinkage further away from the center.

The surface topography of a representative RBC sample made with Filtek™ Supreme Ultra CT exposed to the LCU light for 720 s for the sample geometry of 25 μm thick

Mylar coverslip is displayed in Figure 28. The shrinkage map shows distinct features at the time for the maximum deflection rate, intermediate time, and final acquisition time. At 29 s the shrinkage map is most correlated with the irradiance beam profile of the LCU where the shrinkage line scans FWHM is 1.2 mm. This is to be compared to a FWHM of 0.5 mm for the beam profile. At 258 s the shrinkage near the center exhibits a flat region 1.2 mm wide and a FWHM of 2.2 mm. At 845 s a small "w" shape is barely discernible in the line scan near the center of the shrinkage map with the local maxima at ± 0.5 mm. When data collection time is increased from 257 s to 845 s there is an additional shrinkage of 2 μm at ± 4 mm. Finally, at the time of 845 s the FWHM for the shrinkage line scans was 5 mm. The broadening of the shrinkage line scans with time is attributed to light scattering of the incident LCU beam as it propagates through the sample. The scattering of the light redistributed optical power throughout the sample thus promoted additional photopolymerization of the RBC in the sample's periphery. After each experiment, the coverslip was removed and the uncured RBC still in the pre-vitrified state was scraped off exposing the cured RBC disc-shaped sample with a typical diameter of 4.2 mm.

The maximum deflection rate and deflection for each of the sample geometries and experimental conditions are shown in Figure 29. The maximum deflection was measured at the end of acquisition, 845 s after the LCU was turned on. Except for where noted in the figure caption all mean values were calculated from three repeats. Due to the small number of repeats rather than providing error bars calculated from the standard deviation of the sets of data - the mean deflection value, mean deflection rate value, and sample

values are displayed. The mean maximum deflection rate and mean maximum deflection for Geometry #1 and #2 and for each coverslip thickness appears to be approximately the same value to within the apparent sample variance. The mean maximum deflections for all three geometries are approximately the same value to within the apparent sample variance. However, the mean maximum deflection rate for Geometry #3 is approximately twice as large as for those obtained using the other two geometries.

3.3.2 Discussion

The conditions selected for this experiment were tailored specifically towards observing the dramatic effects caused by the coverslip rigidity and use of a supporting brass ring on the shrinkage map of cured RBC samples. To attain the desired photopolymerization condition, an aperture was used with a 250 μm opening placed at the tip end of the standard light guide. The experiment was designed so that at a distance of 3 mm away from the aperture the FWHM of the irradiance beam profile was only 0.5 mm. This beam profile was used to induce a relatively high curing rate in a small area near the center of the sample of RBC. By adding the aperture to the standard light guide the total output power decreased by a factor of 4360 compared to that without the aperture. At this much lower irradiance the deflection rate also decreased substantially by a factor of approximately 140. As well, the time for which the maximum deflection rate occurs increased from 0.9 s to 60 s for sample geometry #1 and a 100 μm thick glass coverslip. Under these conditions, as photopolymerization and shrinkage strain developed with light exposure, the center of the sample started pulling on the rigid glass coverslip. In turn, the

coverslip gradually applied a pressure on the RBC. This pressure is partially relieved by the RBC still in the liquid or gel state by a momentary outward flow of the RBC.

The important aspects in the deflection data are observed from a comparison between the shrinkage maps obtained using Geometry #1 and #2 and the 100 μm and 150 μm thick coverslips. Near the center of the samples and for radial positions less than 2 mm, all samples displayed a minimum in deflection with comparable values 9-11 μm. Outside the sample central region radial dependence of the deflection depends upon the geometry. For Geometry #1 where a brass ring is used to support the glass coverslip, a w-shaped deflection is observed with a valley-to-peak deflection of 5 μm. Note that a zero deflection is obtained at the ring-coverslip contact. However, for Geometry #2 where there is no supporting ring used, the deflection keeps increasing with increasing radial position. The general trend of these data does not depend on the thickness of the coverslip where the 150 μm thick coverslip has 3.4 times the flexural rigidity of the 100 μm thick coverslip. The above results are in excellent agreement with the model presented in Figure 24 where coverslip induced stress on the RBC and stress relief through RBC flow still in the liquid or gel state occurs.

Sample geometry #3 was used to further investigate the role of the coverslip flexural rigidity on the shrinkage maps of disc shaped RBC samples. A 25 μm thick Mylar coverslip was used because its flexural rigidity is 1000 times smaller than that for the 100 μm thick glass coverslip. The coverslip induced stress on the RBC and stress release through RBC flow was observed from a comparison between the shrinkage maps

collected using the three sample geometries. As shown in Figure 28(c), the maximum shrinkage is at the center, except for a little less at the final time, and shrinkage is lower away from the center. The shrinkage profiles also more closely resemble the beam profile and no coverslip induced deformation of the RBC at the sample's peripheral is observed. Note the broadening of the shrinkage line scans with time. This is attributed to light scattering of the incident LCU beam as it propagated through the sample. The scattered light promoted additional photopolymerization and hence shrinkage. At the final time there is still a small "w" shape in the deflection line profile showing two off-center local maxima. These maxima may be due to coverslip induced stress on the RBC and release through RBC flow except on a smaller scale compared to that observed in Geometry #1 and #2. This suggests that the characteristic "w" shape becomes smaller in scale with decreasing coverslip rigidity.

The mean maximum deflection for all sample geometries is the same to within the variance of the data. However, the mean maximum deflection rate for Geometry #3 is approximately two times greater than that for the glass coverslip cases. This is very interesting since it appears that regardless of the shrinkage rate, the maximum shrinkage is approximately the same. The mean maximum deflection rate for samples in Geometry #1 and #2 is smaller than those for Geometry #3. This may be due to the pre-gel RBC shrinkage stress being too low to deflect the rigid glass coverslip whereas Mylar is sufficiently compliant.

3.4 SUMMARY

It was shown that the maximum deflection and maximum deflection rate measured at the RBC sample centers were found to be qualitatively the same within the sample variance for the three sample geometries and typical light exposure conditions, such as the PAC unit set on bleach mode and using either a standard or turbo light guide. However, the shrinkage kinetics monitored off the sample center depends upon both the sample geometry and beam profile from the LCU used for photopolymerization. The glass coverslip induces extra axial deflection towards the RBC's periphery due to a central fast curing region causing the bent coverslip to apply a downward pressure on the pre-vitrified RBC. This causes off-center RBC to deform radially and axially in addition to photopolymerization induced axial shrinkage thus exhibiting a total axial deflection at the sample's periphery to be larger than at its center. This pattern was observed for Gaussian-like shaped LCU irradiance beam profiles due to higher curing rate at the sample center. The very small flexural rigidity of the Mylar coverslip allows the shrinkage map to conform to the RBC's surface without applying a deformation inducing force on it. At low LCU light exposure irradiance the viscoelastic properties of the RBC becomes significant. The shrinkage kinetics is affected throughout the sample surface by the coverslip rigidity and brass ring. At the 201 μW LCU power and peak irradiance of 85 mW/cm², the mean maximum deflection rate is twice as high for Geometry #3 as compared to Geometry #1 and #2 and the mean maximum deflection was approximately the same. This work suggests that for the bonded disc geometry the coverslip should be a 25 μm thick Mylar coverslip to get accurate shrinkage map measurements for the RBC. A

100 μm thick glass coverslip may only be used if the LCU irradiance beam profile is uniform across the sample surface. The exception is that at low LCU irradiance and for a bell-shaped beam profile the shrinkage kinetics are affected by the glass coverslip so a Mylar coverslip should be used instead. The possibility of a reduction in the C-factor of the sample when using Mylar instead of a glass coverslip should be considered.

3.5 Figures and Tables

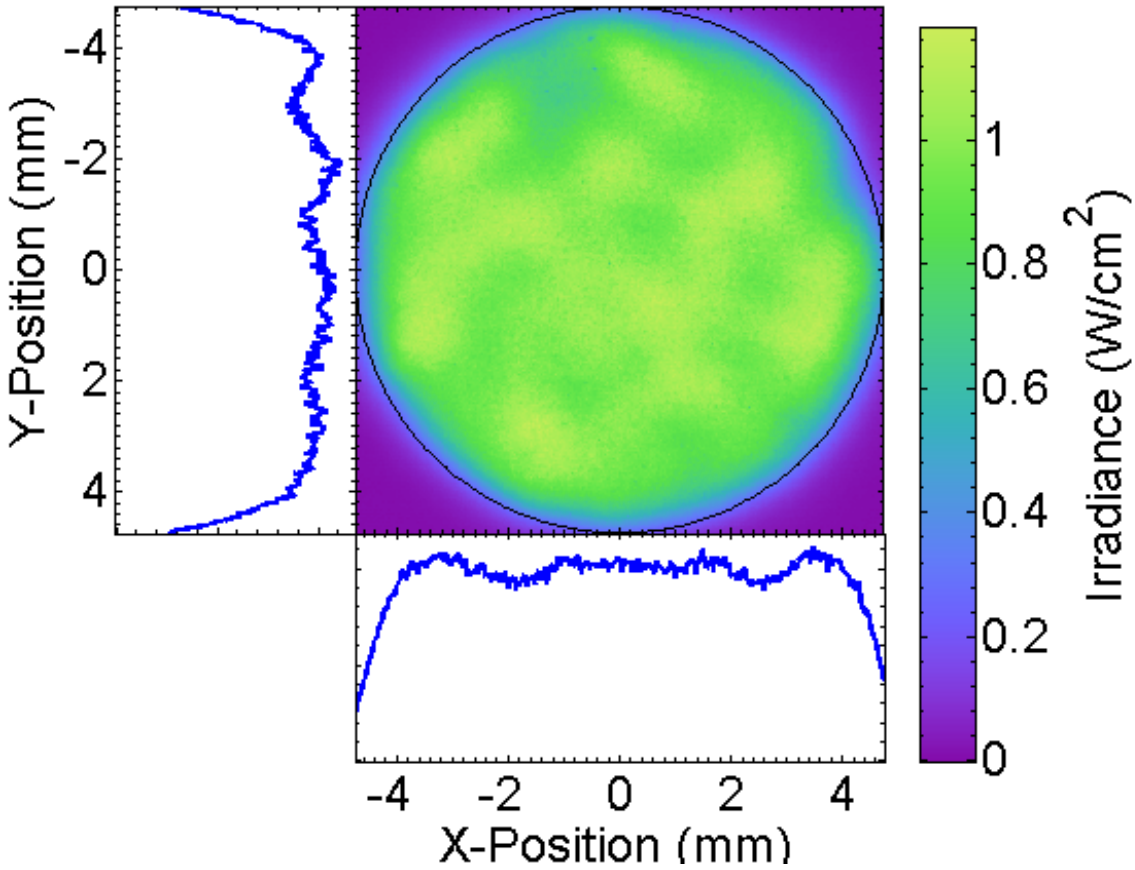

Figure 18 Irradiance beam profile of the Sapphire® LCU with a standard light guide on the bleach mode setting. Total power output was 876 mW and the beam profile full width at half maximum was 9 mm. The blue-colored y-, x- line scans (left-side and bottom plots) are profiles through the center of the 2D beam profile. The mean irradiance at the center is 1.04 W/cm² with a peak to peak variation of 0.18 W/cm². The line scan and colorbar irradiance maximum and minimum value is 1.17 W/cm² and 0 W/cm², respectively.

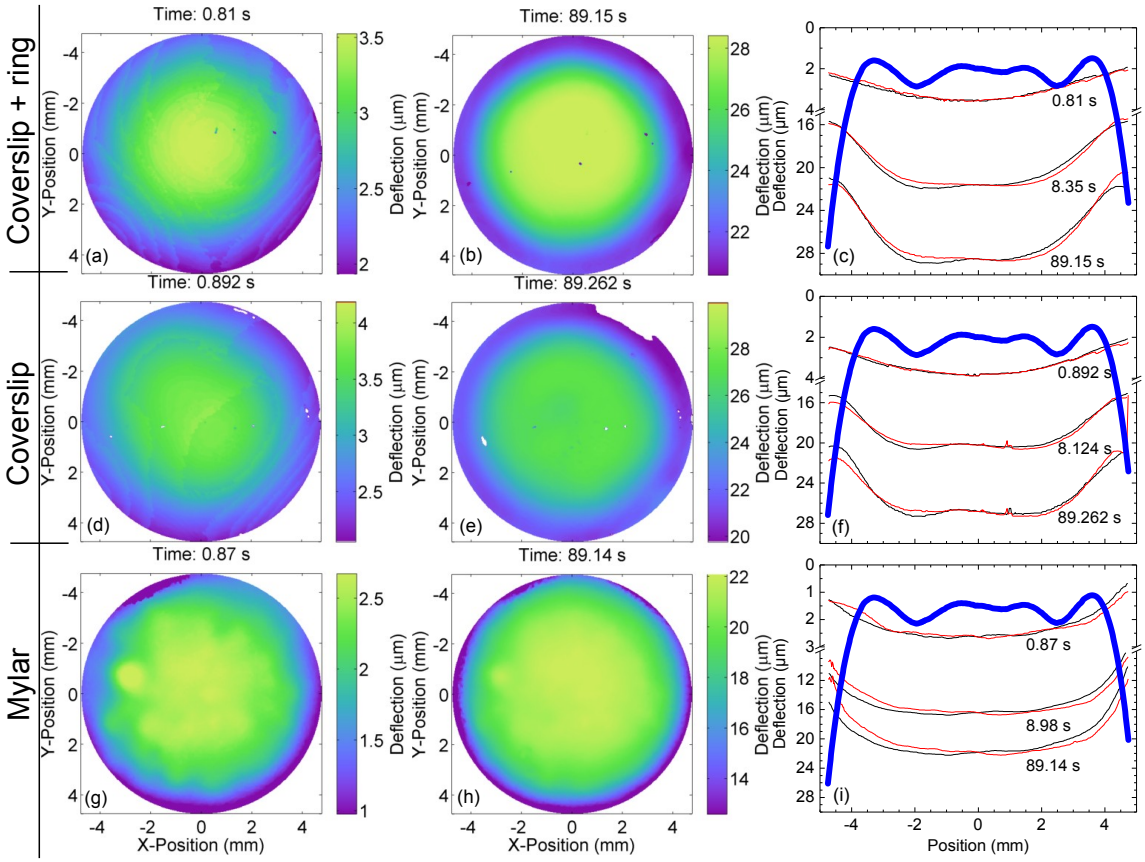

Figure 19 Surface topography of RBC samples made with Filtek™ Supreme Ultra CT cured by a Sapphire® LCU using a standard light guide set on bleach mode for 30 seconds. The sample temperature was 22°C. The three sample geometries used were with a 100 µm thick glass coverslip with a brass ring (a-c), 100 µm thick glass coverslip without a brass ring (d-f), and 25 µm thick Mylar coverslip without a brass ring (g-i). The surface topographies where the sample shrinkage rate at the center was at a maximum (a,d,g) and at the end of acquisition (b,e,h) are displayed. Horizontal (red line) and vertical (black line) line profiles (c,f,i) passing through the center of the sample shrinkage map are shown. Note the broken vertical axis. The data collection time for each of the line profile is given next to it. The semi-transparent blue line (c,f,i) is the x-line scan through the center of the LCU 2D beam profile. The white areas in the 2D maps indicate the absence of data or data below the minimum value in the color scale. Note that for the sample with a Mylar coverslip (g-i) the sample thickness was 1.00 mm instead of 1.22 mm that was used for the other samples.

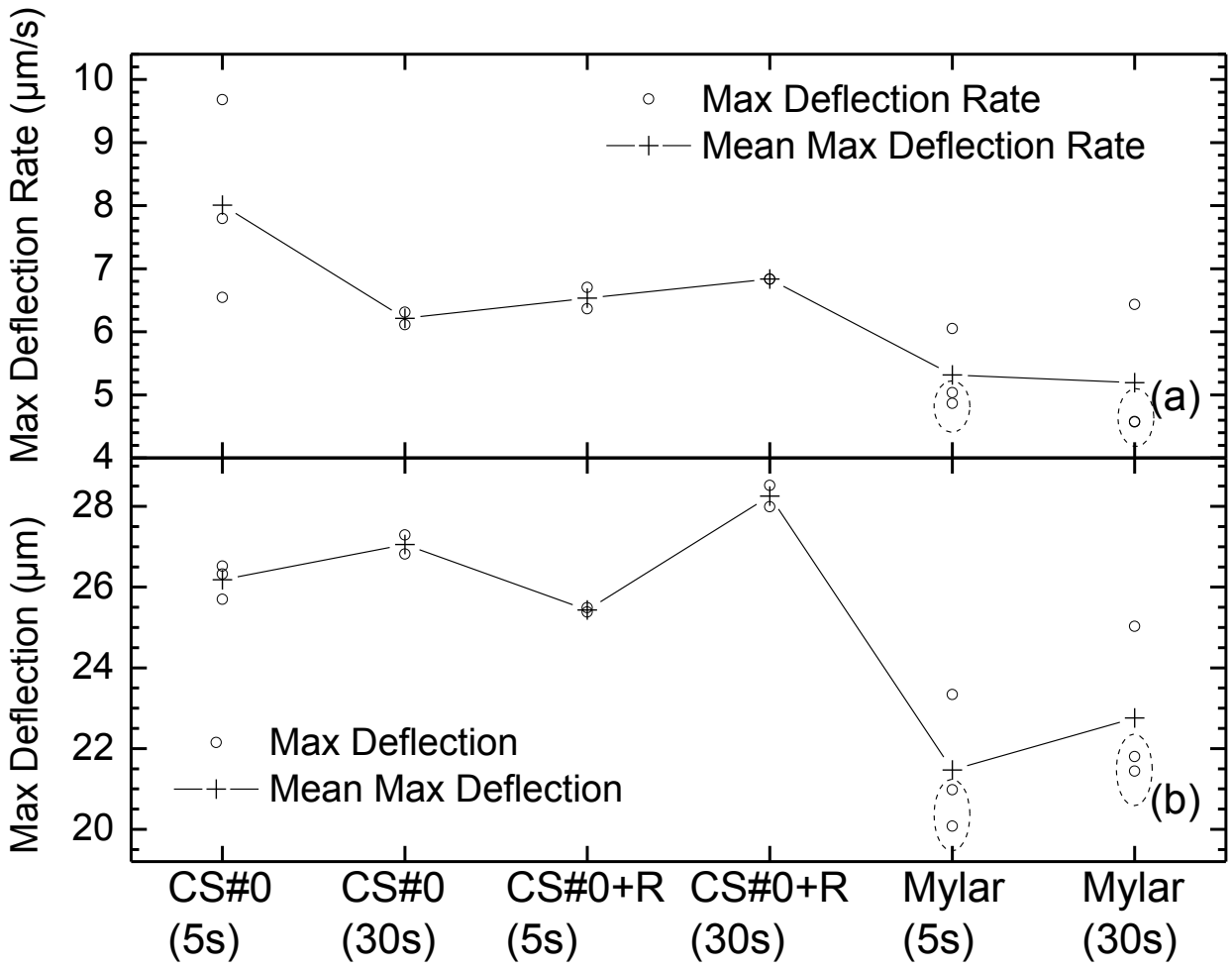

Figure 20 Maximum deflection rate (a) and deflection (b) at the center of the sample for each of the sample geometries and experimental conditions. The RBC samples are made with the Filtek™ Supreme Ultra CT. The LCU used is Sapphire® using a standard light guide on the bleach mode setting. The open circles and crosses correspond to the measured maximum deflection and maximum deflection rate and their mean values, respectively. The x-axis labels describe the sample experimental conditions: CS#0 – 100 μm thick glass coverslip, CS#0+R – 100 μm thick glass coverslip with a brass ring, Mylar – 25 μm thick Mylar coverslip (without brass ring). The 5s and 30s within the parenthesis means 5 s and 30 s light exposure, respectively. The maximum deflection was measured at 90 s after the LCU was turned on. Note that for the two data points (enclosed by a dashed circle) below the mean value for both Mylar (5s) and Mylar (30s) the sample conditions differed in that, rather than the standard RBC sample thickness of 1.22 mm, 1.00 mm thick samples were used. The lines are a guide to the eye to highlight the similarities and differences in kinetics between the sample geometries. Note that CS#0 (30s), CS#0+R (5s), and CS#0+R (30s) all have only 2 repeats.

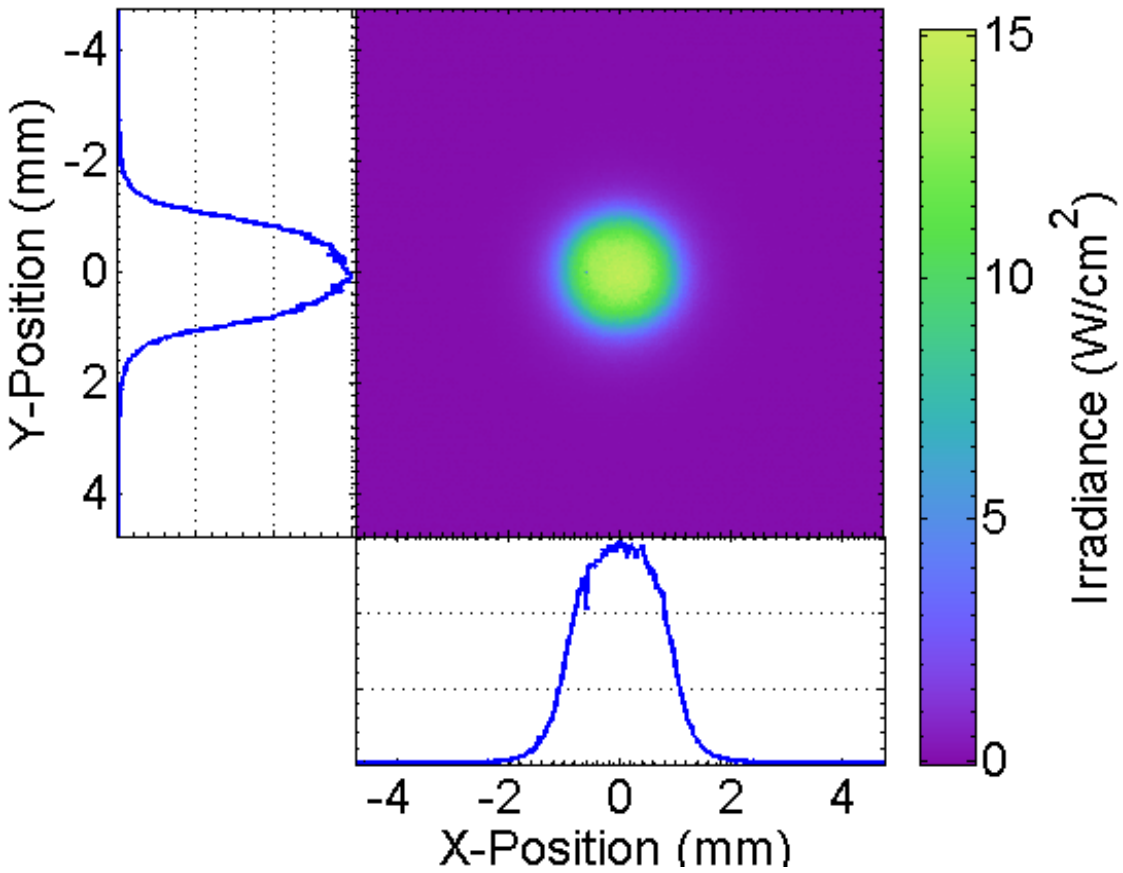

Figure 21 Irradiance beam profile of the Sapphire® LCU with a turbo light guide on the bleach mode setting. Total power output was 510 mW and the beam profile full width at half maximum was 2.0 mm. The blue-colored y- and x- line scans (left-side and bottom plots) are profiles through the center of the 2D profile. The line scan and colorbar irradiance maximum and minimum value is 15.1 W/cm² and 0 W/cm², respectively.

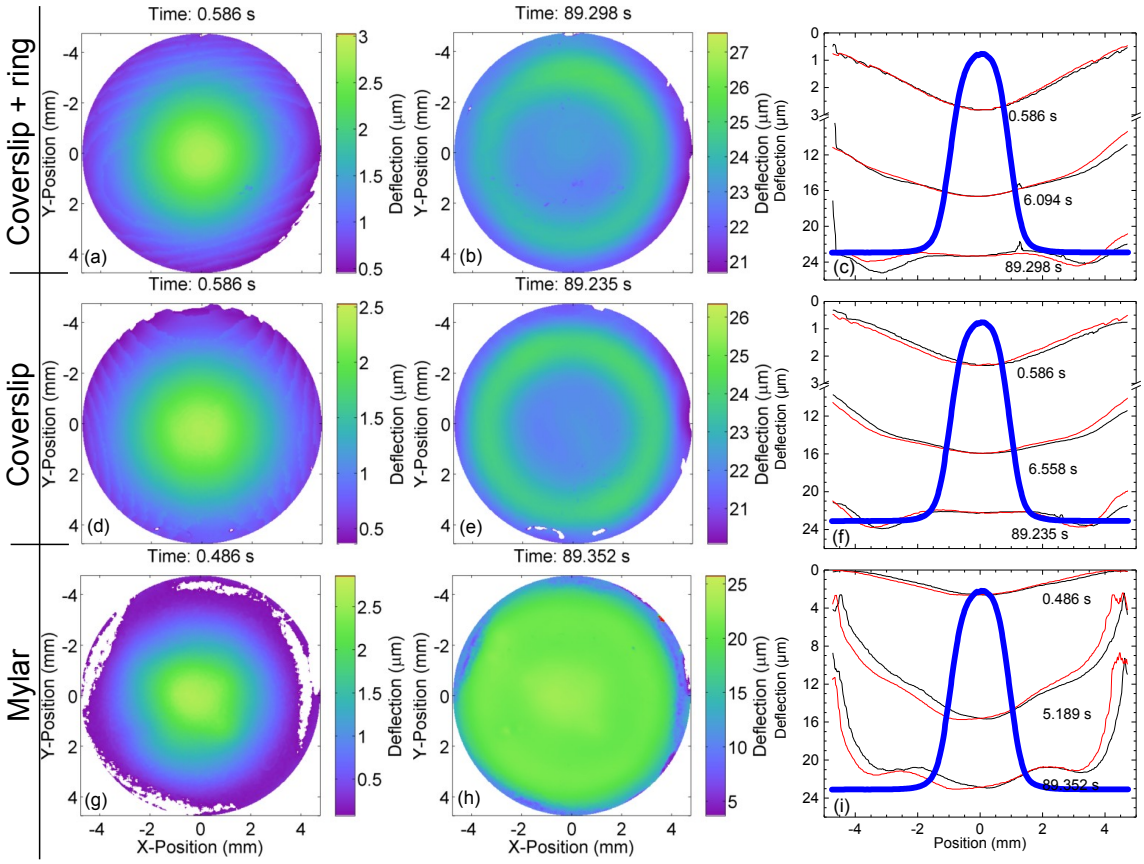

Figure 22 Surface topography of RBC samples made with Filtek™ Supreme Ultra CT cured by a Sapphire® LCU using a turbo light guide on bleach mode for 30 seconds. The sample temperature was 22 °C. The sample geometries used were 100 µm thick glass coverslip with a brass ring (a-c), 100 µm thick glass coverslip without a brass ring (d-f), and 25 µm thick Mylar coverslip without a brass ring (g-i). The surface topographies where the sample shrinkage rate at the center was at a maximum (a,d,g) and at the end of acquisition (b,e,h) are displayed. Horizontal (red line) and vertical (black line) line profiles (c,f,i) passing through the center of the sample shrinkage map are shown. Note the broken vertical axis for figures (c) and (f). The data collection time for each of the line profile is given next to the line. The white areas in the 2D maps indicate the absence of data or data below the minimum value in the color scale. The semi-transparent blue line (c,f,i) is the x-line scan through the center of the LCU 2D beam profile.

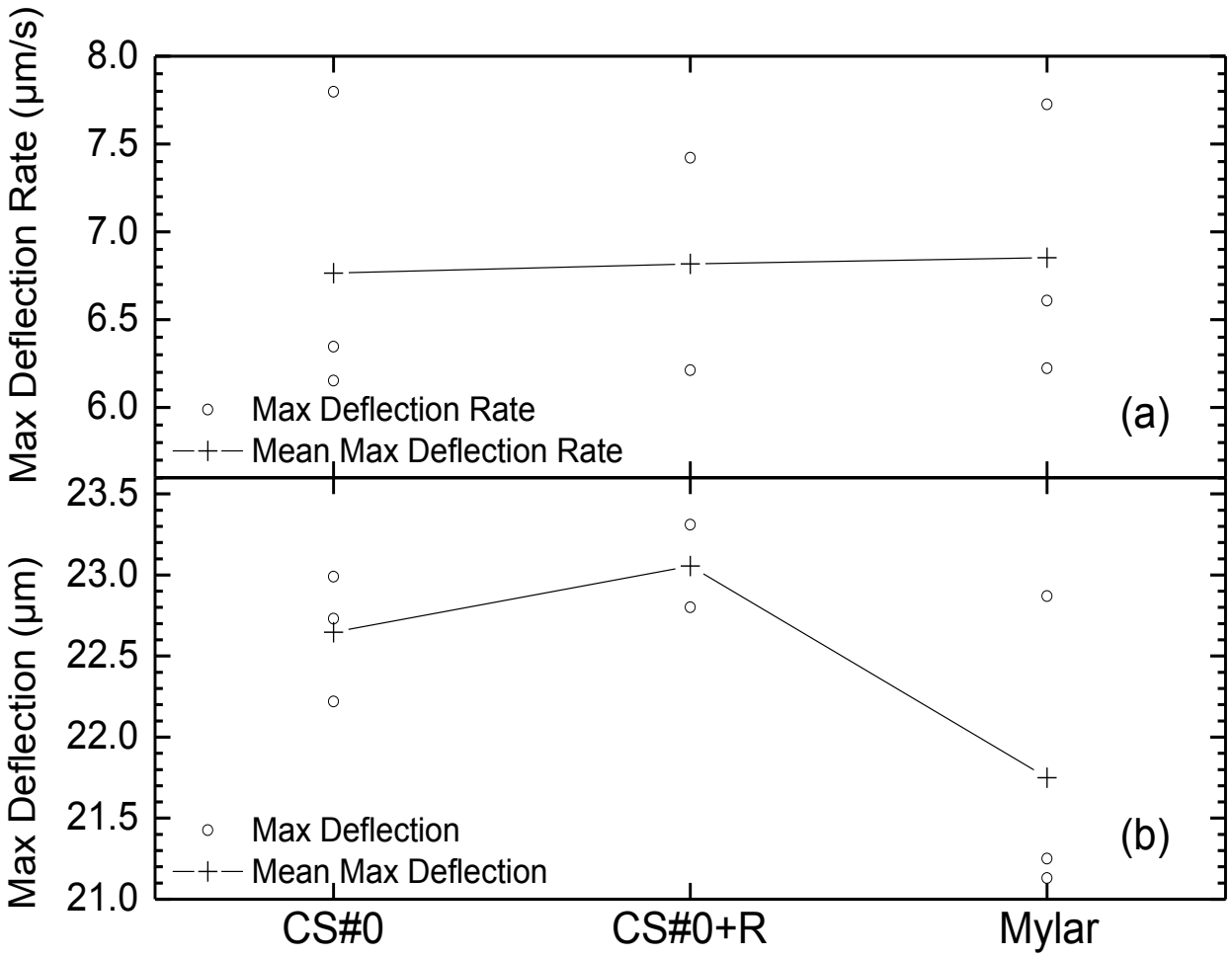

Figure 23 Maximum deflection rate (a) and deflection (b) at the center of the sample for each of the sample geometries and experimental conditions. The RBC sample is made with Filtek™ Supreme Ultra CT. The LCU used is Sapphire® using a turbo light guide on the bleach mode setting for 30 s. The sample temperature was 22 °C. The open circles and crosses correspond to the measured and mean values, respectively. The x-axis labels describe the experimental conditions as follows: CS#0 – 100 μm thick glass coverslip without a brass ring, CS#0+R – 100 μm thick glass coverslip with a brass ring, Mylar – 25 μm thick Mylar coverslip without brass ring. The maximum deflection was measured at 90 s after the LCU was turned on. The lines are a guide to the eye to highlight the similarities and differences in kinetics between the sample geometries. Note that CS#0+R has only 2 repeats.

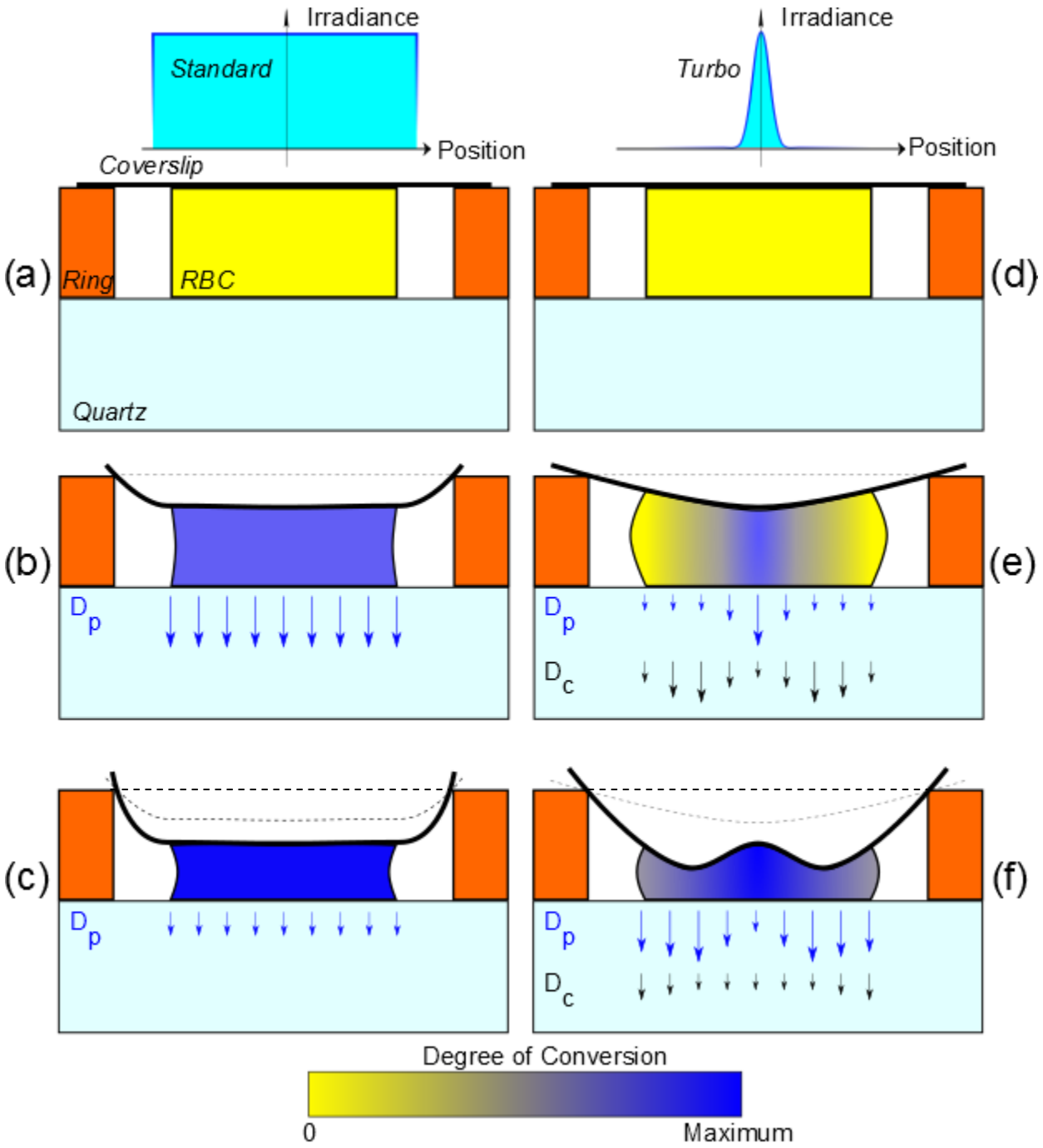

Figure 24 Schematic diagram depicting the effects of the rigid coverslip induced deformation on the resin-based composite (RBC) sample in the bonded disc geometry. Two light curing unit (LCU) beam profiles are considered – uniform as radiated from a standard light guide (a-c) and Gaussian-like distribution with the highest irradiance at the RBC's center as emitted by a turbo light guide (d-f). (a,d) Before light exposure the RBC sample and coverslip are flat. (b) A short time after uniform light exposure the sample shrinkage is uniform across its top surface and the coverslip remains flat. (c) A long time after light exposure the sample shrinkage has further increased but is still uniform across

the top surface due to uniform illumination. The coverslip remains flat and no coverslip induced sample deformation occurred during photopolymerization. Also displayed for case (b) and (c) is the radial photopolymerization shrinkage near the sample midsection. (e) A short time after light exposure photopolymerization and shrinkage is localized near the sample center. The sample pulls on the coverslip near its center taking on a concave shape and resulting in the RBC still in the liquid or gel state to a brief flow outward. The momentary RBC radial outflow results in a convex shape for the outer sample edge where no flow at the sample/substrate and sample/coverslip interface is assumed. (f) As photopolymerization progressed at long time the central part of the sample where the irradiance is highest is the first part of the sample to complete its shrinkage. Then the outer sample region where outward RBC flow occurred continues to shrink relative to the sample center. As a result, after light exposure the coverslip forms a smooth "w" shape. D_p (blue arrows) and D_c (black arrows) is the deflection of the RBC due to photopolymerization induced shrinkage and coverslip induced deformation, respectively. The length of the arrows indicates the magnitude of the deflection. The dashed gray line indicates the position of the coverslip in the previous instance. The colorbar at the bottom of the figure maps the RBC's degree of conversion of zero to maximum from yellow to blue, respectively. Note that the dimensions are not to scale.

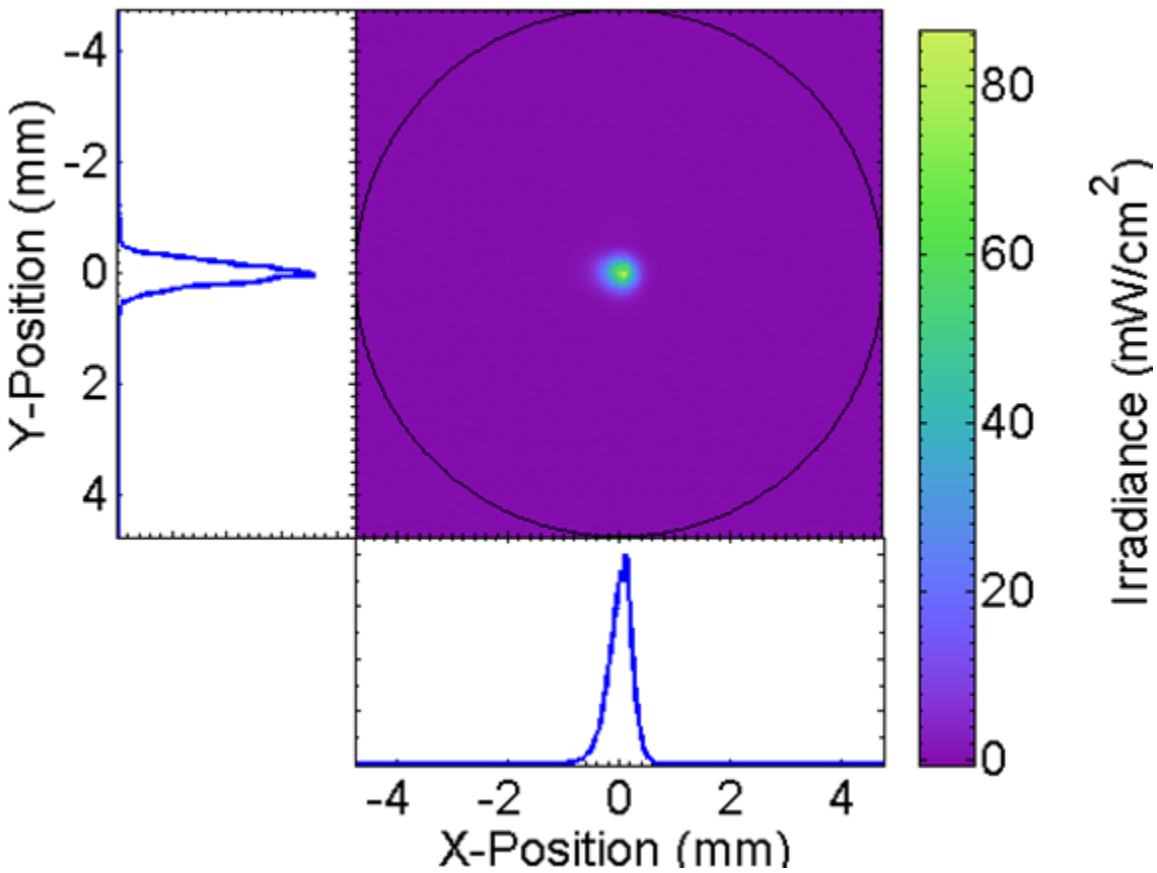

Figure 25 Irradiance beam profile of the Sapphire® LCU with a standard light guide and a 250 µm diameter aperture attachment placed on the light guide tip. Total power output was 201 µW and the beam profile full width at half maximum was 0.5 mm. The blue-colored y- and x- line scans (left-side and bottom plots) are profiles through the center of the 2D profile. The line scan and colorbar irradiance maximum and minimum value is 86.1 mW/cm² and 0 mW/cm², respectively.

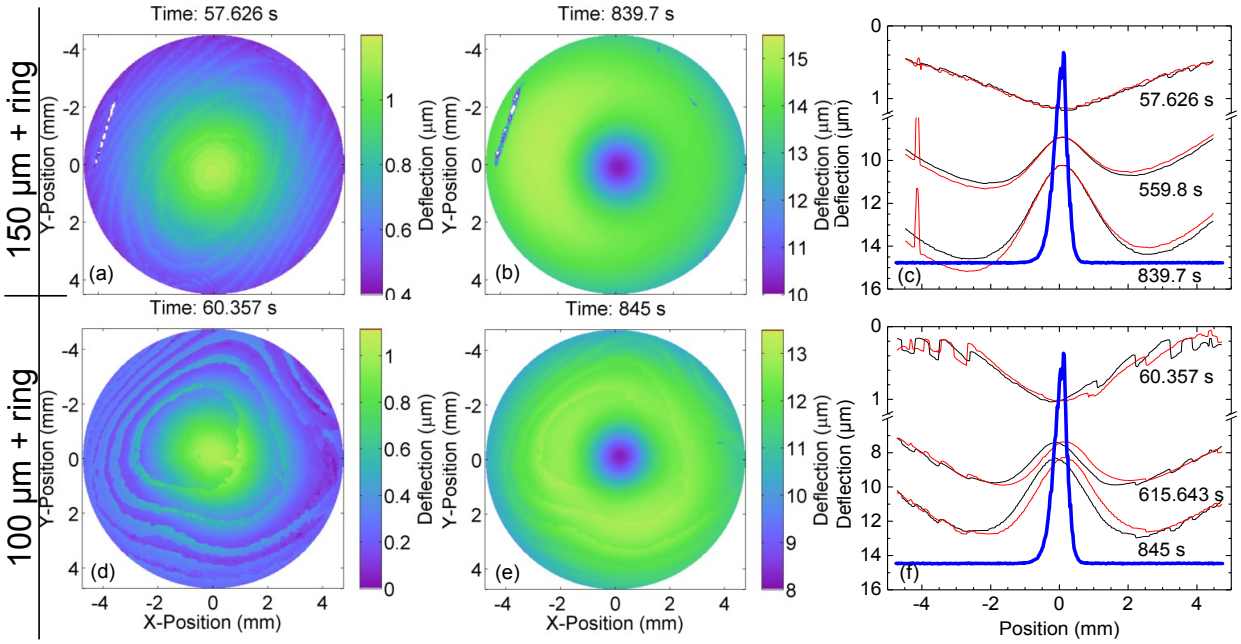

Figure 26 Surface topography of RBC samples made with Filtek™ Supreme Ultra CT cured by a Sapphire® LCU using a standard light guide with 250 µm diameter aperture attachment set on bleach mode for 30 seconds. The sample temperature was 22 °C. The two sample geometries used were 150 µm thick glass coverslip with a brass ring labeled "150 µm + ring" (a-c) and 100 µm thick glass coverslip with a brass ring labeled "100 µm + ring" (d-f). The surface topographies where the sample shrinkage rate at the center was at a maximum (a,d) and at the end of acquisition (b,e) are shown. Horizontal (red line) and vertical (black line) line profiles (c,f) passing through the center of the sample shrinkage map are shown. Note the vertical broken axis. The data collection time for each of the line profile is given next to the line. The white areas in the 2D maps indicate the absence of data or data below the minimum value in the color scale. The semi-transparent blue line (c,f) is the x-line scan through the center of the LCU 2D beam profile. The spikes seen at -4 mm position for figure (c) are reconstruction errors which are also seen in figures (a) and (b) as a white line starting from -4 mm and ending at -3 mm x-position.

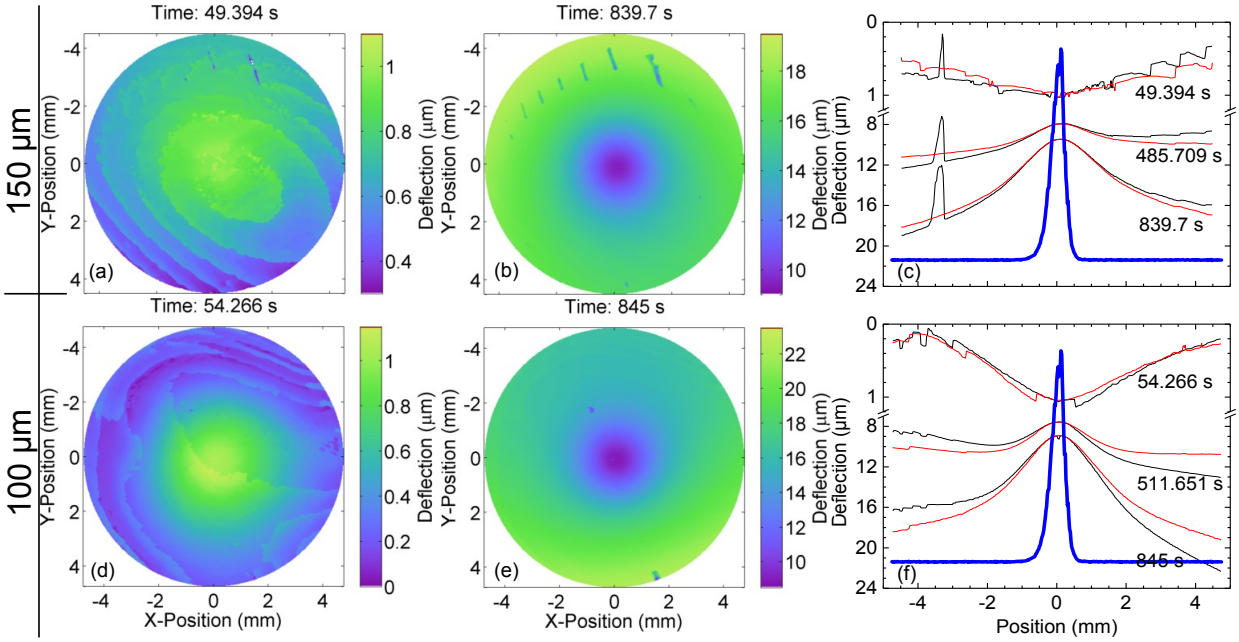

Figure 27 Surface topography of RBC samples made with Filtek™ Supreme Ultra CT cured by a Sapphire® LCU using a standard light guide with a 250 µm diameter aperture attachment placed on the light guide tip set on bleach mode for 30 seconds. The sample temperature was 22 °C. The two sample geometries used were 150 µm thick glass coverslip without a brass ring labeled "150 µm" (a-c) and 100 µm thick glass coverslip without a brass ring labeled "100 µm" (d-f). The surface topographies where the sample shrinkage rate at the center was at a maximum (a,d) and at the end of acquisition (b,e) are shown. Horizontal (red line) and vertical (black line) line profiles (c,f) passing through the center of the sample shrinkage map are shown. Note the vertical broken axis. The data collection time for each of the line profile is given next to the line. The white areas in the 2D maps indicate the absence of data or data below the minimum value in the color scale. The spikes at -3.5 mm at all times in (c) are reconstruction errors. The semi-transparent blue line (c,f) is the x-line scan through the center of the LCU 2D beam profile.

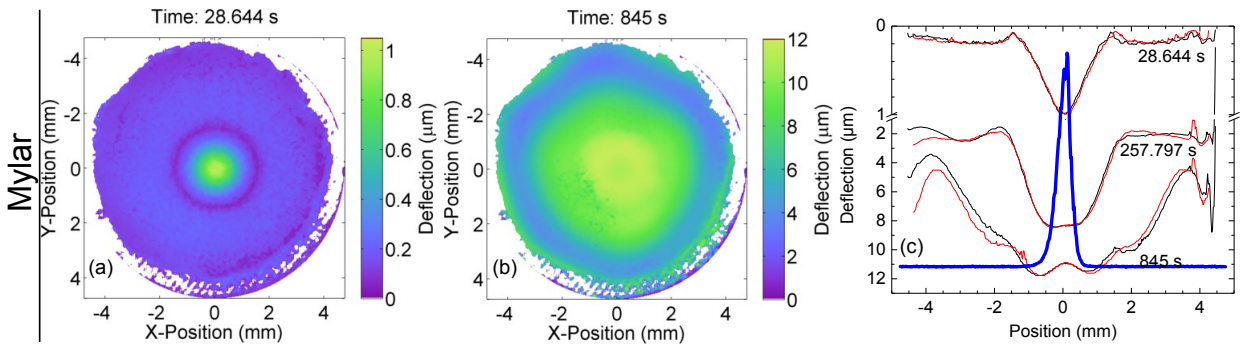

Figure 28 Surface topography of a RBC sample made with Filtek™ Supreme Ultra CT cured by a Sapphire® LCU using a standard light guide with 250 µm diameter aperture attachment set on bleach mode for 30 seconds. The sample temperature was 22 °C. The sample geometry used was 25 µm thick Mylar coverslip without a brass ring (a-c). The surface topography where the sample shrinkage rate at the center was at a maximum (a) and at the end of acquisition (b) is shown. Horizontal (red line) and vertical (black line) line profiles (c) passing through the center of the sample shrinkage map are shown. Note the vertical broken axis. The data collection time for each of the line profile is given next to the line. The white areas in the 2D maps indicate the absence of data or data below the minimum value in the color scale. The semi-transparent blue line (c) is the x-line scan through the center of the LCU 2D beam profile.

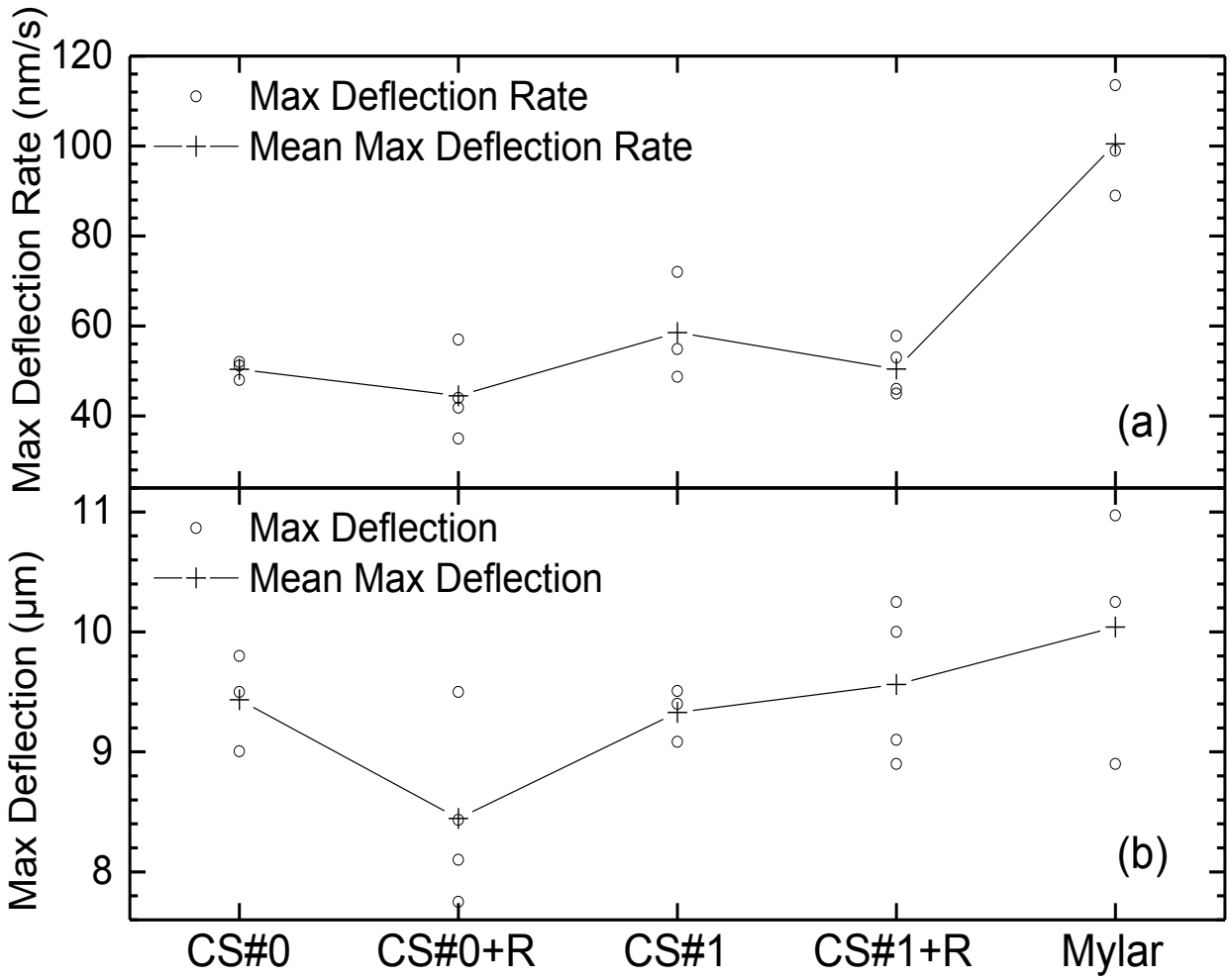

Figure 29 Maximum deflection rate (a) and deflection (b) at the center of the sample for each of the sample geometries and experimental conditions. The RBC samples were made with Filtek™ Supreme Ultra CT. The LCU used was a Sapphire® using a standard light guide with 250 µm diameter aperture attachment set on the bleach mode setting for 30 s. The sample temperature was 22 °C. The open circles and crosses correspond to the measured and mean values, respectively. The x-axis labels describe the experimental conditions as follows: CS#0 – 100 µm thick glass coverslip without a brass ring, CS#0+R – 100 µm thick glass coverslip with a brass ring, CS#1 – 150 µm thick glass coverslip without a brass ring, CS#1+R – 150 µm thick glass coverslip with a brass ring, Mylar – 25 µm thick Mylar coverslip without brass ring. The maximum deflection was measured at 845 s after the LCU was turned on. The lines are a guide to the eye to highlight the similarities and differences in kinetics between the sample geometries. Note that CS#0+R and CS#1+R have 4 repeats.

Chapter 4
EFFECT OF A LED-BASED LCU IRRADIANCE BEAM PROFILE ON THE SAMPLE TOPOGRAPHY DURING AND AFTER LIGHT EXPOSURE

4.1 INTRODUCTION

RBC polymerization shrinkage is a function of the LCU irradiance such that the greater LCU irradiance the faster the rate of photoinitiation. Thus a non-uniform irradiance beam profile will generate a non-uniform polymerization shrinkage rate throughout the sample. The Bluephase Style LCU has been selected for this study because it has a non-uniform irradiance beam profile at distances of 0 mm to 3 mm from the light emitting tip. The LCU consists of 3 LEDs where two of these LEDs emit at a peak wavelength of 470 nm (blue) and a third LED at 410 nm (violet). This allows curing of RBCs that contain photoinitiators such as camphorquinone (CQ) and monoacylphosphine oxide (Lucirin® TPO) whose peak sensitivities in the absorption spectrum are different. CQ has peak sensitivity in its absorption spectrum at 470 nm, whereas Lucirin is at 381 nm [83]. Tetric EvoCeram is an example of a RBC that has both photoinitiator types which can be activated by the Bluephase Style LCU. The RBC Filtek™ Supreme Plus A4B contains only CQ. In this chapter, the Bluephase Style is used on RBC samples made with Tetric EvoCeram and Filtek™ Supreme Plus A4B to study the effects of a non-uniform irradiance beam profile on the sample shrinkage topography.

4.2 RESULTS

Irradiance beam profile of the Bluephase Style LCU is shown in Figure 30. The beam profile was acquired at 0 mm distance from the light guide tip. Total power output was 671 mW. The mean irradiance at the center of each of the two blue LEDs and the one violet LED were 5 W/cm² and 2 W/cm², respectively.

A comparison between the Bluephase Style LCU irradiance beam profile and the axial deflection of Filtek™ Supreme Plus A4B and Tetric EvoCeram samples are shown in Figure 31. Both the top and bottom-left spots in the beam profile correspond to the 470 nm (blue) peak wavelength LEDs. The middle-right LED corresponds to the 410 nm (violet) peak wavelength LED. The sample geometry included a 25 μm thick Mylar coverslip and a 3.0 mm or 1.5 mm thick quartz disc substrate both of which were 25.4 mm in diameter. Three distinct deflection spots in the sample shrinkage map corresponding to the regions irradiated by the three LEDs in the LCU are evident. As depicted in Figure 31(c), the shrinkage map of Filtek™ Supreme Plus A4B (CQ only) sample the deflection was predominantly localized to the regions irradiated by the blue LEDs, whereas there was less deflection from the violet LED. Shown in Figure 31(b,d), the Tetric EvoCeram (CQ and Lucirin) sample shrinkage map displays three distinct deflection spots corresponding to the regions irradiated by the three LEDs in the LCU.

The surface topography of the RBC sample made with Filtek™ Supreme Plus A4B and cured by a Bluephase Style LCU for 30 seconds is shown in Figure 32. The sample

geometry included a 25 μm thick Mylar coverslip and a 3.0 mm thick quartz disc substrate both of which were 25.4 mm in diameter. In the shrinkage map where the deflection rate was at a maximum, occurring at 1.251 s, the deflection was predominantly localized to the regions irradiated by the blue LEDs with little deflection from the violet LED. At the end of acquisition, occurring at 88.938 s, the shrinkage map was more uniform than at earlier times.

The surface topography of the RBC sample made with Tetric EvoCeram and cured by a Bluephase Style LCU for 30 seconds is shown in Figure 33. The sample geometry included a 25 μm thick Mylar coverslip and a 3.0 mm thick quartz disc substrate both of which were 25.4 mm in diameter. In the shrinkage map where the deflection rate is at a maximum, occurring at 0.667 s, three distinct deflection spots corresponding to the regions irradiated by the three LEDs in the LCU are observable. At the end of acquisition, occurring at 89.896 s, the shrinkage map had greater uniformity than it did at earlier times obfuscating the three distinct deflection spots.

The surface topography of the RBC sample made with Tetric EvoCeram and cured by a Bluephase Style LCU for 30 seconds is shown in Figure 34. The sample geometry included a 25 μm thick Mylar coverslip and a 1.5 mm thick quartz disc substrate both of which were 25.4 mm in diameter. In the shrinkage map where the deflection rate was at a maximum, occurring at 0.667 s, three distinct deflection spots corresponding to the regions irradiated by the three LEDs in the LCU are evident. At the end of acquisition,

occurring at 89.896 s, the shrinkage map was more uniform than it was at earlier times obfuscating the three distinct deflection spots.

4.3 Discussion

The choice of sample geometry was to ensure that the effect of a commercial LCU that has a non-uniform irradiance beam profile was as evident as possible. The coverslip used was a 25 μm thick Mylar which allowed it to flexibly conform to the shrinking sample to prevent the effect of coverslip induced deformation. The quartz disc substrate was 3.0 mm thick. For one experimental stage it was altered to 1.5 mm to reduce the distance between the LCU light emitting tip and the sample. Reducing the distance maximized the non-uniformity of the LCU beam profile on the sample. As the distance from the LCU increased any irradiance variation is averaged due to the divergence of the emitted light which caused overlapping.

Results from the shrinkage map collected at short times, suggest a strong correlation with the position of the LEDs in the LCU, the LED emission wavelength, and the RBC type. Filtek™ Supreme Plus A4B used the photoinitiator CQ and did not contain the violet light sensitive Lucirin, thus minimal shrinkage was observed in the region corresponding to the violet LED. By comparison Tetric EvoCeram had both photoinitiator types, and significant shrinkage induced by the violet LED was observed. The shrinkage in the regions from the blue LEDs was greater than from the violet LED indicating that the Lucirin photoinitiated polymerization reaction was initially slower than that of CQ. The

rate of reaction depends on the irradiance from the violet LED, concentration of the photoinitiator, as well as its intrinsic reaction rate.

At 90 s after photoinitiation both Filtek™ Supreme Plus A4B and Tetric EvoCeram show nearly uniform axial shrinkage throughout the sample. The uniformity of the shrinkage map obfuscates evidence of having used a non-uniform irradiance beam profile. The LCU irradiated the samples for 30 s which, based on the uniformity of the results, appears sufficient to attain a high degree of curing (DC) throughout the sample. The higher the DC the larger the polymerization induced shrinkage. A uniform DC then corresponds to uniform shrinkage. This demonstrates that a non-uniform irradiance beam profile is mostly apparent near the beginning of photoinitiation when the DC throughout the sample is still non-uniform.

4.4 Summary

There is a strong correlation between the LCU irradiance beam profile, LED emission wavelength, the RBC type, and its axial shrinkage map shortly after irradiation. With increasing time since LCU light exposure the correlation is obfuscated as the shrinkage becomes increasingly uniform throughout the sample.

4.5 Figures and Tables

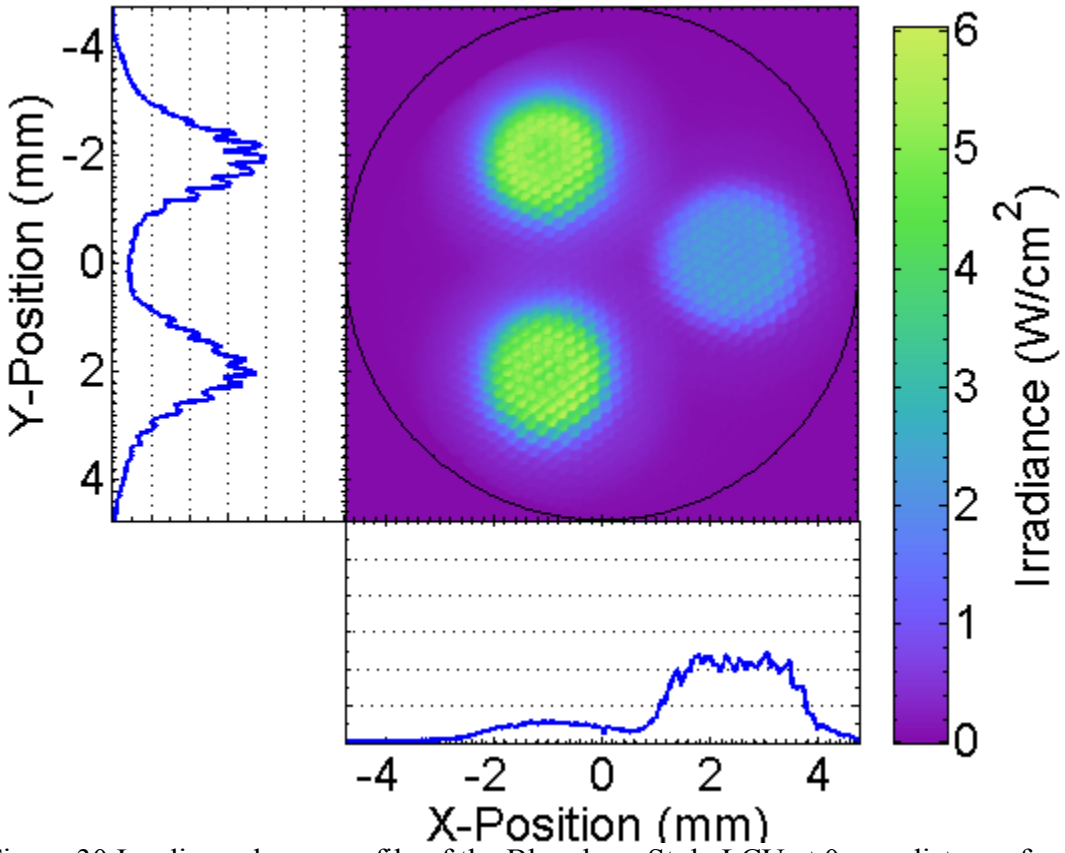

Figure 30 Irradiance beam profile of the Bluephase Style LCU at 0 mm distance from the light guide tip. Total power output was 671 mW. The mean irradiance at the center of the top-left and bottom-left spot and middle-right spot is 5 W/cm² and 2 W/cm², respectively. The top-left and bottom-left spot and middle-right spot correspond to the blue LEDs (470 nm) and the middle-right spot is the violet LED (410 nm). The blue-colored line scans (left-side and bottom plots) are profiles through the center of the 2D beam profile. The line scan and colorbar irradiance axis maximum value is 6 W/cm² with a corresponding minimum value at 0 W/cm².

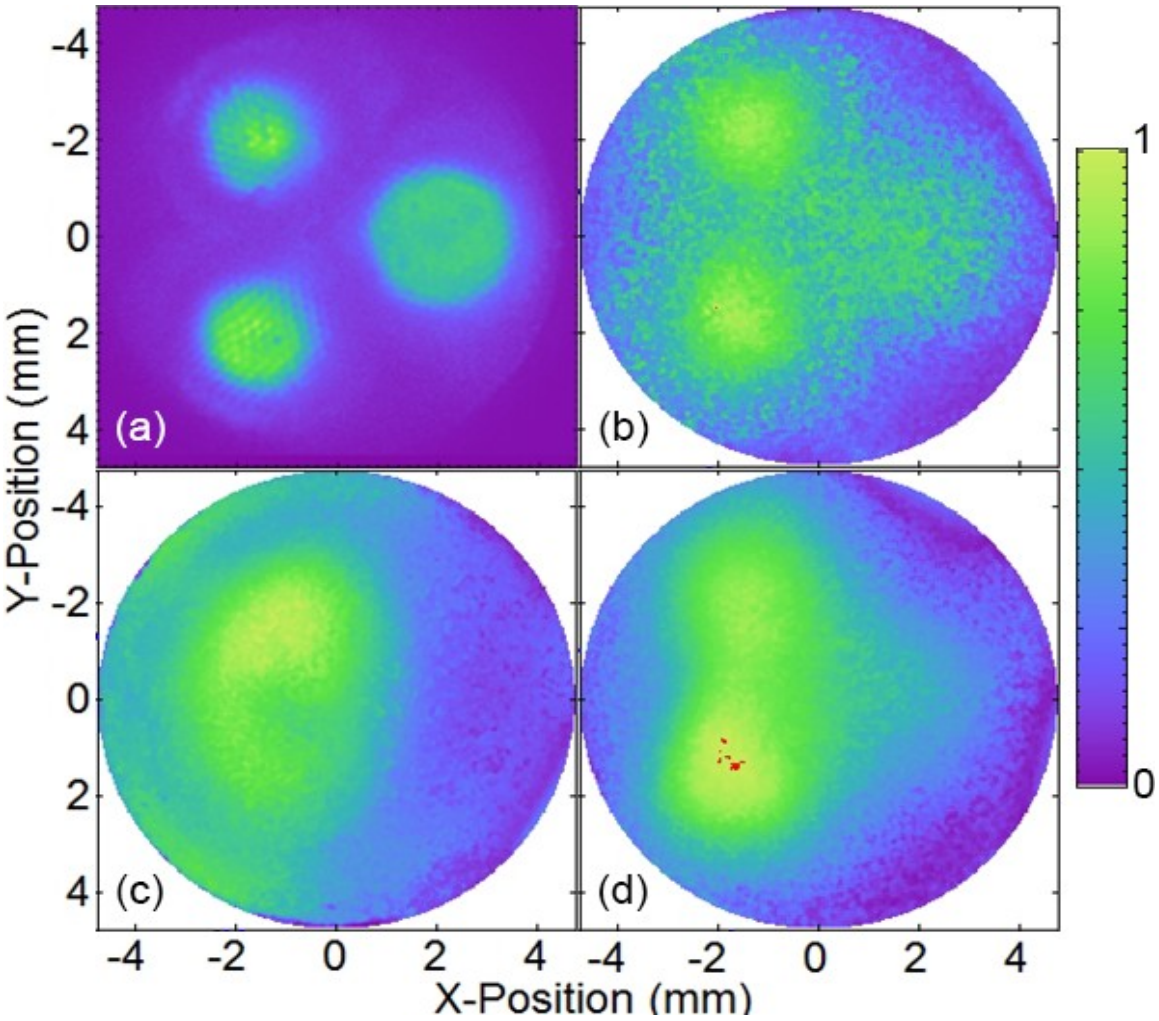

Figure 31 An early stage comparison between the beam profile and the shrinkage map of two different RBCs. (a) Irradiance beam profile of the Bluephase Style LCU as imaged through the Michelson interferometer system using arbitrary irradiance units. The top-left and bottom-left spots in the beam profile correspond to the 470 nm peak wavelength emitting LEDs. The middle-right LED corresponds to the 410 nm peak wavelength emitting LED. (b) Shrinkage map of RBC sample made with Tetric EvoCeram at 0.25 s after light exposure with a 1.5 mm thick quartz disc substrate. (c) Shrinkage map of RBC sample made with Filtek™ Supreme Plus A4B at 0.5 s after light exposure with a 3.0 mm thick quartz disc substrate. (d) Shrinkage map of RBC sample made with Tetric EvoCeram at 0.334 s after light exposure with a 3.0 mm thick quartz disc substrate. The sample geometry was a 25 µm thick Mylar coverslip without a brass ring and quartz disc substrate of 1.5 mm or 3.0 mm thickness. The white and red regions in the 2D maps indicate the absence of data, or data below the minimum value, and data above the maximum value in the color scale, respectively. These are representative results taken from three repeats done for each condition. The colorbar is an arbitrary scale where the

minimum value is zero and the maximum value is 0.2 μm, 0.55 μm, and 0.45 μm for the plots (b), (c), and (d), respectively.

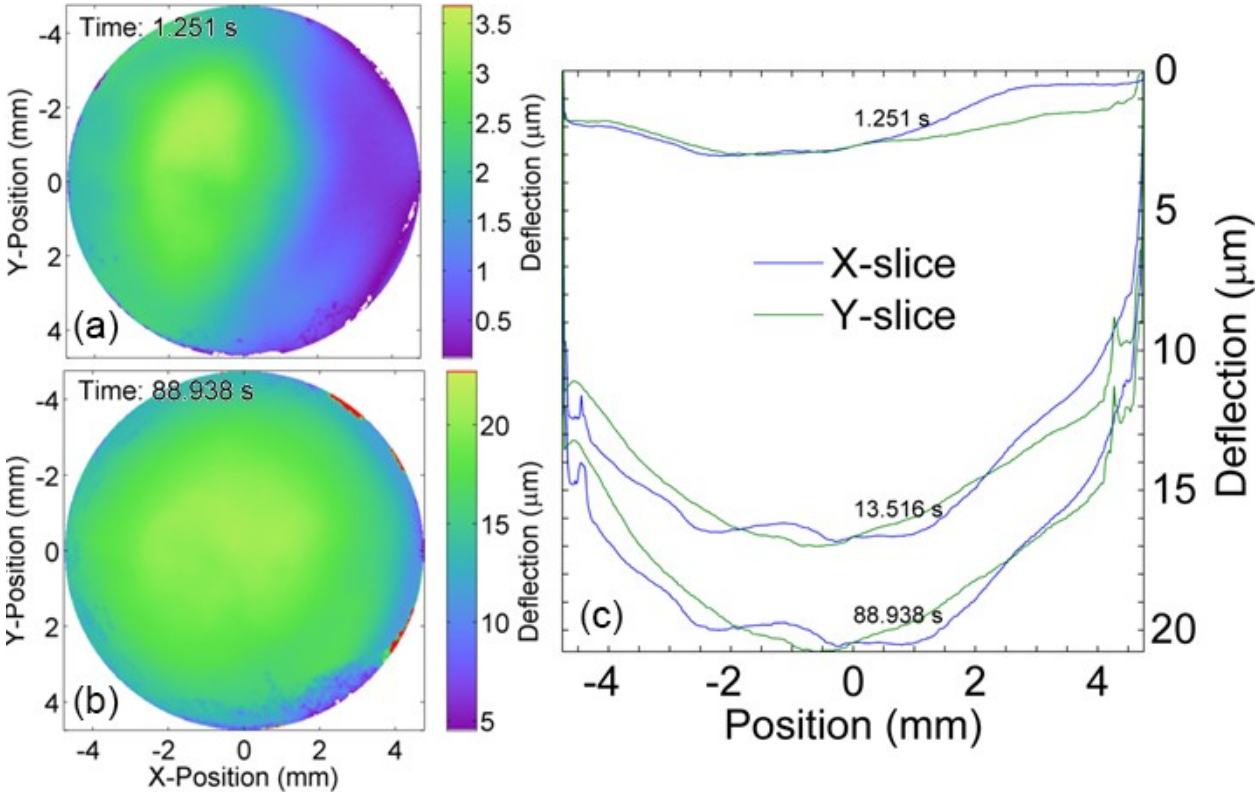

Figure 32 Surface topography of RBC samples made with Filtek™ Supreme Plus A4B cured by a Bluephase Style LCU for 30 seconds. The sample geometry included a 25 µm thick Mylar coverslip without a brass ring and a quartz disc substrate of 3.0 mm thickness. The surface topographies where the sample shrinkage rate at the center was at a maximum (a) and at the end of acquisition (b) are shown. Horizontal (X-slice) and vertical (Y-slice) line profiles (c) passing through the center of the sample shrinkage map are shown. The data collection time for each of the line profiles is displayed by the respective image. The white and red regions in the 2D maps indicate the absence of data, or data below the minimum value, and data above the maximum value in the color scale, respectively. These are representative results taken from the three experiment repeats.

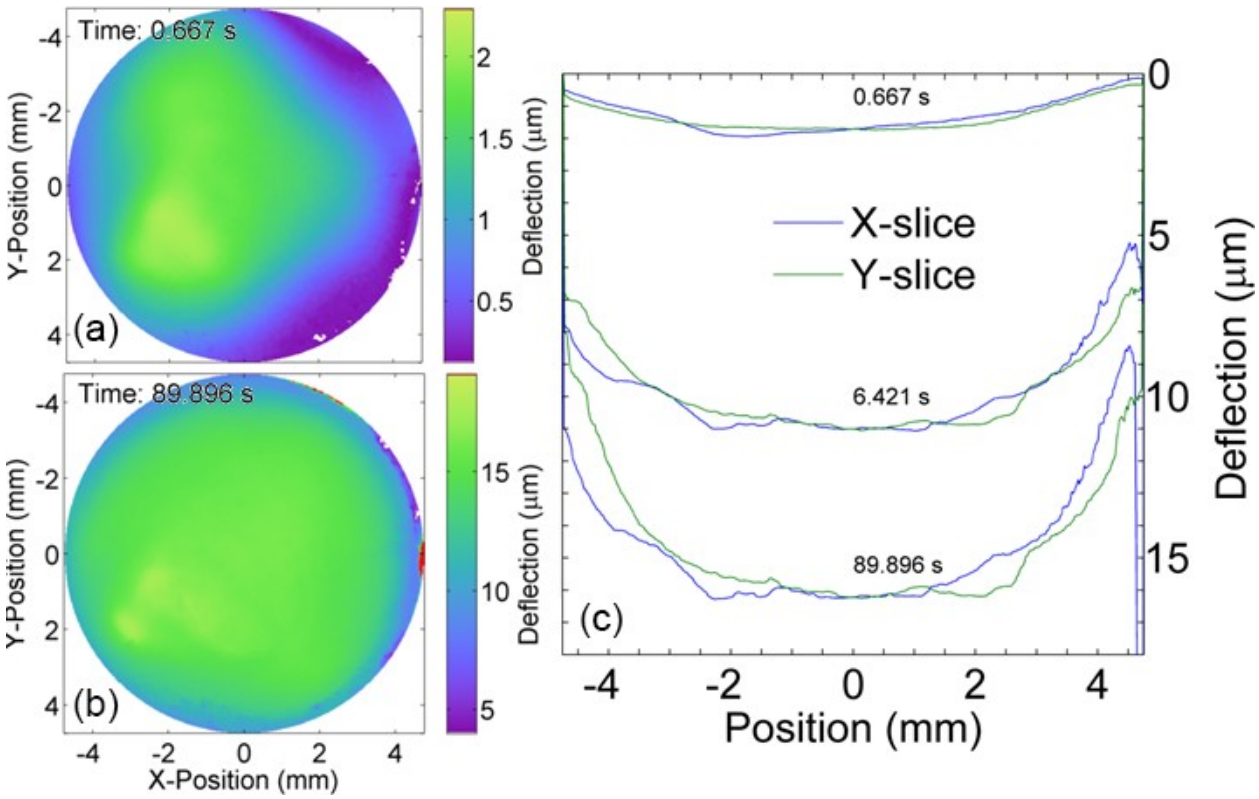

Figure 33 Surface topography of RBC samples made with Tetric EvoCeram and cured by a Bluephase Style LCU for 30 seconds. The sample geometry included a 25 µm thick Mylar coverslip without a brass ring and a quartz disc substrate of 3.0 mm thickness. The surface topographies where the sample shrinkage rate at the center was at a maximum (a) and at the end of acquisition (b) are shown. Horizontal (X-slice) and vertical (Y-slice) line profiles (c) passing through the center of the sample shrinkage map are shown. The data collection time for each of the line profiles is displayed by the respective image. The white and red regions in the 2D maps indicate the absence of data, or data below the minimum value, and data above the maximum value in the color scale, respectively. These results are representatively presented and taken from the three experimental repeats.

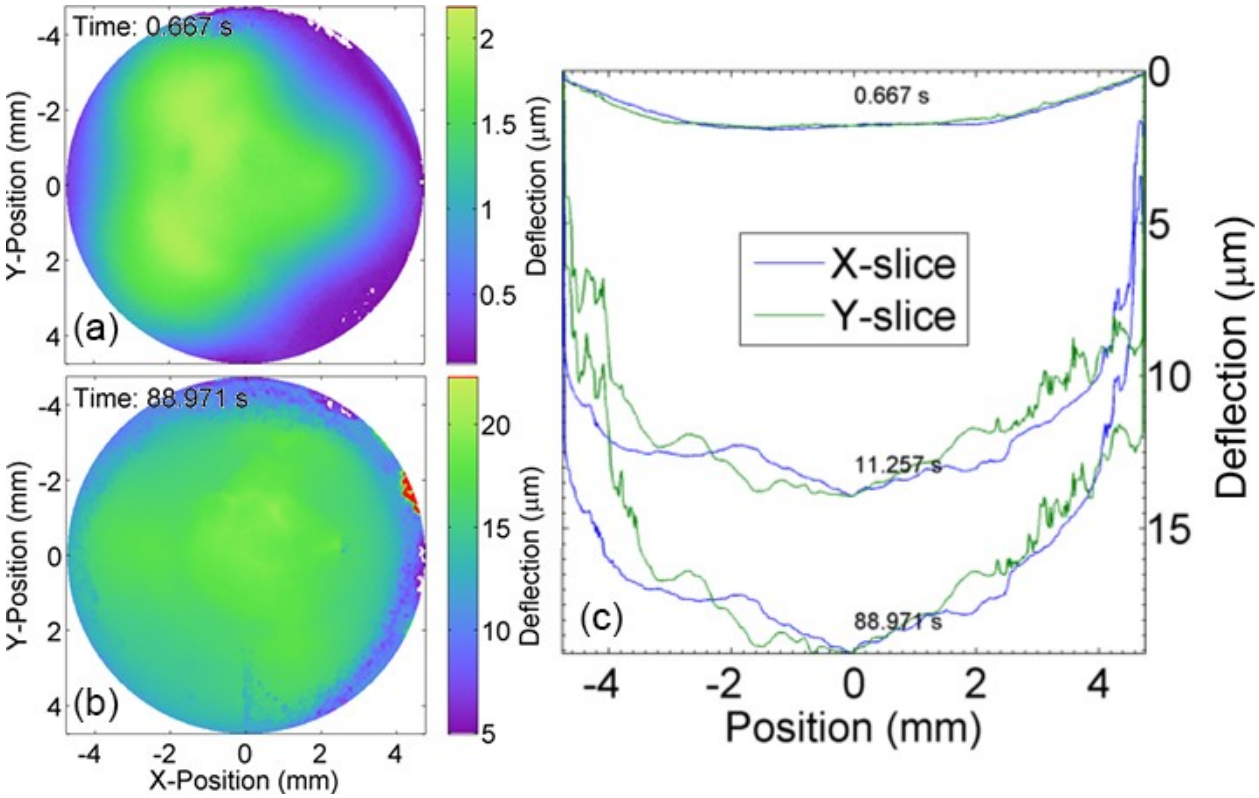

Figure 34 Surface topography of RBC samples made with Tetric EvoCeram and cured by a Bluephase Style LCU for 30 seconds. The sample geometry included a 25 µm thick Mylar coverslip without a brass ring and a quartz disc substrate of 1.5 mm thickness. The surface topographies where the sample shrinkage rate at the center was at a maximum (a) and at the end of acquisition (b) are shown. Horizontal (X-slice) and vertical (Y-slice) line profiles (c) passing through the center of the sample shrinkage map are shown. The data collection time for each of the line profiles is displayed by the image. The white and red regions in the 2D maps indicate the absence of data, or data below the minimum value, and data above the maximum value in the color scale, respectively. These are representative results taken from the three experiment repeats.

Chapter 5
EFFECT OF THE LCU IRRADIANCE BEAM PROFILE ON THE SHRINKAGE KINETICS DURING AND AFTER LIGHT EXPOSURE

5.1 INTRODUCTION

Photoinitiated dimethacrylate RBC polymerization depends on the free radical assisted linkage of monomers [84]. Free radicals are produced in these RBCs by light induced activation of radical-producing molecules, photoinitiators, such as Camphorquinone (CQ). Typically, a tertiary amine is used as a co-initiator with CQ to provide radicals for the polymerization process. CQ has peak absorption sensitivity at 468 nm which is in the perceptually blue part of the electromagnetic spectrum. When CQ is in its activated state one of its two carbonyl groups becomes activated through excitation of its electrons to a higher energy state. In this excited state, if CQ encounters an amine it receives an electron and a Hydrogen cation from the amine thus forming two radicals – a CQ radical and an aminoalkyl radical. The aminoalkyl radical is responsible for initiating polymerization of monomers whereas the CQ radical inhibits the polymerization process [85]. Dimethacrylate monomers such as Bisphenol A-Glycidyl Methacrylate (Bis-GMA) contain two carbon-carbon double bond sites. When it encounters a free radical a bond in one of the sites are broken thus becoming an active site for polymerization where it is ready to form a polymer chain with another active monomer [86].

Generally, free radicals are involved in the initiation, propagation, and termination reactions. These three reactions produce a net change in free radical concentration that is

positive for initiation, zero for propagation, and negative for termination. At the start of polymerization the termination rate is greater as the free radicals collide into themselves. Viscosity increases as polymers are formed. This increase in viscosity then decreases the overall mobility of polymers while leaving monomers relatively mobile. Polymers with free radical ends are then trapped reducing the termination rate making the reaction diffusion limited. The monomers move freely throughout the polymer networks to combine with active polymer chains and undergo propagation reactions. Due to an increase in viscosity the termination rate decreases, and as a result the propagation rate increases resulting in a higher polymerization rate. The rapid increase in the polymerization rate is called *autoacceleration*. As the polymerization progresses, the viscosity increases to the point of significantly reducing the mobility of monomers and making the propagation reaction rate diffusion limited as well. This results in a rapid decrease in the polymerization rate known as *autodeceleration* [2].

The consequence of RBC polymerization is a reduction in bulk volume. This effect is known as polymerization shrinkage. Figure 35 illustrates the effect of polymerization induced volumetric shrinkage. For an unpolymerized RBC the dominant force of interaction between the monomers is the Van der Waals force whereas upon polymerization the monomers form covalent bonds with each other. Given that the strength of interaction for covalent bonds is greater than the Van der Waals interaction the inter-molecular spacing decreases resulting in volumetric shrinkage [25].

5.1.1 Autocatalytic Equation

Initially, Piloyan *et al.* applied the chemical reaction rate equation for the determination of activation energies of chemical reactions by differential thermal analysis [87]. Afterwards, the equation was adapted by Kamal and Sourour to characterize the autocatalytic thermal cure of polyesters [88]. The equation (hereafter referred to as the autocatalytic equation) is:

$$\frac{d\alpha}{dt} = k'\alpha^m(\alpha_m - \alpha)^n \tag{3}$$

where α is the degree of conversion (DC), m and n are the reaction orders, k' is the reaction rate constant, and α_m is the maximum attainable DC. RBC shrinkage is polymerization induced and the autocatalytic equation can be used to model the shrinkage [16]:

$$\frac{d\varepsilon}{dt} = k\varepsilon^m(\varepsilon_m - \varepsilon)^n \tag{4}$$

where ε is the shrinkage strain, m and n are the reaction orders, k is the shrinkage strain rate constant, and ε_m is the maximum attainable shrinkage strain. For the work in this thesis, the autocatalytic equation is expressed in terms of deflection rather than strain:

$$\frac{dD}{dt} = aD^m(b - D)^n \tag{5}$$

where D is the shrinkage deflection, m and n are the reaction orders, a is the shrinkage deflection rate constant, and b is the maximum attainable deflection. This chapter presents the analysis of RBC shrinkage kinetics by non-linear least squares fitting of the autocatalytic function (Equation 5) to the experimental data. The different experimental conditions are then compared by means of the normalized equation. The deflection is

divided by the maximum attainable deflection, and the deflection rates are divided by the maximum deflection rate:

$$\frac{\dot{\delta}}{\dot{\delta}_{max}} = \frac{(m+n)^{m+n}}{m^m n^n}\,\delta^m(1-\delta)^n \qquad (6)$$

where $\delta = D/b$ is the normalized deflection and $\dot{\delta} \equiv \frac{d\delta}{dt}$. Note that Equation 6 depends only on the reaction orders m and n. See Appendix B for the derivation.

Figure 36 demonstrates the trend of Equation 6 for different values of *m* and *n* while keeping *n*, *m*, or the ratio of *n* over *m* constant. The ratio of *n*/*m* is set to 7.5. The deflection value at which the peak deflection rate occurs is given by 1/(*n*/*m*+1) which comes to about 0.12. Increasing *m* or *n* while keeping the ratio of *n*/*m* constant causes the peak to become narrower. The peak position equation states that increasing the reaction order parameter *n* (while keeping *m* constant) makes the deflection value at which the peak deflection rate occurs move closer to zero (δ=0). By increasing the reaction order parameter *m* (while keeping *n* constant), the peak deflection rate position moves closer to the maximum value (δ=1). The more monomers are converted to polymers the larger the deflection. It can then be interpreted that the parameter *m* governs the deflection rate sensitivity to polymer concentration whereas for the parameter *n* it is for monomer concentration.

5.2 Results

Shown in Figure 37 is the deflection rate plotted against the deflection at the sample center for two sample geometries, two LCU light guide types, and two power levels. The

RBC samples were made with Filtek™ Supreme Ultra CT cured by a Sapphire® LCU set on bleach mode for 30 seconds. The two light guide types used were standard and turbo. The two sample geometries used were with a 100 μm thick glass coverslip using a brass ring and a 25 μm thick Mylar coverslip without a brass ring. The sample temperature was 22°C. At high power LCU mode, for any light guide type, the estimated peak deflection rate was in the range of 6-8 μm/s and for low power 1.3-1.6 μm/s.

The deflection rate plotted against the deflection, measured at the center of the sample using a CCD camera as described in Chapter 2, and its corresponding fit using the autocatalytic model for representative samples can be observed in Figure 38. The RBC samples were made with Filtek™ Supreme Ultra CT cured by a Sapphire® LCU set on bleach mode for 30 seconds. Both standard and turbo light guides were used with the LCU set on either high or low power modes. The two sample geometries used were a 100 μm thick glass coverslip with a brass ring and a 25 μm thick Mylar coverslip without a brass ring.

It can be observed that the peak deflection rate's uncertainty increases with increasing deflection rate. The uncertainty at the peak values for the high power conditions was 1 μm/s, as estimated by the peak to peak oscillation range. Using Mylar instead of a glass coverslip achieved a smaller total deflection at the end of acquisition. When the LCU turns off at high power mode the deflection rate temporarily increases, whereas at low power mode the deflection rate rapidly decreases.

Comparison of the normalized autocatalytic model fits to the deflection rate versus deflection at the sample center for different geometries are observed in Figure 39 and Figure 40. The RBC samples were made with Filtek™ Supreme Ultra CT cured by a Sapphire® LCU set on bleach mode for 30 seconds. Both standard and turbo light guides were used with the LCU on a high or low power mode. The two sample geometries used included a 100 μm thick glass coverslip with a brass ring and a 25 μm thick Mylar coverslip without a brass ring. For all cases, except for Mylar coverslip with a turbo light guide, there is a qualitatively significant difference between high and low power modes. However, when comparing between coverslip types the difference is qualitatively smaller. It can be observed when using normal or turbo light guides that the variation of the repeated experiment is greater for high power versus low power modes.

The parameters derived from the autocatalytic model least square fit to the deflection rate versus deflection for different sample conditions are shown in Table 2. Going from high to low LCU power a global trend emerges where the autocatalytic model parameters *m*, *n*, and *b* all increase while *a* decreases. There is a notable exception to this trend however. For the case of a turbo light guide with a glass coverslip the parameters *n* and *b* decrease.

DC and deflection as a function of time of Filtek™ Supreme Ultra CT cured by a Sapphire® LCU set on bleach mode for 30 seconds are shown in Figure 41 and the DC rate and deflection rate are displayed in Figure 42. A standard (876 mW) and attenuated (68 mW) LCU output power mode was used. The deflection and DC was measured at the sample center and on separate samples. The DC data is an average over three repeated

experiments. The rates are calculated taking the finite difference. DC was measured using a FTIR where a 1.22 mm thick RBC disc shaped sample was placed on the 2x2 mm² size sensor. The LCU was then irradiated through a 3 mm thick quartz disc to duplicate the illumination conditions used in the deflection experiments. The deflection measurements were obtained using a 25 μm thick Mylar coverslip. LCU activation timing was unknown for the DC data, so the origin of time was shifted until the sum of squares in the linear regression of deflection versus DC was minimized as shown in Figure 43. For either high or low LCU power cases there was an initial positive residual up to 0.5 μm between 0 % and 3 % DC.

Autocatalytic model fits to the degree of conversion (DC) measurements are shown in Figure 44. The RBC samples were made with Filtek™ Supreme Ultra CT cured by a Sapphire® LCU set on bleach mode for 30 seconds and a standard light guide. The sample temperature was 22°C. A standard (876 mW) and attenuated (68 mW) LCU output power mode was used. DC was measured at the sample center. The fitted parameters for 68 mW are: a=1±1, b=0.49±0.07, m=0.5±0.1, and n=3±1. The fitted parameters for 876 mW are: a=6±1, b=0.70±0.05, m=0.61±0.05, and n=5.0±0.7.

Comparison of the autocatalytic model fits for the DC and deflection measurements are shown in Figure 45. The deflection and DC were measured at the sample center and on separate samples. The RBC samples used were made with Filtek™ Supreme Ultra CT cured by a Sapphire® LCU set on bleach mode for 30 seconds. A standard (876 mW) and attenuated (68 mW) LCU output power mode were used. By decreasing the LCU power

the reaction order *n* decreased for DC and increased for deflection. It was also observed that the reaction order *m* had a larger change for DC than for deflection.

5.3 Discussion

The peak deflection rate correlates better with the quoted LCU power value than with the quoted irradiance value when comparing between the standard and turbo light guide results. The quoted irradiance value for a particular configuration is calculated as the total power over a 1 mm² area about the sample's center and divided by that area. The LCU power value is essentially the irradiance integrated over the 10 mm diameter area of the sample. This indicates that the quoted irradiance value would correlate better if it was calculated by integrating the power over a larger area. If the integration area is increased the irradiance value will decrease for the turbo light guide and due to the higher beam homogeneity stay approximately the same for the normal light guide. The results suggest that the RBC deflection rate is sensitive to beam profile variations further than 1 mm radius away from the sample's center.

It can be observed that is an oscillatory trend in the data at high deflection rates. These oscillations are a result of the CCD camera's limited sampling rate. When using the peak detection algorithm the interference oscillation extrema positions are recorded only in integer multiples of the sampling time interval (8.2 ms for the camera's 122 Hz frame rate). When the interference oscillation frequency is near the Nyquist frequency of the acquisition system, the sample deflection rate is very high. For example, if the interval between two adjacent extrema is 12.3 ms (1.5*sampling time interval) the algorithm will

find that there is either 8.2 ms or 16.4 ms time interval because there are either 2 or 3 data points comprising the interval. Since it is assumed that every half period corresponds to a 158 nm deflection, the calculated deflection rates would then be 19.3 μm/s or 9.63 μm/s. However, the actual deflection rate is 12.8 μm/s. A simulation of the sampling rate dependence of the deflection rate uncertainty is shown in Figure 46. The reconstructed data (blue lines) was derived using the MATLAB peak locating algorithm on the simulated interference pattern sampled at 122 Hz and 1000 Hz. In turn, the interference pattern was calculated using the deflection as a function of time obtained by solving Equation (3), the autocatalytic equation. A sampling rate of 122 Hz and 1000 Hz were chosen to correspond to the camera and photodiode sampling rates, respectively. The error bounds are calculated by allowing only for integer multiples of the sampling interval. The upper and lower bounds are from the rounded down and up interval, respectively. It can be seen that the error increases with increasing deflection rate due to the shorter time interval between successive data points. For 122 Hz the peak error bound range is 3.2 μm/s whereas for 1000 Hz its 0.4 μm/s – a reduction by a factor of 8. Note the comparison between experimental data collected using the camera and photodiode in panel (c) where the camera data has a much higher variation for the deflection rate around the peak value than that for the photodiode data. These results are in agreement with the theoretical analysis.

To improve the time resolution of the interference oscillation frequency, the peak determining algorithm was applied to all the 2401 pixels (sample resolution of 20.6 x 20.6 μm²/pixel) of the camera that constituted a 1 mm² area at the center of the sample.

The aggregated result of the peak determining algorithm is shown in Figure 47. Only the pixels which contain the same number of oscillations by the end of acquisition are chosen. The number of pixels selected for further analysis varied from sample to sample. It was approximately 38 % - 51 % of the total number of pixels. The number of oscillations expected is determined by the median value of the total number of oscillations found by the final time within the sampling region. For a given extremum in the sequence, known as the fringe number, the times at which it is located depends on the initial phase of the interference pattern. Within the sampling area the initial phase will vary some and thus there will be a spread of time values for a given fringe number. Taking the average of the spread of time values will determine a more precise time interval between extrema and thus increase the deflection rate accuracy.

The deflection rate versus deflection has greater variation at high LCU power across the three repeated tests as compared to low LCU power. This is likely due to the large LCU power variation during the first 2.5 seconds of the experiment. Overlay of the RBC shrinkage kinetics and the corresponding LCU output power for two representative samples is shown in Figure 48. For the high power mode the LCU power fluctuation extends past the sample's maximum deflection rate where it attains 45% of the total deflection. For low LCU power tests the power fluctuation ends at 5% of the total deflection. This occurs before the sample reaches its maximum deflection rate. The power fluctuates for a smaller portion of the sample's total shrinkage at low power mode than it does at high power mode. This helps explain why the variation in the repeated experimental tests is lower at low power mode. It is interesting to note at high power

mode the qualitative correlation between the peak in power and a small bump-like shape (emphasized by the gap created between the data points and the green line) in the deflection rate at 10 μm deflection. Likewise, at low power mode there's a qualitative correlation between the initial spike in power and a sudden increase in deflection rate at 0.07 μm.

One noticeable effect of using low instead of high power mode is that when the LCU turns off the deflection rate decreases. At high LCU power mode the sample temperature increases appreciably from absorbing the light. When the LCU turns off the sample temperature decreases sharply thus resulting in the sample's sudden thermal contraction. The sudden thermal contraction is detected as an increased deflection rate. At low power mode the thermal power on the sample from the LCU irradiation is too low to appreciably increase the sample temperature. When the LCU turns off the thermal contraction is negligible, but the deflection rate decreases because the monomer and photoinitiator concentrations are significant enough to have their conversion rates reduced by the absence of the LCU light.

The deflection rate versus deflection plots is qualitatively different when comparing across LCU power levels. However, the difference is minor when comparing across coverslip types. This means that the shrinkage kinetics at the sample's center is largely affected by the LCU optical power and beam profile, but much less by the coverslip used. The coverslip type does not affect the shrinkage behavior at the sample center since that is the region that undergoes the fastest polymerization.

The fastest curing region affects the slower curing areas by coverslip induced deformation as demonstrated and discussed in Chapter 3. As shown in Table 2 the effect of decreasing the LCU power is that the autocatalytic model parameters *m*, *n*, and *b* increase while *a* decreases. The exception to this trend is that for the case of a turbo light guide with a glass coverslip, the parameter *b* decreases. This observed trend may be due to the prolonged duration until vitrification which allows diffusion limited polymers with free radical ends more time to propagate until they become trapped. If reactants are trapped the maximum attainable volumetric shrinkage decreases. By decreasing the irradiance the proportion of reactants that get trapped decrease and the autocatalytic model parameter *b* then increases. The rate parameter *a* decreases with lower irradiance because the rate of initiation decreases. Consequentially, the rate of polymerization decreases as well. The parameter *n* increased with decreasing LCU irradiance thus suggesting that the concentration of monomers is more significant for lower LCU irradiance. This can be understood from the the peak position equation which states that increasing the reaction order parameter *n* (while keeping *m* constant) makes the deflection value at which the peak deflection rate occurs move closer to zero (δ=0).

DC and deflection as a function of time follow very similar behavior where plotting the deflection versus the DC shows a linear trend. It is expected to see a positive correlation between DC and the deflection, that is, as the sample polymerizes the DC increases and consequentially the shrinkage increases. Any deviations from linearity as seen near 2.5% DC in the residuals are likely due to the microscopic nature of the measurement of the

DC, whereas deflection is a macroscopic effect. The microscopic nature refers to that the DC is measured locally over a 1 mm² on the surface of the RBC sample and that any contribution to axial shrinkage would be from the DC in the axial direction. The macroscopic effect refers to any shrinkage (in the axial direction) taking place within the sample is immediately measured by the deflection of the topmost surface of the sample. It is interesting to note that the slope (deflection over DC) is higher by 6% for the low power case than it is for the high power case which may be due to more time available for the monomers to propagate within the sample, due to a lower reaction rate, before monomers are trapped by vitrification**.**

It is observed that at the beginning of photopolymerization the deflection rate is temporarily larger than the DC rate. The DC is measured at the bottom surface of the RBC sample which is the furthest point away from the LCU. As the RBC used in this study undergoes curing the sample becomes less diffuse which allows more light to reach the bottom surface where the FTIR sensor is measuring. The relative irradiance throughout the depth of the sample increases with time as the sample is exposed to the LCU light. Meanwhile the shrinkage occurs throughout the sample. It is thus expected that initially the deflection would increase at a rate higher than the DC.

The autocatalytic equation has been used to fit the DC data**.** It is observed that despite the high degree of linearity observed between DC and deflection data, the normalized autocatalytic equation shows that the shrinkage and DC kinetics have different reaction order parameters. This is evidenced by the differences observed in the normalized

autocatalytic equation curves between DC and deflection as shown in Figure 45. The DC has been measured up to 53% at 876 mW LCU power due to an acquisition time of 100 s. It is expected that the DC and the shrinkage would proceed beyond the time that was measured. It may be that the linear relationship breaks down past 50% DC as seen in the paper by Stansbury [84]. In addition, the residual of the DC versus deflection shows some fluctuation that does not appear to be randomly distributed noise (e.g. Gaussian noise). Also note that silane treated filler in the RBC causes the measured DC to underestimate the true value associated with purely the double carbon bonds in the monomers due to additional double carbon bonds on the silane molecules adsorbed on the filler particles [89]. Further work is required to elucidate the mechanism for the difference in reaction order parameters between the deflection and DC.

5.4 SUMMARY

Despite a higher irradiance value for the turbo light guide the peak deflection rate is the same as it is for the standard light guide suggesting that shrinkage kinetics depend on the beam profile homogeneity. The greater the deflection rate the greater its uncertainty due to the relatively low sampling frequency, i.e. the time resolution, of the data acquisition system.

It was observed that time resolution of the interference pattern reconstruction can be improved by averaging the extrema for each pixel within a 1 mm² area at the sample's center. Variance in the reproducibility for each given experimental condition is likely due to the variance in the LCU output power from each time it was activated. For low and

high LCU power settings the RBC undergoes 5% and 45% of its total shrinkage by the time the LCU power is in a stable zone, respectively. At low power the results are more reproducible.

When the LCU turns off the deflection rate increases for high LCU power and decreases for low LCU power. Deflection rate increases due to thermal contraction and decreases due to decreased rate of photoinitiation. The rate of polymerization in dimethacrylate RBC is diffusion limited. By using a lower LCU irradiance the sample takes a longer time until vitrification occurs, allowing more time for diffusion of monomers toward active sites. At vitrification the monomer mobility is significantly reduced, thus using low irradiance results in more total conversion (i.e. total shrinkage) than at high irradiance.

The RBC sample's DC and deflection are well linearly correlated. The deviation from linearity is seen in the linear fit residual of deflection against DC. The difference in the reaction order parameters between DC and deflection is better observed in the figure showing the curves generated from the normalized autocatalytic equation. From a physical perspective, the difference between DC and deflection is that of a microscopic and macroscopic effect, respectively. The DC is measured locally at the sample's surface furthest from the LCU, whereas deflection is a bulk-effect where the entire sample is shrinking. The slope in deflection over DC is greater for low power than high power LCU which may be due to the delayed onset of vitrification at lower power LCU. Longer acquisition times for the DC and deflection are required to confirm if a linear relationship is maintained.

5.5 FIGURES AND TABLES

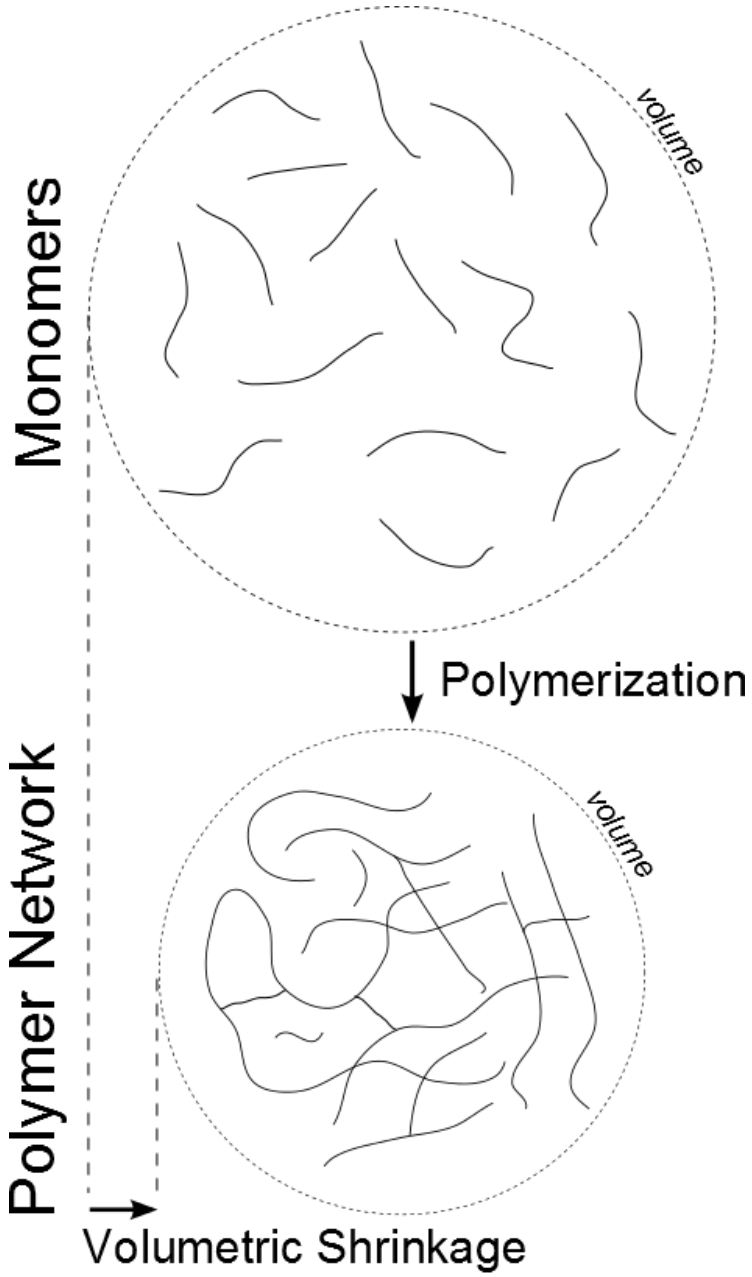

Figure 35 Illustration of the effect of polymerization induced volumetric shrinkage. The initial monomer configuration is loosely bound by Van der Waals forces. After polymerization, monomers form cross-linked polymer networks that are linked by covalent bonds. Covalent bonds being stronger than Van der Waals interaction the inter-molecular spacing decreases resulting in volumetric shrinkage. The dotted circle represents the volume of the monomer or polymer specimen.

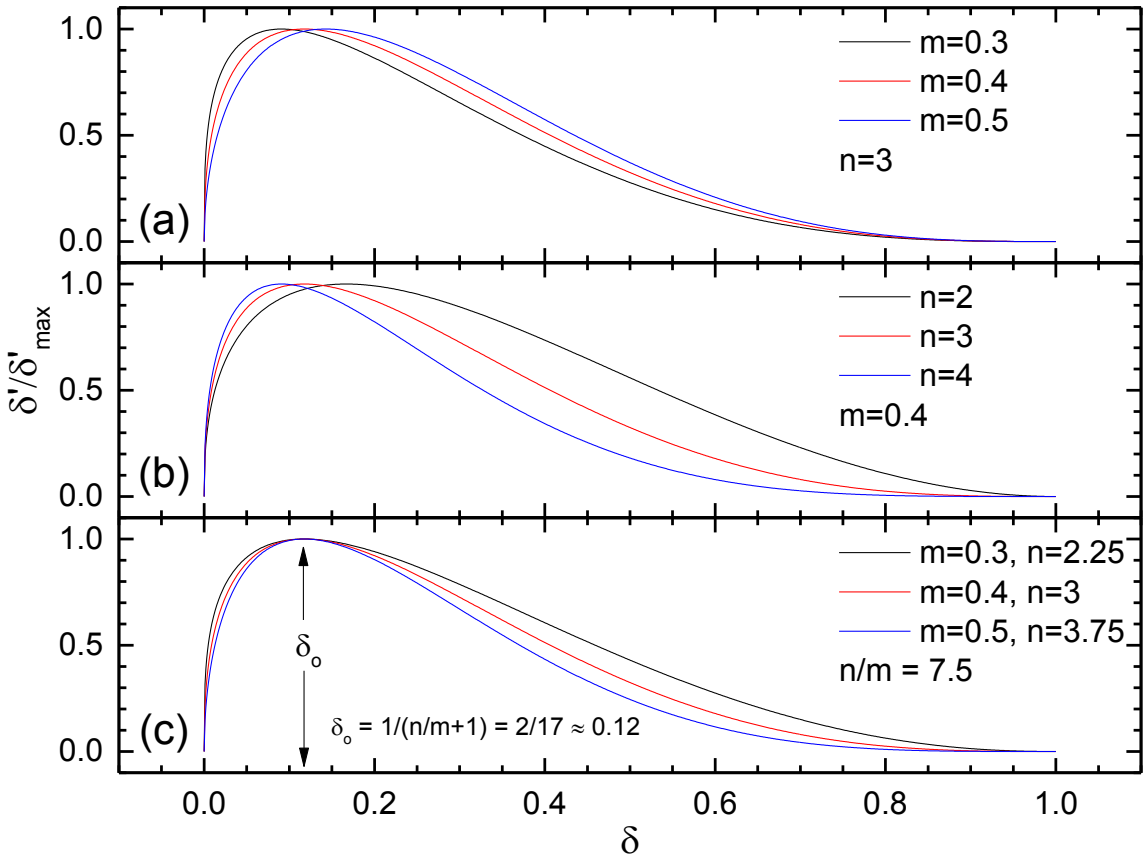

Figure 36 Curves of the normalized autocatalytic equation for different values of *m* and *n* while keeping *n* constant (a), while keeping *m* constant (b), and while keeping the ratio of *n* over *m* constant (c). The ratio of *n*/*m* is set to 7.5. The peak position (δ_o) is given by 1/(*n*/*m*+1) which comes to about 0.12. It is apparent that increasing *m* or *n* while keeping the ratio of *n*/*m* constant causes the peak to become narrower.

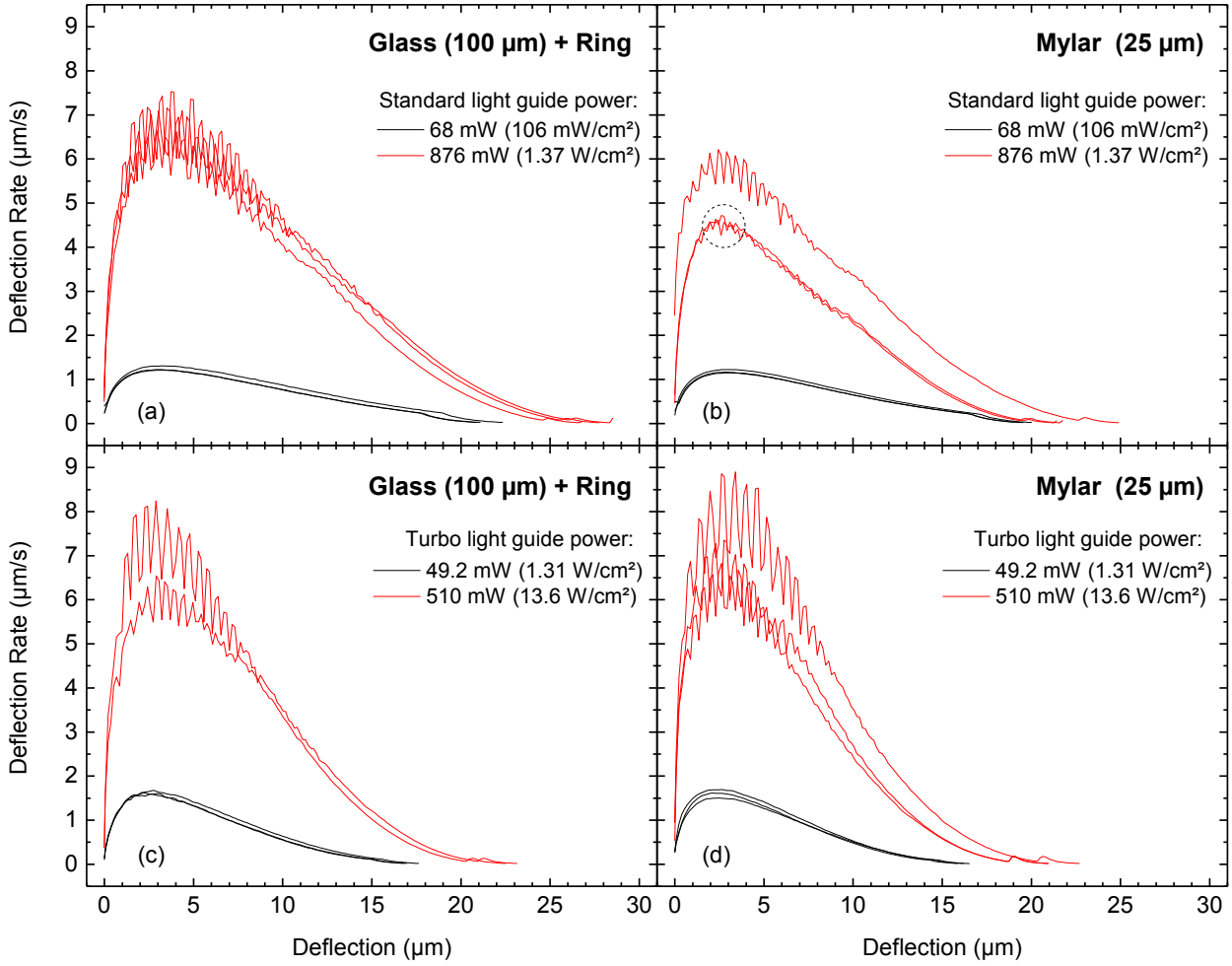

Figure 37 Deflection rate plotted against the deflection at the center of the sample for two RBC geometries, two LCU light guide types, and two power levels. The RBC samples are made with Filtek™ Supreme Ultra CT cured by a Sapphire® LCU set on bleach mode for 30 seconds. The two light guide types were standard (a,b) and turbo (c,d). The two RBC sample geometries used were with a 100 µm thick glass coverslip using a brass ring (a,c) and a 25 µm thick Mylar coverslip without a brass ring (b,d). The sample temperature was 22°C. The black and red lines correspond to low and high power modes, respectively. The total power output and irradiance of the LCU is given in the legend of each plot. All conditions were done with three repeats with the exception of two repeats for 510 mW in (c). Note that for two of the high power mode Mylar samples (lines enclosed by a dashed circle) in (b) the conditions differed in that, rather than the standard 1.22 mm, a 1.00 mm thick brass ring was used. It is expected that the shrinkage rate would be lower for a thinner sample. Note that the negative valued deflection and its rate were truncated so that the autocatalytic model could be used.

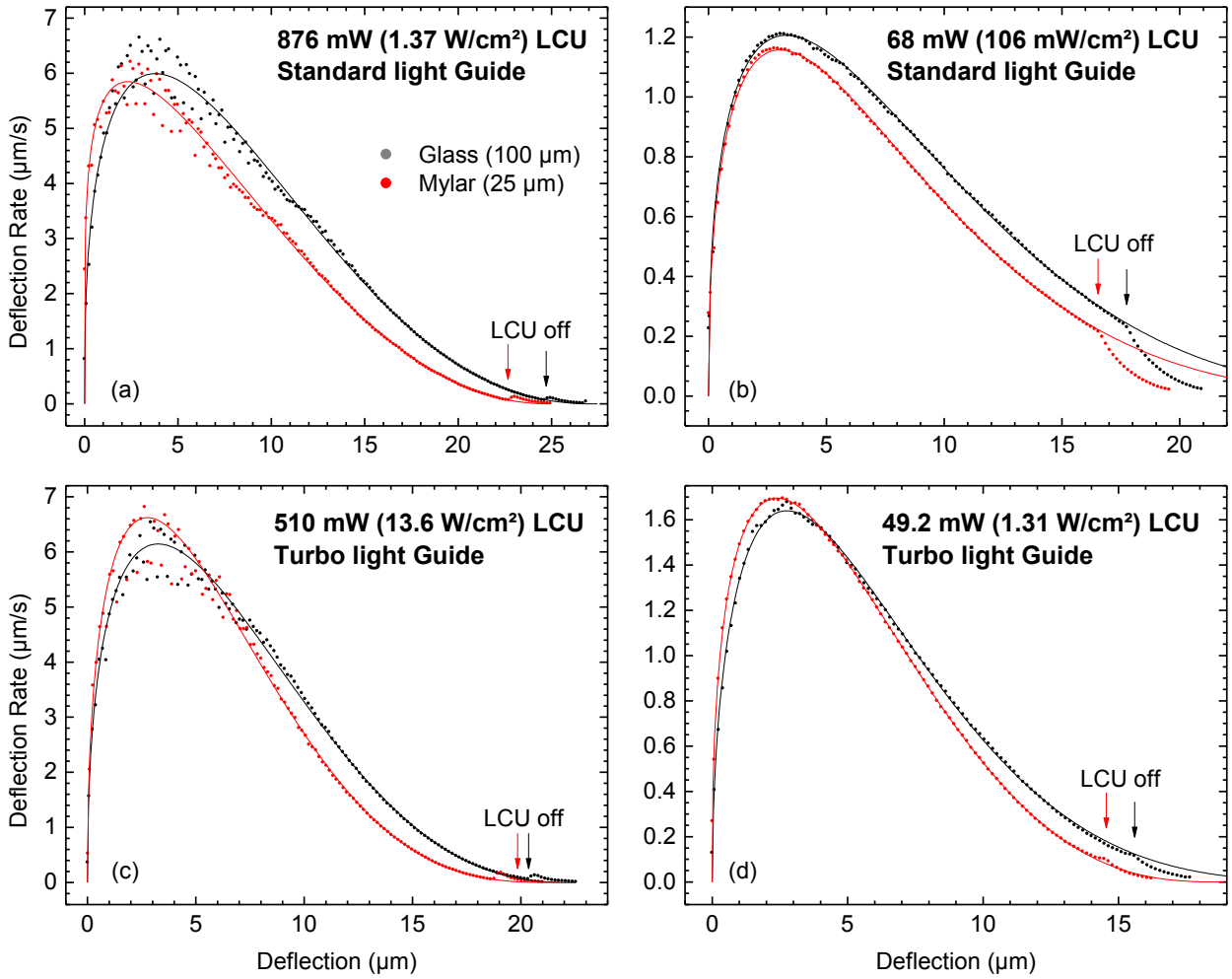

Figure 38 Deflection rate plotted against the deflection at the center of the sample of the raw data and its fit using the autocatalytic model for representative samples. The RBC samples are made with Filtek™ Supreme Ultra CT cured by a Sapphire® LCU set on bleach mode for 30 seconds. The two light guide types were standard (a,b) and turbo (c,d). High (a,c) and low (b,d) LCU output power and irradiance were used where the value is given in each plot. The sample temperature was 22°C. The black and red lines correspond to 100 µm thick glass and 25 µm thick Mylar coverslip sample geometries, respectively. The black and red arrows point to the deflection value at which the LCU turned off for the glass and Mylar coverslip cases, respectively. Note that different scales were used between figures to illustrate the fit of the data.

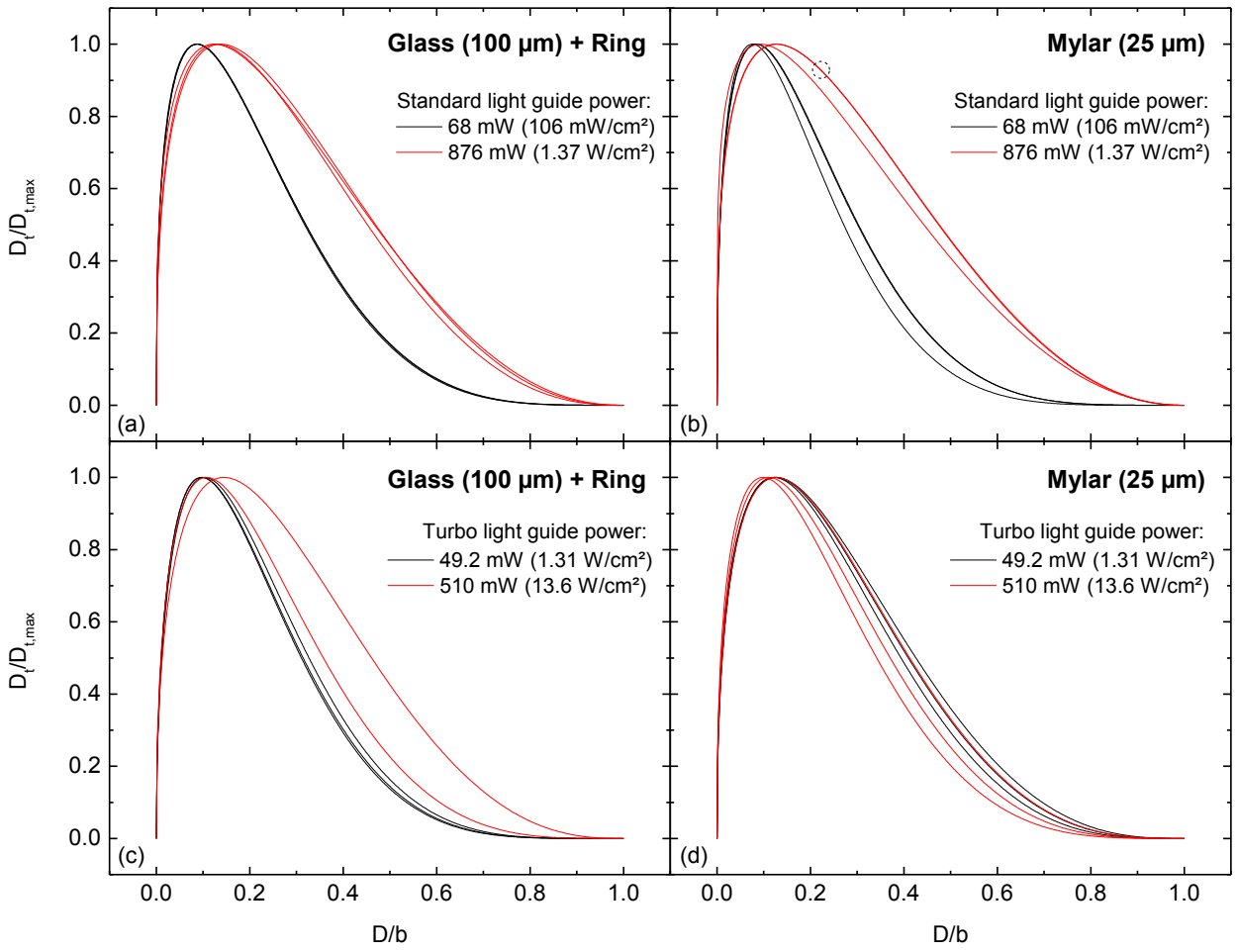

Figure 39 Comparison of the autocatalytic model fits to the deflection rate versus deflection at the center of the sample for different sample geometries. The y-axis is the deflection rate, D_t, normalized to the maximum deflection rate, $D_{t,max}$, calculated in the model. The x-axis is the deflection, D, normalized to the maximum attainable deflection, b, in the model. The RBC samples are made with Filtek™ Supreme Ultra CT cured by a Sapphire® LCU set on bleach mode for 30 seconds. The two light guide types were standard (a,b) and turbo (c,d). The two sample geometries used were with a 100 µm thick glass coverslip with a brass ring (a,c) and a 25 µm thick Mylar coverslip without a brass ring (b,d). The sample temperature was 22°C. The black and red lines correspond to low and high power modes, respectively. The total power output of the LCU is given in the legend of each plot. All conditions were done with three repeats with the exception of two repeats for 510 mW in (c). Note that for two of the high power mode Mylar samples (lines enclosed by a dashed circle) in (b) the conditions differed in that, rather than the standard 1.22 mm, a 1.00 mm thick brass ring was used.

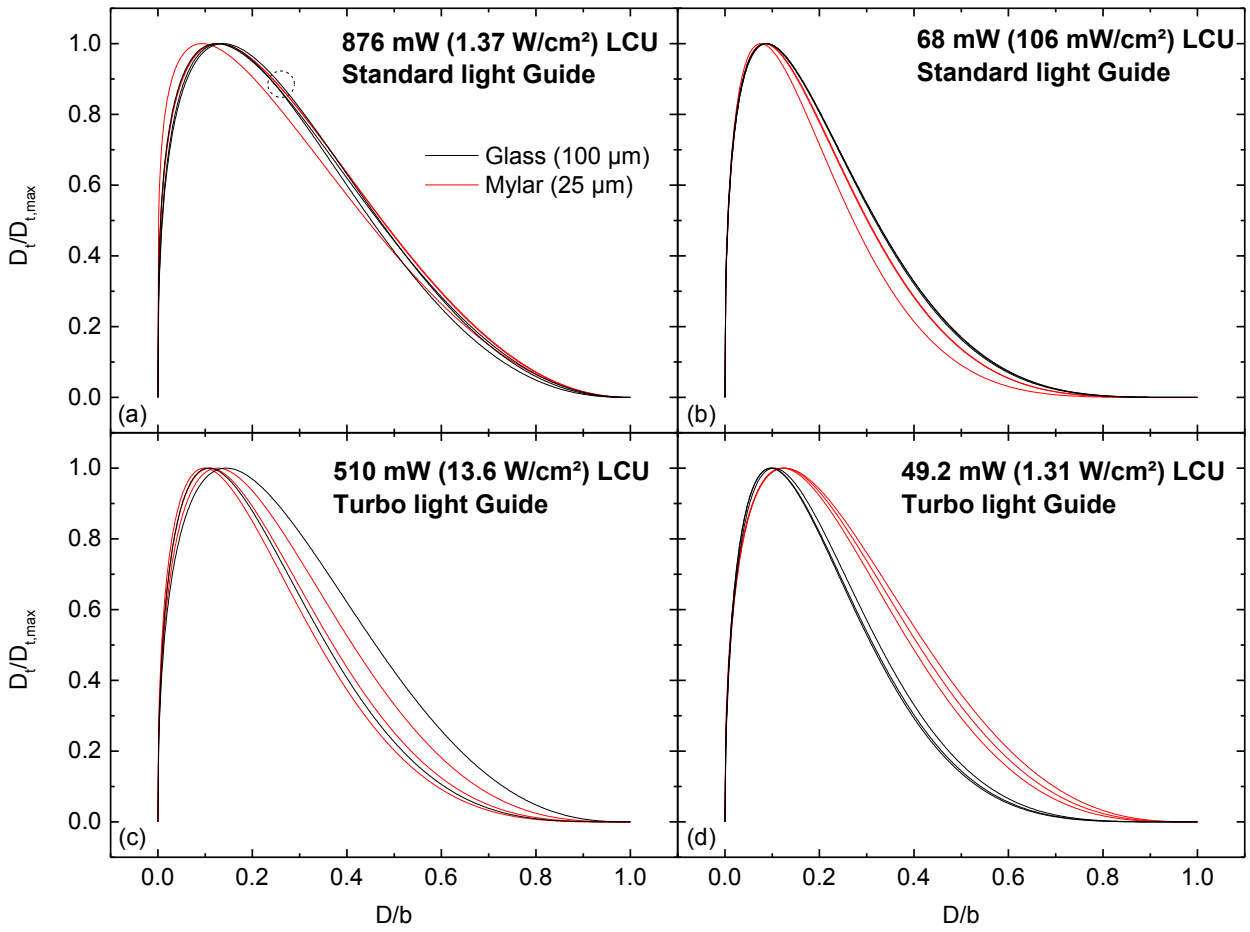

Figure 40 Deflection rate plotted against the deflection at the center of the sample of the raw data and its fit using the autocatalytic model for representative samples. The y-axis is the deflection rate, D_t, normalized to the maximum deflection rate, $D_{t,max}$, calculated in the model. The x-axis is the deflection, D, normalized to the maximum attainable deflection, b, in the model. The RBC samples are made with Filtek™ Supreme Ultra CT cured by a Sapphire® LCU set on bleach mode for 30 seconds. The two light guide types were standard (a,b) and turbo (c,d). High (a,c) and low (b,d) LCU output power were used where the value is given in each plot. The sample temperature was 22°C. The black and red lines correspond to 100 µm thick glass and 25 µm thick Mylar coverslip sample geometries, respectively. Note that the two curves for Mylar in (a) that are enclosed by a dashed circle were 1.00 mm thick samples rather than 1.22 mm.

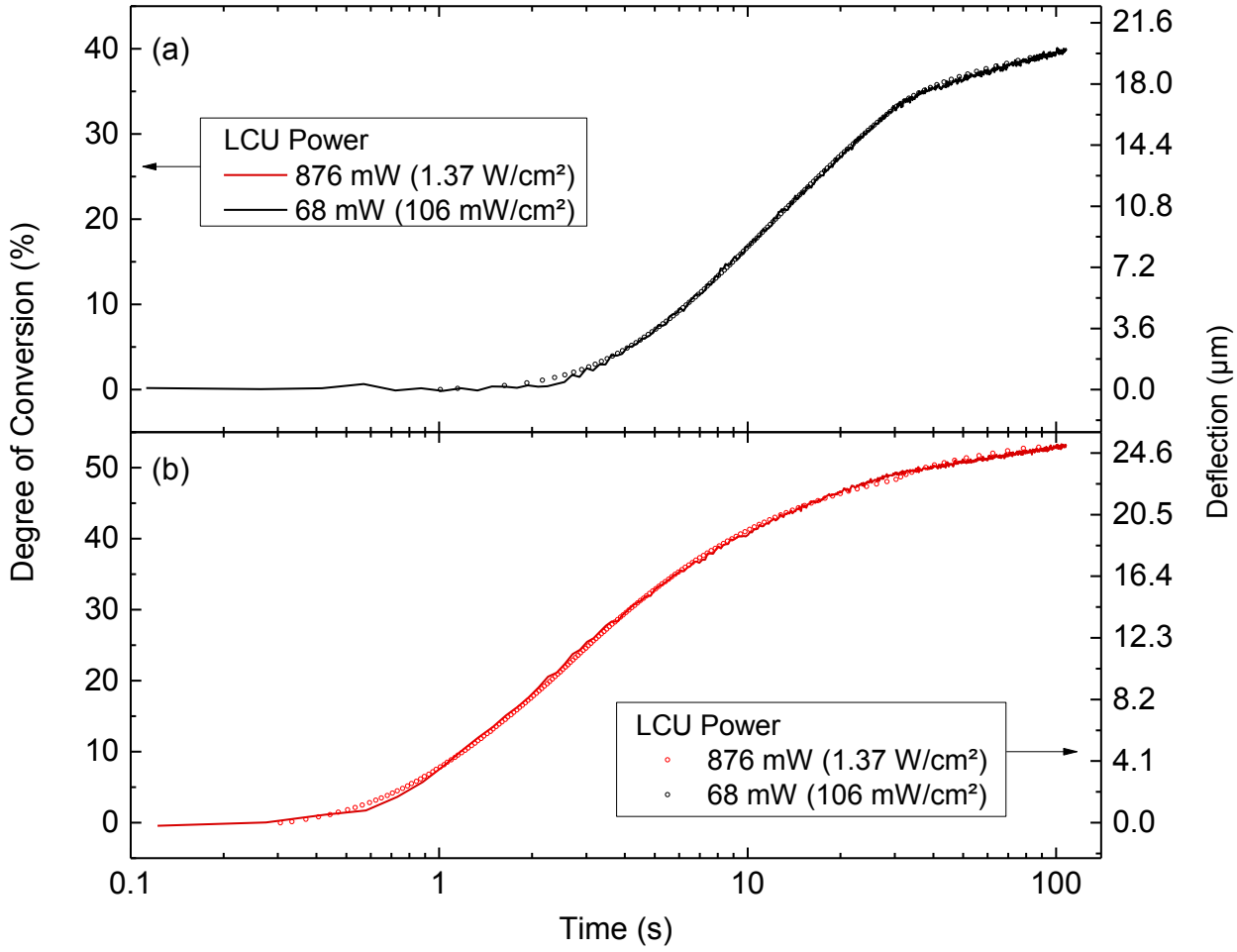

Figure 41 Degree of conversion (DC) and deflection as a function of time of Filtek™ Supreme Ultra CT cured by a Sapphire® LCU set on bleach mode for 30 seconds and a standard light guide. A LCU output power of 68 mW (a) and 876 mW (b) were used. The sample temperature was 22°C. The deflection and DC was measured at the center of the sample and on separate samples. The DC data is an average of three repeats. The deflection measurements were done with a 25 µm thick Mylar coverslip. The time axis corresponds to the duration beginning when the LCU was turned on. LCU activation timing is unknown for the DC data, so it was shifted in time until the sum of squares in the linear regression of deflection versus DC was minimized. Note that different scales were used between figures to illustrate the fit of the data.

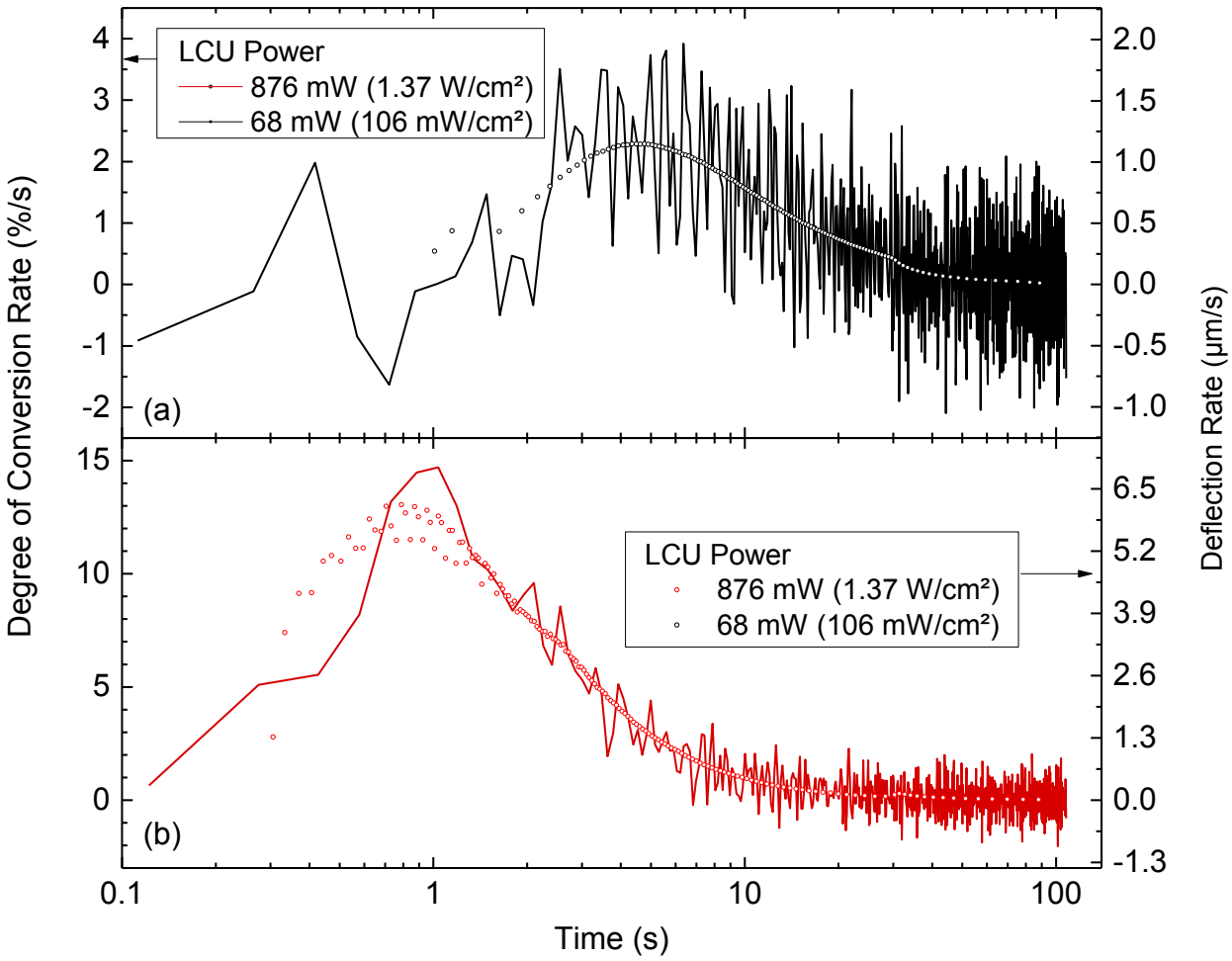

Figure 42 Degree of conversion (DC) rate and deflection rate as a function of time of Filtek™ Supreme Ultra CT cured by a Sapphire® LCU set on bleach mode for 30 seconds and a standard light guide. A LCU output power of 68 mW (a) and 876 mW (b) were used. The sample temperature was 22°C. The deflection and DC was measured at the center of the sample and on separate samples. The DC data is an average of three repeats. The rates are calculated taking the finite difference. The deflection measurements were done with a 25 µm thick Mylar coverslip. The time axis corresponds to the duration beginning when the LCU was turned on. LCU activation timing is unknown for the DC data, so it was shifted in time until the sum of squares in the linear regression of deflection versus DC was minimized. Note that different scales were used between figures to illustrate the fit of the data.

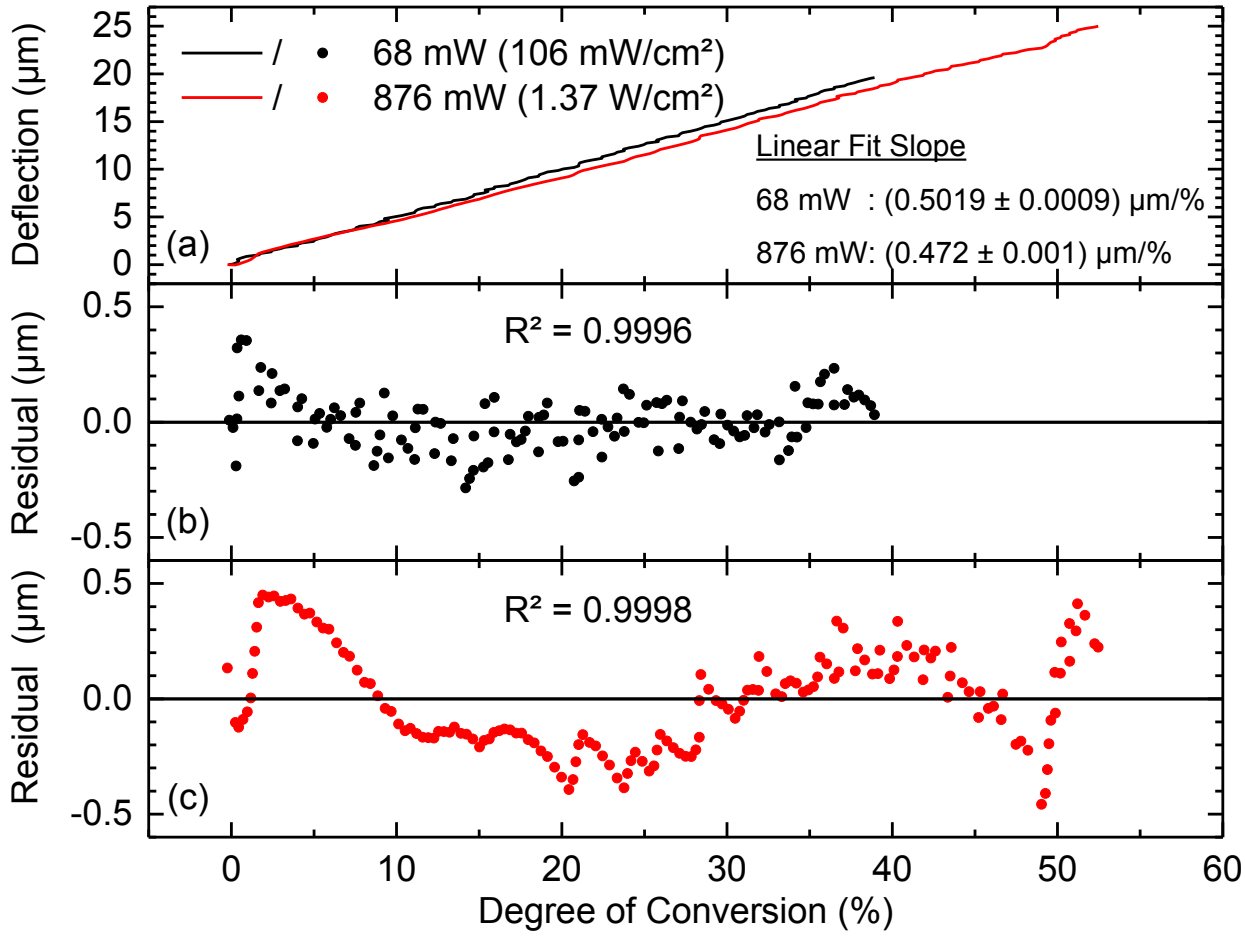

Figure 43 Deflection plotted as a function of degree of conversion (DC) of Filtek™ Supreme Ultra CT cured by a Sapphire® LCU set on bleach mode for 30 seconds and a standard light guide. The sample temperature was 22°C. The deflection and DC was measured at the center of the sample and on separate samples. (a) Low (68 mW) and high (876 mW) power results are plotted. The residual from a linear least squares fit on the data in (a) of the low and high power cases are shown in (b) and (c), respectively. The slopes (deflection/DC) and intercepts of the linear least square fit were 0.5019 µm/% and 0.472 µm/%, and 0.04 µm and -0.02 µm for 68 mW and 876 mW cases, respectively. The deflection measurements were done with a 25 µm thick Mylar coverslip and sample thickness of 1.22 mm.

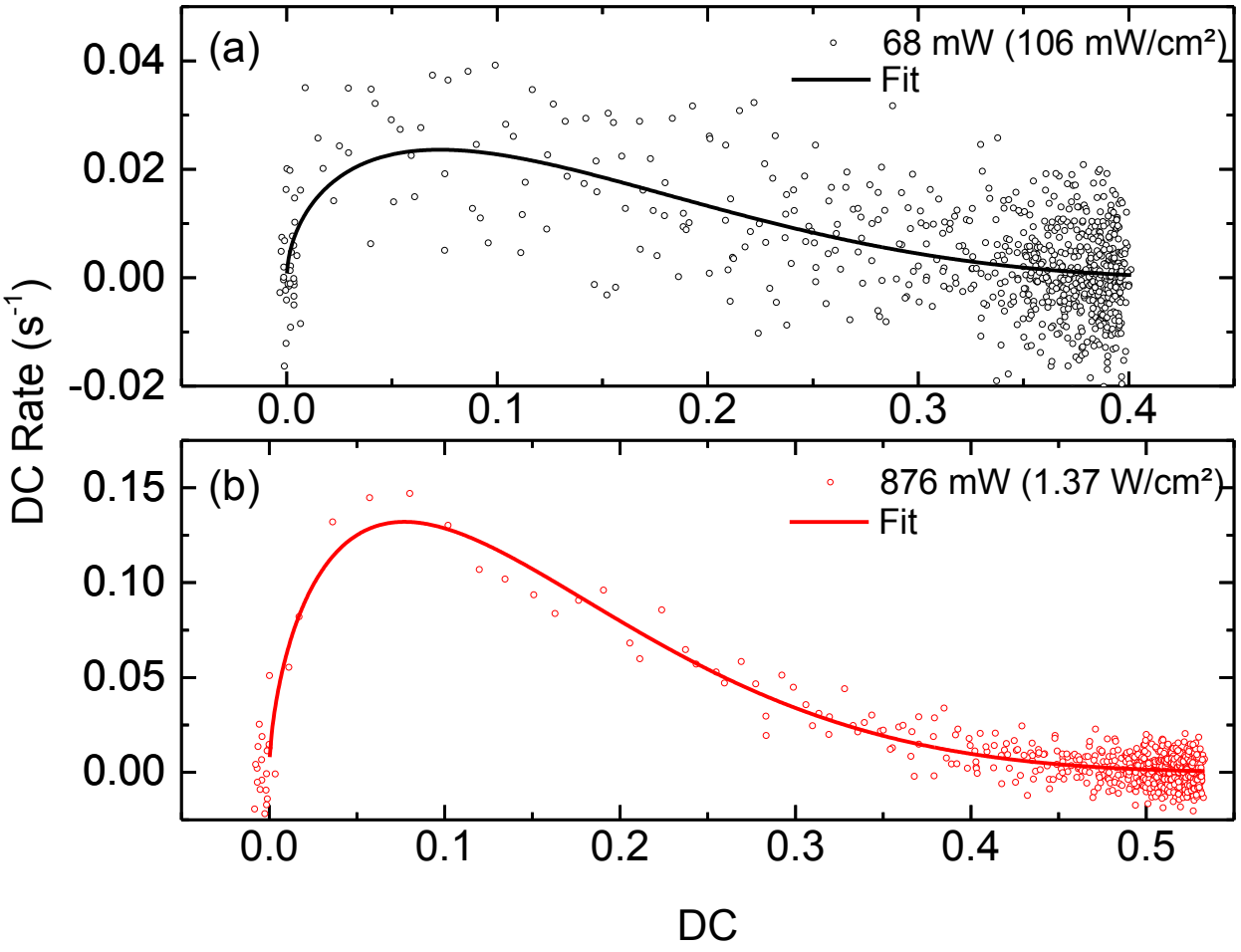

Figure 44 Autocatalytic model fits to the degree of conversion (DC) measurements. The RBC samples were made with Filtek™ Supreme Ultra CT cured by a Sapphire® LCU set on bleach mode for 30 seconds and a standard light guide. The sample temperature was 22°C. DC was measured at the sample center. The black (a) and red (b) lines correspond to LCU low (68 mW) and high (876 mW) power modes, respectively. For (a) the fitted parameters are: a=1±1, b=0.49±0.07, m=0.5±0.1, and n=3±1. For (b) the fitted parameters are: a=6±1, b=0.70±0.05, m=0.61±0.05, and n=5.0±0.7. Note that different scales were used between figures to illustrate the fit of the data.

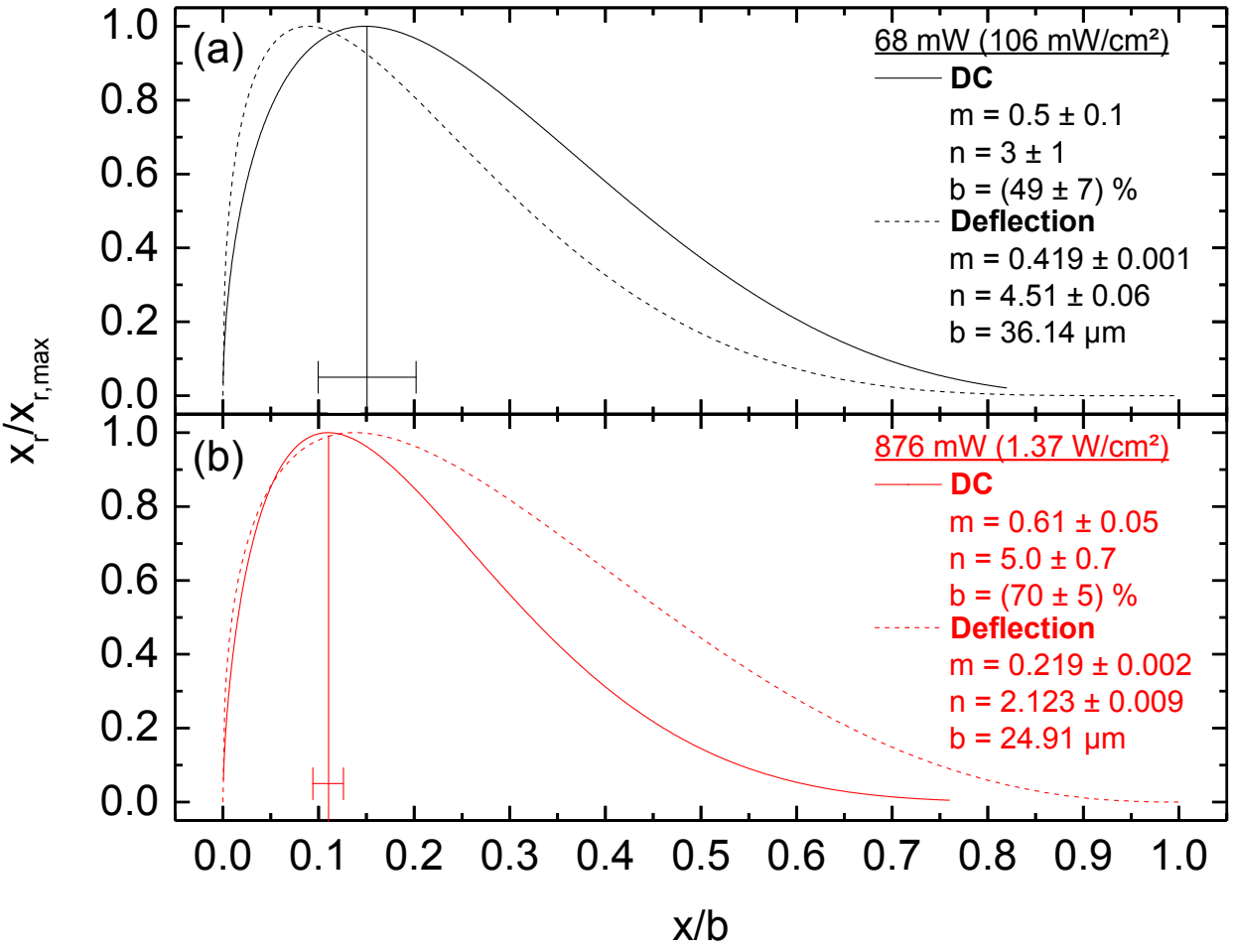

Figure 45 Comparison of the autocatalytic model fits for the degree of conversion (DC) and deflection measurements. The DC and deflection were measured at the sample center using different samples. The sample temperature was 22°C. The y-axis is the DC (or deflection) rate, x_t, normalized to the maximum rate, $x_{t,max}$, calculated in the model. The x-axis is the DC or *D* (deflection), normalized to the maximum attainable DC (or deflection), *b*, in the model. The parameter, *x*, can be either DC or the deflection. The RBC samples were made with Filtek™ Supreme Ultra CT cured by a Sapphire® LCU set on bleach mode for 30 seconds and a standard light guide. The same geometry was brass ring with 100 µm thick glass coverslip for shrinkage data. The black (a) and red (b) lines correspond to LCU low (68 mW) and high power (876 mW) modes, respectively. The fitted parameters *m*, *n,* and *b* are given within the legend for the corresponding case. Horizontal error bars shown in (a) and (b) indicate the uncertainty in the peak normalized DC rate position.

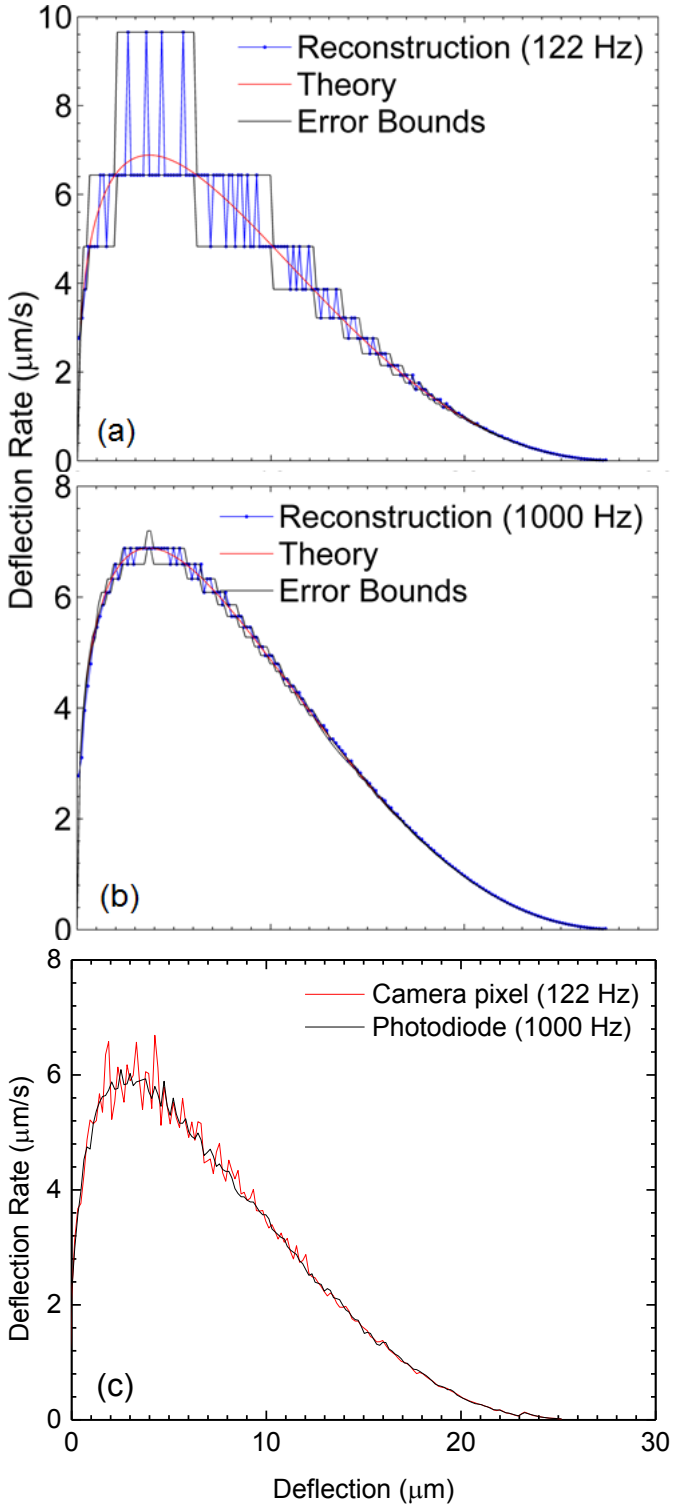

Figure 46 Simulation of the sampling rate dependence of the deflection rate error from the interference pattern reconstruction. A sampling rate of 122 Hz (a) and 1000 Hz (b) were chosen to correspond to the camera and photodiode sampling rates, respectively. The theoretical curve (red lines) is calculated using the autocatalytic equation. The reconstructed data (blue lines) was derived using the MATLAB peak locating algorithm on the digitized interference pattern and was generated by solving the autocatalytic

equation. The autocatalytic equation parameters were m=0.359, n=2.39, a=0.00202, b=28.4. The error bounds (black lines) display the range in the uncertainty of the deflection rate at the given sampling rate. The peak locating algorithm did not interpolate between acquired data points, so the peak position uncertainty range can be as great as the time interval between them. The error bounds shown are calculated by allowing only for integer multiples of the sampling interval. The upper and lower bounds are from the rounded down and up interval, respectively. An example of experimental data collected using a camera (122 Hz) and photodiode (1000 Hz) is shown in panel (c).

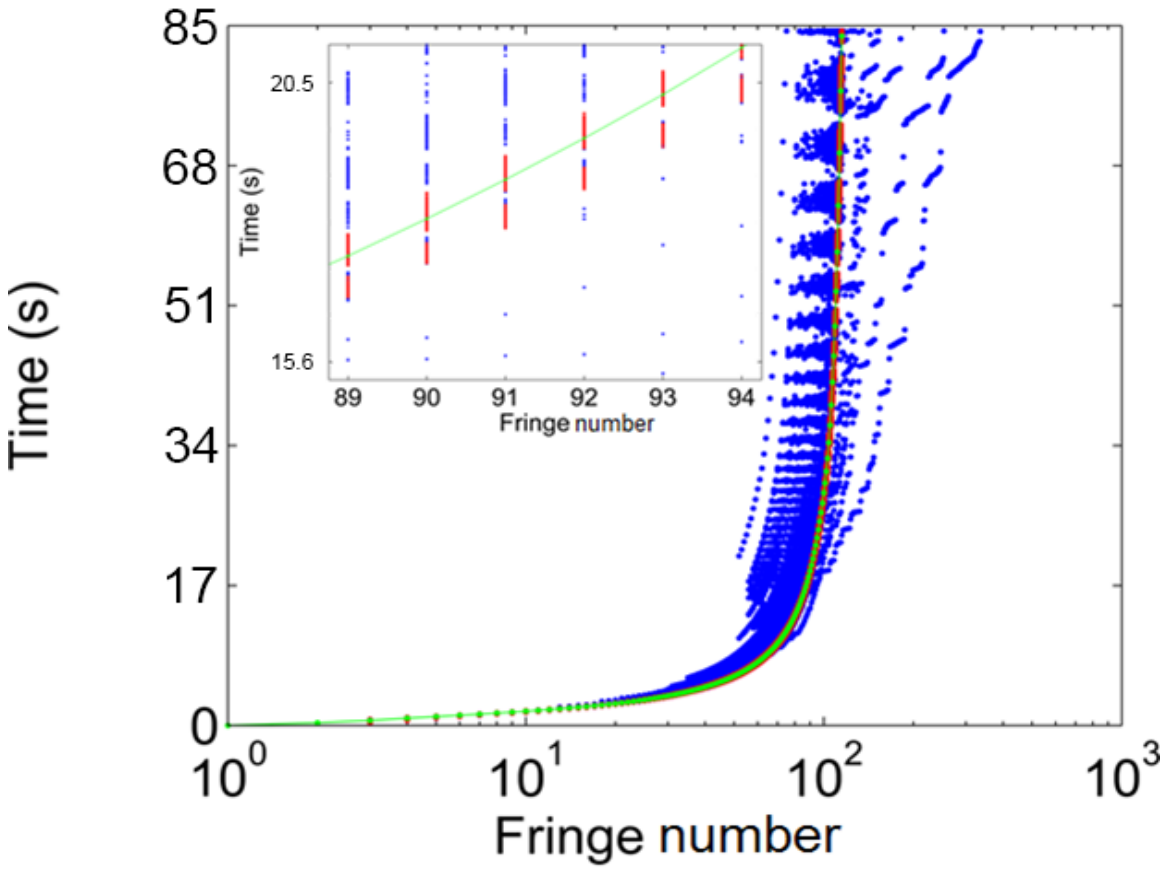

Figure 47 Aggregated results of the peak finding algorithm over a 1 mm x 1mm square area at the sample's center. The blue data is the aggregation over all results. The red data represents the results for all the points within the 1 mm² area that satisfy the condition that the total number of fringes at the end of acquisition, time final, is equal to the median value. The median value is calculated from the data at the final time for all points. The green data connected by a line, as a guide for the eye, is derived by taking the mean across the time axis for each fringe number of the red data.

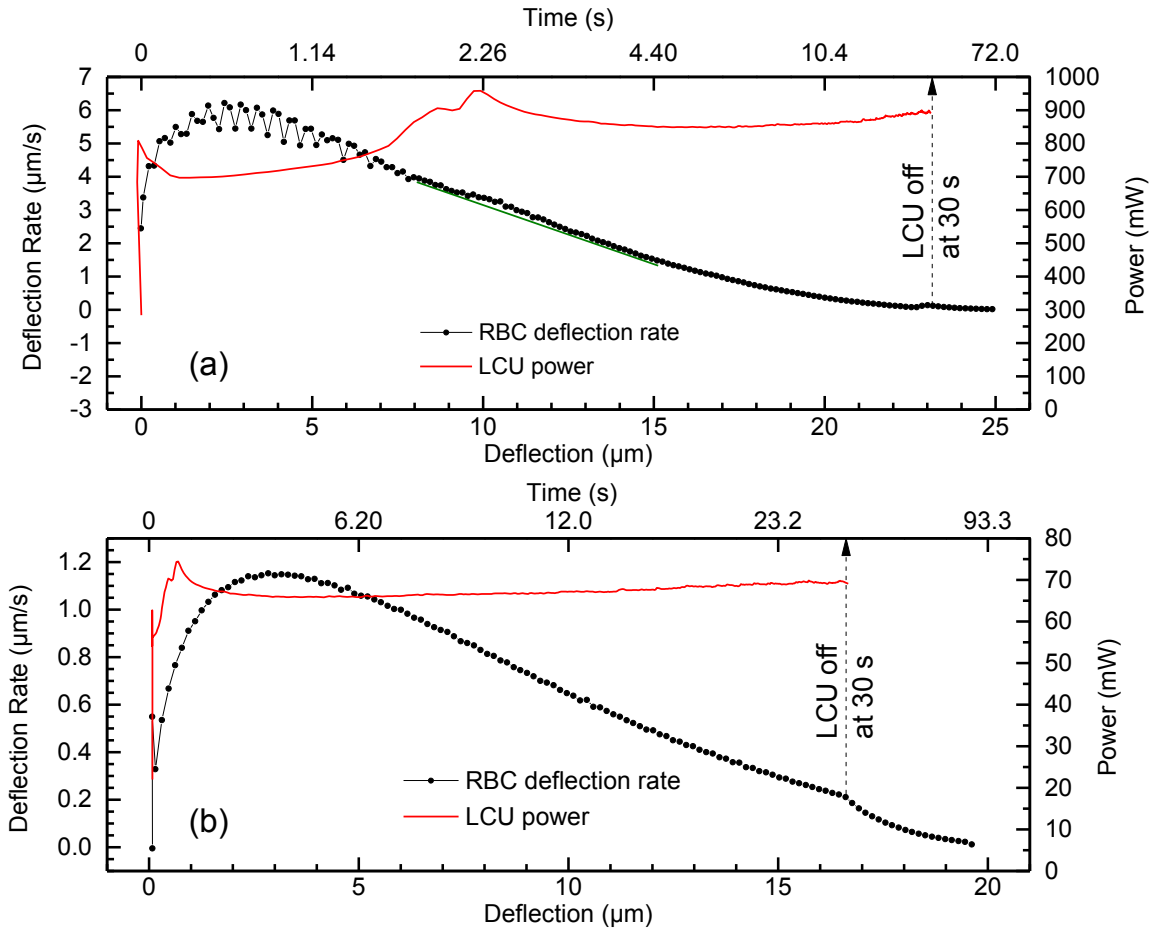

Figure 48 Overlay of the RBC shrinkage kinetics and the corresponding LCU output power. The optical spectrum of the Sapphire® LCU using a standard light guide was acquired as a function of time using an integrating sphere and an Ocean Optics USB4000 spectrometer. The RBC sample consisted of Filtek Supreme Ultra CT. The sample geometries were glass coverslip with a brass ring. The sample temperature was 22°C. Results were acquired for when the LCU was set on bleach mode (a) and when a light attenuation filter was present to cut the power (b). The acquired spectra were integrated over the 350 nm to 550 nm wavelength range to get the total power. The LCU power is the average of 5 repeats and where the relative standard deviation to the average at 30 s is 4.5%. At 30 s the LCU was turned off. The measured time dependent RBC sample deflection at a given time was used to determine the LCU power as a function of RBC deflection displayed in (a) and (b). A bump-like shape in (a) at 10 µm is emphasized by the gap formed between the RBC deflection rate data points and a linear green line. Note that the time axis is non-linear and that different scales were used between figures to illustrate the variation of the data.

Table 2 Derived parameters from the autocatalytic model least square fits to the deflection rate versus deflection for different sample conditions are shown. The specifics of the sample conditions are given in the table. The RBC sample thickness was 1.22 mm and the LCU irradiation time was 30 s. The mean and standard deviation (S.D.) of each parameter is determined from three repeats with the exception of glass coverslip at 510 mW LCU power using a turbo light guide which was from two repeats. Note that for Mylar coverslip at 876 mW LCU power using a standard light guide only the result with a RBC sample thickness of 1.22 mm is included hence no standard deviation is given.

LCU	PAC with standard light guide							
Coverslip	glass (100 μm) + ring				Mylar (25 μm)			
LCU Power	876 mW		68 mW		876 mW		68 mW	
Parameter	**Mean**	**S.D.**	**Mean**	**S.D.**	**Mean**	**S.D.**	**Mean**	**S.D.**
m	0.36	0.03	0.394	0.008	0.219	-	0.420	0.007
n	2.4	0.1	4.11	0.05	2.12	-	4.7	0.3
b (μm)	28.4	0.7	38	1	24.9	-	38	2
a	2.0E-3	8E-4	3.7E-07	9E-08	6.5E-3	-	7E-08	5E-08
LCU	PAC with Turbo light guide							
Coverslip	glass (100 μm) + ring				Mylar (25 μm)			
LCU Power	510 mW		49.2 mW		510 mW		49.2 mW	
Parameter	**Mean**	**S.D.**	**Mean**	**S.D.**	**Mean**	**S.D.**	**Mean**	**S.D.**
m	0.436	0.009	0.44	0.02	0.449	0.008	0.514	0.006
n	3.5	0.3	3.1	0.2	3.2	0.6	4.7	0.1
b (μm)	24	1	19.7	0.6	25	2	26.40	0.08
a	2E-4	2E-4	2E-4	1E-4	8E-4	8E-4	4E-07	1E-07

Chapter 6
CONCLUSION

A novel approach using a Michelson interferometer was used to measure the full axial shrinkage field across the RBC sample surface in real time before, during, and after photopolymerization. The main components of the apparatus consist of a Helium-Neon (HeNe) laser and a CCD camera with 122 frames per second acquisition rate capable of measuring shrinkage rates up to 19.3 μm/s and with a spatial resolution on the sample of 20.6 μm. The sample geometry utilised is a modification of the bonded disc method. The advantage of this approach relative to previous methods is that it has a good balance of both high spatial and temporal resolution. The high spatial accuracy of the new set up was verified by using three spherical concave mirrors where their focal lengths determined using Michelson interferometry were in excellent agreement with the manufacturer's specifications. Moreover, the topography of a typical cured RBC sample determined by Michelson interferometry was in excellent agreement with that measured using profilometry. The high temporal resolution of the camera data acquisition system was confirmed using the data obtained from the Silicon photodiode and its parallel data acquisition system. It was shown that the novel approach can monitor the fast axial shrinkage field across the RBC sample surface under clinical light exposure conditions.

It was concluded that the LCU beam profile and sample geometry does play a role in the measurement of the 2D axial deflection map and shrinkage kinetics at the center of the sample. The glass coverslip induces extra axial deflection towards the RBC's periphery due to a central fast curing region causing the bent coverslip to apply a downward pressure on the pre-vitrified RBC. This causes off-center RBC to deform radially and

axially in addition to photopolymerization induced axial shrinkage thus exhibiting a total axial deflection at the sample's periphery to be larger than at its center. This effect is more pronounced when the LCU irradiance beam profile is inhomogenous (e.g. Gaussian-like shape) and the total output power is low. This makes a larger difference for the polymerization rate of the RBC sample between its center and periphery. Also, at low output power the viscoelastic properties of the RBC becomes significant where the shrinkage kinetics is affected by the coverslip rigidity and the boundary conditions set by the brass ring. Based on the results in this thesis it is recommended that for the bonded disc geometry a 25 μm thick Mylar coverslip be used with a high C-factor to minimize the effects of the coverslip induced axial deflection. Otherwise, a glass coverslip may be used if the LCU emits a uniform beam profile.

To study the effect of an inhomogeneous irradiance beam profile radiated by a polywave LCU on the axial shrinkage of RBC samples, a Bluephase Style LCU manufactured by Ivoclar Vivadent was used. The LCU consisted of two blue LEDs radiating near 460 nm, and one violet LED emitting near 405 nm. Results show a strong qualitative correlation between the LCU irradiance beam profile, LED emission wavelength, and the RBC type and its axial shrinkage map shortly after the beginning of irradiation. With increasing exposure time the correlation is obfuscated as the shrinkage becomes more uniform throughout the sample.

Numerical analysis and experimental results showed that the greater the deflection rate of the RBC sample the greater the uncertainty of its measured value due to the finite sampling rate of the camera. The uncertainty is reduced by averaging the times at which extrema occur in the interference pattern for each pixel within a 1 mm^2 area at the

sample's center. Overall the variance in the shrinkage kinetics and shrinkage field is possibly due to the variance in the LCU output power from each time it is activated. In addition to that, the output power fluctuates as a function of time. For example, for low and high LCU power setting the RBC undergoes 5% and 45% of its total shrinkage by the time the LCU power is mostly stabilized, respectively, hence at low power the results are more reproducible.

The fitting of the data using the autocatalytic model predicts that the final deflection of the RBC is higher for a lower LCU irradiance. This effect may be due to the delayed onset of vitrification and that the rate of polymerization in dimethacrylate RBCs is diffusion limited. Therefore by using a lower LCU irradiance the sample takes a longer time until vitrification allowing more time for diffusion of monomers towards active sites. At vitrification the monomer mobility is significantly reduced thus lower irradiance results in more total conversion, i.e. total shrinkage, than at high irradiance.

The RBC sample DC and deflection is linearly correlated for the measured range of values. The deviation from linearity is seen in the linear fit residual of deflection against DC. The difference between DC and deflection is that of a microscopic and macroscopic effect, respectively. DC is measured locally at the sample's surface furthest from the LCU whereas deflection is a bulk-effect where the entire sample is shrinking.

The limitations of this approach to measuring the polymerization shrinkage of RBCs is that it requires a specific sample geometry, the maximum measurable deflection rate of the sample is dictated by the acquisition rate of the camera, and that only axial shrinkage is measured. The constraints in the sample geometry are that a flexible smooth reflecting

coverslip on top of the sample is necessary. It needs to satisfy two functions - a specularly reflecting surface so that the incident laser beam is not diffusely reflected and when the sample deforms the coverslip is flexible enough to easily contort to its curvature.

6.1 Future Work

In light of the results in this thesis, some of the future work would be to examine if using a Mylar coverslip changes the configuration factor of the sample. This can be studied by decreasing the sample diameter, thus decreasing the configuration factor, to see if the RBC sample shrinks less in proportion to its thickness. The role of the RBC viscosity on the shrinkage for a given C-factor is of importance. Similar conditions using a glass coverslip can then be compared. It would also be of interest to cross-correlate the 2D shrinkage maps, hardness maps, and DC maps. This will give additional insight into the interplay of RBC's desirable properties (i.e. high DC and hardness) with undesirable ones (i.e. high shrinkage). For the FTIR DC measurements it is important to get an accurate measurement of when the LCU is turned on during the data acquisition. This way the DC and deflection data are better synchronized leading to a more accurate and in depth analysis. In addition, extending the data acquisition time to at least 15 min for 876 mW and 1 hr for 67 mW would elucidate if deflection and DC continue to correlate linearly at long time. The duration for which the LCU is kept on should also be extended for as long as possible since the shrinkage kinetics are observed to change upon turning off the LCU. Using a LCU with constant output power when turned on and that doesn't change for each use would be helpful in getting less variability in the shrinkage results. Lastly, by

irradiating the RBC sample using a short duration (<8 ms) high power LCU output a large amount of free radicals can be generated without significant shrinkage taking place before the LCU light is turned off. This way the free radical polymerization consisting of only the propagation and termination reactions, but without the creation of more free radical by photoinitiation (after the initial short duration of generated radicals), can be studied from the shrinkage and DC data.

BIBLIOGRAPHY

[1] Cramer NB, Stansbury JW, Bowman CN. Recent advances and developments in composite dental restorative materials. J Dent Res 2011;90:402–16.

[2] Bowman CN, Kloxin CJ. Toward an enhanced understanding and implementation of photopolymerization reactions. AIChE J 2008;54:2775–95.

[3] Andrzejewska E. Photopolymerization kinetics of multifunctional monomers. Prog Polym Sci 2001;26:605–65.

[4] Decker C. The use of UV irradiation in polymerization. Polym Int 1998;45:133–41.

[5] Decker C. Photoinitiated crosslinking polymerisation. Prog Polym Sci 1996;21:593–650.

[6] Decker C, Elzaouk B, Decker D. Kinetic study of ultrafast photopolymerization reactions. J Macromol {Science-Pure} Appl Chem 1996;A33:173–90.

[7] Ferracane JL. Resin composite--state of the art. Dent Mater 2011;27:29–38.

[8] Leprince JG, Palin WM, Hadis MA, Devaux J, Leloup G. Progress in dimethacrylate-based dental composite technology and curing efficiency. Dent Mater 2013;29:139–56.

[9] Heintze SD, Rousson V. Clinical effectiveness of direct class II restorations - a meta-analysis. J Adhes Dent 2012;14:407–31.

[10] Sunnegårdh-Grönberg K, van Dijken JW V, Funegård U, Lindberg A, Nilsson M. Selection of dental materials and longevity of replaced restorations in Public Dental Health clinics in northern Sweden. J Dent 2009;37:673–8.

[11] Simecek JW, Diefenderfer KE, Cohen ME. An evaluation of replacement rates for posterior resin-based composite and amalgam restorations in U.S. Navy and marine corps recruits. J Am Dent Assoc 2009;140:200–209; quiz 249.

[12] Braga RR, Ballester RY, Ferracane JL. Factors involved in the development of polymerization shrinkage stress in resin-composites: a systematic review. Dent Mater 2005;21:962–70.

[13] Kleverlaan CJ, Feilzer AJ. Polymerization shrinkage and contraction stress of dental resin composites. Dent Mater 2005;21:1150–7.

[14] Schneider LFJ, Cavalcante LM, Silikas N. Shrinkage Stresses Generated during Resin-Composite Applications: A Review. J Dent Biomech 2010;2010.

[15] Ryan V, Hart T, Schiller R. Size determination of Streptococcus mutans 10499 by laser light scattering. Biophys J 1980;31:313–24.

[16] Atai M, Watts DC. A new kinetic model for the photopolymerization shrinkage-strain of dental composites and resin-monomers. Dent Mater 2006;22:785–91.

[17] Boulden JE, Cramer NB, Schreck KM, Couch CL, Bracho-Troconis C, Stansbury JW, et al. Thiol-ene-methacrylate composites as dental restorative materials. Dent Mater 2011;27:267–72.

[18] Lien W, Vandewalle KS. Physical properties of a new silorane-based restorative system. Dent Mater 2010;26:337–44.

[19] Gonçalves F, Pfeifer CCS, Stansbury JW, Newman SM, Braga RR. Influence of matrix composition on polymerization stress development of experimental composites. Dent Mater 2010;26:697–703.

[20] Leprince JG, Hadis M, Shortall a C, Ferracane JL, Devaux J, Leloup G, et al. Photoinitiator type and applicability of exposure reciprocity law in filled and unfilled photoactive resins. Dent Mater 2011;27:157–64.

[21] Min S-H, Ferracane J, Lee I-B. Effect of shrinkage strain, modulus, and instrument compliance on polymerization shrinkage stress of light-cured composites during the initial curing stage. Dent Mater 2010;26:1024–33.

[22] Geiser V, Leterrier Y, Månson J-AE. Conversion and shrinkage analysis of acrylated hyperbranched polymer nanocomposites. J Appl Polym Sci 2009;114:1954–63.

[23] Atai M, Ahmadi M, Babanzadeh S, Watts DC. Synthesis, characterization, shrinkage and curing kinetics of a new low-shrinkage urethane dimethacrylate monomer for dental applications. Dent Mater 2007;23:1030–41.

[24] Floyd CJE, Dickens SH. Network structure of Bis-GMA- and UDMA-based resin systems. Dent Mater 2006;22:1143–9.

[25] Atai M, Watts DC, Atai Z. Shrinkage strain-rates of dental resin-monomer and composite systems. Biomaterials 2005;26:5015–20.

[26] Decker C. Photoinitiated crosslinking polymerisation. Prog Polym Sci 1996;21:593–650.

[27] Decker C, Elzaouk B, Decker D. Kinetic study of ultrafast photopolymerization reactions. J Macromol {Science-Pure} Appl Chem 1996;A33:173–90.

[28] Kugel G, Ferrari M. The science of bonding: from first to sixth generation. J Am Dent Assoc 2000;131 Suppl:20S–25S.

[29] De Gee AJ, Davidson CL, Smith A. A modified dilatometer for continuous recording of volumetric polymerization shrinkage of composite restorative materials. J Dent 1981;9:36–42.

[30] Rosin M, Urban AD, Gärtner C, Bernhardt O, Splieth C, Meyer G. Polymerization shrinkage-strain and microleakage in dentin-bordered cavities of chemically and light-cured restorative materials. Dent Mater 2002;18:521–8.

[31] Sakaguchi RL, Wiltbank BD, Shah NC. Critical configuration analysis of four methods for measuring polymerization shrinkage strain of composites. Dent Mater 2004;20:388–96.

[32] Yamamoto A, Miyazaki M, Rikuta A, Kurokawa H, Takamizawa T. Comparison of two methods for measuring the polymerization characteristics of flowable resin composites. Dent Mater 2007;23:792–8.

[33] Watts DC, Kisumbi BK, Toworfe GK. Dimensional changes of resin/ionomer restoratives in aqueous and neutral media. Dent Mater 2000;16:89–96.

[34] Lee IB, Cho BH, Son HH, Um CM. A new method to measure the polymerization shrinkage kinetics of light cured composites. J Oral Rehabil 2005;32:304–14.

[35] Dewaele M, Truffier-Boutry D, Devaux J, Leloup G. Volume contraction in photocured dental resins: the shrinkage-conversion relationship revisited. Dent Mater 2006;22:359–65.

[36] De Melo Monteiro GQ, Montes MAJR, Rolim TV, de Oliveira Mota CCB, de Barros Correia Kyotoku B, Gomes ASL, et al. Alternative methods for determining shrinkage in restorative resin composites. Dent Mater 2011;27:e176–85.

[37] Cook WD, Forrest M, Goodwin AA. A simple method for the measurement of polymerization shrinkage in dental composites. Dent Mater 1999;15:447–9.

[38] Watts DC, Cash AJ. Determination of polymerization shrinkage kinetics in visible-light-cured materials: methods development. Dent Mater 1991;7:281–7.

[39] Wilson HJ. Properties of radiation-cured restorative resins. Proc. Int. Symp. Fotofil Dent. Restorative, Franklin Sci. Proj. London, 1978, p. 11–6.

[40] Watts DC, Marouf AS. Optimal specimen geometry in bonded-disk shrinkage-strain measurements on light-cured biomaterials. Dent Mater 2000;16:447–51.

[41] Lee I-B, Cho B-H, Son H-H, Um C-M, Lim B-S. The effect of consistency, specimen geometry and adhesion on the axial polymerization shrinkage measurement of light cured composites. Dent Mater 2006;22:1071–9.

[42] Simon Y, Mortier E, Dahoun A, Gerdolle D. Video-controlled characterization of polymerization shrinkage in light-cured dental composites. Polym Test 2008;27:717–21.

[43] Spinell T, Schedle A, Watts DC. Polymerization shrinkage kinetics of dimethacrylate resin-cements. Dent Mater 2009;25:1058–66.

[44] Sakaguchi RL, Sasik CT, Bunczak MA, Douglas WH. Strain gauge method for measuring polymerization contraction of composite restoratives. J Dent 1991;19:312–6.

[45] De Gee AF, Feilzer AJ, Davidson CL. True linear polymerization shrinkage of unfilled resins and composites determined with a linometer. Dent Mater 1993;9:11–4.

[46] Park S-H, Krejci I, Lutz F. Consistency in the amount of linear polymerization shrinkage in syringe-type composites. Dent Mater 1999;15:442–6.

[47] Abu-elenain DA, Lewis SH, Stansbury JW. Property evolution during vitrification of dimethacrylate photopolymer networks. Dent Mater 2013;29:1173–81.

[48] Fano V, Ortalli I, Pizzi S, Bonanini M. Polymerization shrinkage of microfilled composites determined by laser beam scanning. Biomaterials 1997;18:467–70.

[49] Sharp LJ, Choi IB, Lee TE, Sy A, Suh BI. Volumetric shrinkage of composites using video-imaging. J Dent 2003;31:97–103.

[50] Tiba A, Charlton DG, Vandewalle KS, Ragain JC. Comparison of two video-imaging instruments for measuring volumetric shrinkage of dental resin composites. J Dent 2005;33:757–63.

[51] Lee I-B, Min S-H, Seo D-G. A new method to measure the polymerization shrinkage kinetics of composites using a particle tracking method with computer vision. Dent Mater 2012;28:212–8.

[52] Li J, Fok ASL, Satterthwaite J, Watts DC. Measurement of the full-field polymerization shrinkage and depth of cure of dental composites using digital image correlation. Dent Mater 2009;25:582–8.

[53] Chuang S-F, Chang C-H, Chen TY-F. Spatially resolved assessments of composite shrinkage in MOD restorations using a digital-image-correlation technique. Dent Mater 2011;27:134–43.

[54] Miletic V, Manojlovic D, Milosevic M, Mitrovic N, Stankovic TS, Maneski T. Analysis of local shrinkage patterns of self-adhering and flowable composites using 3D digital image correlation. Quintessence Int 2011;42:797–804.

[55] Li J, Lau A, Fok ASL. Application of digital image correlation to full-field measurement of shrinkage strain of dental composites. J Zhejiang Univ Sci A 2013;14:1–10.

[56] Milosevic M, Miletic V, Mitrovic N. Measurement of Local Deformation Fields in Dental Composites Using 3d Optical System. Chem List 2011;105:751–7.

[57] Martinsen M, El-Hajjar RF, Berzins DW. 3D full field strain analysis of polymerization shrinkage in a dental composite. Dent Mater 2013;29:e161–7.

[58] Kweon H-J, Ferracane J, Kang K, Dhont J, Lee I-B. Spatio-temporal analysis of shrinkage vectors during photo-polymerization of composite. Dent Mater 2013;29:1236–43.

[59] Wells-Gray EM, Kirkpatrick SJ, Sakaguchi RL. A dynamic light scattering approach for monitoring dental composite curing kinetics. Dent Mater 2010;26:634–42.

[60] Zeiger DN, Sun J, Schumacher GE, Lin-Gibson S. Evaluation of dental composite shrinkage and leakage in extracted teeth using X-ray microcomputed tomography. Dent Mater 2009;25:1213–20.

[61] Chiang Y-C, Rösch P, Dabanoglu A, Lin C-P, Hickel R, Kunzelmann K-H. Polymerization composite shrinkage evaluation with 3D deformation analysis from microCT images. Dent Mater 2010;26:223–31.

[62] Cho E, Sadr A, Inai N, Tagami J. Evaluation of resin composite polymerization by three dimensional micro-CT imaging and nanoindentation. Dent Mater 2011;27:1070–8.

[63] De Boer J, Visser RJ, Melis GP. Time-resolved determination of volume shrinkage and refractive index change of thin polymer films during photopolymerization. Polymer (Guildf) 1992;33:1123–6.

[64] Fogleman EA, Kelly MT, Grubbs WT. Laser interferometric method for measuring linear polymerization shrinkage in light cured dental restoratives. Dent Mater 2002;18:324–30.

[65] Arenas G, Noriega S, Vallo C, Duchowicz R. Polymerization shrinkage of a dental resin composite determined by a fiber optic Fizeau interferometer. Opt Commun 2007;271:581–6.

[66] Demoli N, Knežević A, Tarle Z, Meniga A, Šutalo J, Pichler G. Digital interferometry for measuring of the resin composite thickness variation during blue light polymerization. Opt Commun 2004;231:45–51.

[67] Knežević A, Demoli N, Tarle Z, Solc M. Digital Holographic Interferometry-A New Method for Measuring Polymerization Shrinkage of Composite Materials. Acta Stomat Croat 2005:155–60.

[68] Knezevic A, Sariri K, Sovic I, Demoli N, Tarle Z. Shrinkage evaluation of composite polymerized with LED units using laser interferometry. Quintessence Int 2010;41:417–25.

[69] Pantelic D, Blazic L, Savic-Sevic S, Muric B, Vasiljevic D, Panic B, et al. Real-time measurement of internal stress of dental tissue using holography. Opt Express 2007;15:6823–30.

[70] Kamal MR. Thermoset characterization for moldability analysis. Polym Eng Sci 1974;14:231–9.

[71] Cadenaro M, Biasotto M, Scuor N, Breschi L, Davidson CL, Di Lenarda R. Assessment of polymerization contraction stress of three composite resins. Dent Mater 2008;24:681–5.

[72] Mucci V, Arenas G, Duchowicz R, Cook WD, Vallo C. Influence of thermal expansion on shrinkage during photopolymerization of dental resins based on bis-GMA/TEGDMA. Dent Mater 2009;25:103–14.

[73] Watts DC, Cash AJ. Kinetic measurements of photo-polymerization contraction in resins and composites. Meas Sci Technol 1991;2:788–94.

[74] Arikawa H, Kanie T, Fujii K, Takahashi H, Ban S. Effect of inhomogeneity of light from light curing units on the surface hardness of composite resin. Dent Mater J 2008;27:21–8.

[75] Vandewalle KS, Roberts HW, Rueggeberg FA. Power distribution across the face of different light guides and its effect on composite surface microhardness. J Esthet Restor Dent 2008;20:108–117; discussion 118.

[76] Silikas N, Eliades G, Watts DC. Light intensity effects on resin-composite degree of conversion and shrinkage strain. Dent Mater 2000;16:292–6.

[77] Li J, Li H, Fok ASL, Watts DC. Multiple correlations of material parameters of light-cured dental composites. Dent Mater 2009;25:829–36.

[78] Furuse AY, Mondelli J, Watts DC. Network structures of Bis-GMA/TEGDMA resins differ in DC, shrinkage-strain, hardness and optical properties as a function of reducing agent. Dent Mater 2011;27:497–506.

[79] Hecht E. Optics. 4th ed. Addison-Wesley; 2001.

[80] Ramer G, Lendl B. Attenuated Total Reflection Fourier Transform Infrared Spectroscopy. Ecyclopaedia Anal. Chem., 2013.

[81] Stansbury JW, Dickens SH. Determination of double bond conversion in dental resins by near infrared spectroscopy. Dent Mater 2001;17:71–9.

[82] Rees JS, Jacobsen PH. The elastic moduli of enamel and dentine. Clin Mater 1993;14:35–9.

[83] Neumann MG, Miranda WG, Schmitt CC, Rueggeberg FA, Correa IC. Molar extinction coefficients and the photon absorption efficiency of dental photoinitiators and light curing units. J Dent 2005;33:525–32.

[84] Stansbury JW. Dimethacrylate network formation and polymer property evolution as determined by the selection of monomers and curing conditions. Dent Mater 2012;28:13–22.

[85] Stansbury JW. Curing Dental Resins and Composites by Photopolymerization. J Esthet Restor Dent 2000;12:300–8.

[86] Lecamp L, Youssef B, Bunel C, Lebaudy P. Photoinitiated polymerization of a dimethacrylate oligomer: 2. Kinetic studies. Polymer (Guildf) 1999;40:1403–9.

[87] Piloyan GO, Ryabchikov ID, Novikova OS. Determination of Activation Energies of Chemical Reactions by Differential Thermal Analysis. Nature 1966;212:1229–1229.

[88] Kamal MR, Sourour S. Kinetics and thermal characterization of thermoset cure. Polym Eng Sci 1973;13:59–64.

[89] Halvorson RH, Erickson RL, Davidson CL. The effect of filler and silane content on conversion of resin-based composite. Dent Mater 2003;19:327–33.

Appendix A
Spherical Mirror Interference Pattern Equation

The interference pattern measured by the CCD camera is produced by the interference between the light beam reflected from the flat reference mirror and that from the spherical mirror in the sample arm of the Michelson interferometer. In this thesis, the light beam diameter was 1 cm, the shortest focal length of the spherical mirror used was 20.3 cm and its radius of curvature, R, was 40.6 cm. In the limit where the light beam radius is much smaller than R, it can be shown that [1]:

$$R = 2f \tag{1}$$

where f is the spherical mirror focal length. Then the mirror deflection is:

$$D(r) = \frac{r^2}{4f} \tag{2}$$

where r is the radial distance away from the mirror center.

The optical path length difference, $L(r)$, between two parallel light rays located at r:

$$L(r) = 2D(r) \tag{3}$$

The associated phase difference is:

$$\emptyset(r) = 2\pi\left(\frac{L(r)}{\lambda}\right)$$
$$\emptyset(r) = \frac{\pi r^2}{\lambda f} \tag{4}$$

where λ = 632.8 nm is the emission wavelength of the HeNe laser.

The intensity of the interference pattern is:

$$I(r) = A\cos(\emptyset(r) + B) + C \tag{5}$$

$$I(r) = A\cos\left(\frac{\pi r^2}{\lambda f} + B\right) + C$$

The coefficients A, B, C and f are adjustable parameters in the non-linear least squares fitting of the interference pattern.

Appendix B

NORMALIZED AUTOCATALYTIC EQUATION DERIVATION

This section provides the derivation of Equation 4 in Chapter 5.

The autocatalytic equation is:

$$\dot{D} = aD^m(b-D)^n \tag{1}$$

where $\dot{D} \equiv \frac{dD}{dt}$ is the deflection rate and it is implied that deflection is a function of time, $D = D(t)$. To determine the maximum deflection rate let D_o be the value of D at which $\dot{D}$ is a maximum and $\ddot{D}(D_o) = 0$ where $\ddot{D} \equiv \frac{d\dot{D}}{dt}$:

$$\ddot{D} = 0 = a^2 {D_o}^{2m-1}(b-D_o)^{2n-1}(mb - D_o(m+n)) \tag{2}$$

The solution which satisfies Equation 2 and produces the maximum deflection rate is:

$$D_o = \frac{mb}{(m+n)} \tag{3}$$

Substituting Equation 3 into Equation 1 to determine the value of the maximum deflection rate gives:

$$\begin{aligned} \dot{D}_{max} &= ab^{m+n}\left(\frac{m}{m+n}\right)^m\left(1-\frac{m}{m+n}\right)^n \\ &= a\left(\frac{b}{m+n}\right)^{m+n} m^m n^n \end{aligned} \tag{4}$$

Substituting the normalized deflection, $\delta = D/b$, into Equation 1 produces:

$$\dot{D} = ab^{m+n}\delta^m(1-\delta)^n \tag{5}$$

Then dividing Equation 5 by Equation 4 and simplifying:

$$\frac{\dot{D}}{\dot{D}_{max}} = \frac{(m+n)^{m+n}}{m^m n^n}\delta^m(1-\delta)^n \tag{6}$$

The left hand side of Equation 6 can be written as:

$$\frac{\dot{D}}{\dot{D}_{max}} = \frac{\dot{D}/b}{\dot{D}_{max}/b} = \frac{\dot{\delta}}{\dot{\delta}_{max}} \tag{7}$$

Where $\dot{\delta}_{max}$ is the maximum of the normalized deflection rate and $\dot{\delta} \equiv \frac{d\delta}{dt}$. Substituting Equation 7 into Equation 6 produces the final result:

$$\frac{\dot{\delta}}{\dot{\delta}_{max}} = \frac{(m+n)^{m+n}}{m^m n^n} \delta^m (1-\delta)^n \tag{8}$$

The solution which produces the normalized deflection at which the maximum normalized deflection rate occurs is simply Equation 3 divided by *b*:

$$\begin{aligned} \delta_o &= \frac{m}{(m+n)} \\ &= \frac{1}{\frac{n}{m}+1} \end{aligned} \tag{9}$$